Photoelectrochemical Water Splitting for Hydrogen Production Using III-V Semiconductor Materials

In Partial Satisfaction of the Requirements for the Degree of Doctor of Philosophy

Mahdi Mohammed Alqahtani

Supervised by

Professor Ivan Parkin

Department of Electronic & Electrical Engineering

University College London

2019

Declaration

‘I, Mahdi Mohammed Alqahtani confirm that the work presented in this thesis is my own. Where information has been derived from other sources, I confirm that this has been indicated in the thesis.’

Abstract

The use of photoelectrochemical (PEC) water splitting to harvest intermittent solar sources in the form of hydrogen is an attractive potential method to address energy and environmental issues. Since 1972, when Honda and Fujishima demonstrated the use of titanium dioxide (TiO_2) in PEC water splitting (1), extensive efforts have been devoted to the development of photoelectrode stability and high solar-to-hydrogen efficiency. Metal oxides (e.g. TiO_2, Fe_2O_3, $BiVO_4$, and $SrTiO_2$) have been extensively studied but their large band gap and sluggish charge transfer kinetics typically limited their solar-to-hydrogen conversion efficiency (1-9). III-V semiconductor materials have proven attractive for PEC water splitting due to their high efficiency, optimal band gap, and excellent optical properties but they are readily susceptible to corrosion in strongly acidic or basic aqueous solutions during the PEC process (10-18).

This thesis aims to construct a PEC device (e.g. photoanode and photocathode) based on III-V semiconductor materials (such as InGaN, GaP, and GaPSb) for PEC water splitting. The design of a direct PEC water splitting device requires a suitable band gap to cover the entire solar spectrum (visible range), which leads to a high photocurrent and solar-to-hydrogen (STH) efficiency. The band edge alignment must straddle the hydrogen and oxygen redox potentials and stable under illumination in electrolyte conditions (19). However, the current challenge is to develop efficient and stable solar-to-chemical conversion systems based on III-V semiconductor materials for PEC water splitting. This can be addressed by incorporating novel co-catalysts that are physically and electrically attached to the surface of the photoelectrodes. The role of the co-catalyst is to minimize the overpotentials and accelerate the charge kinetics at the semiconductor/electrolyte interface (20). Additionally, the surface modification

strategy of applying co-catalysts can extend the stability of the photoelectrode for long-time operation (21-25).

Impact Statement

Consumption of energy has increased rapidly in recent decades to meet the needs of a growing world population and economy. Solar energy that can be directly converted to electricity or chemical fuels represents a massive source of renewable energy to meet the increasing energy demands. In this context, photoelectrochemical (PEC) water splitting is a promising method to harvest solar energy and provide clean energy (e.g. hydrogen) (26-29). Group III-V semiconductors have been shown to have the highest efficiencies for PEC water splitting but the prohibitive cost of single-crystalline wafers may limit their practical use and large-scale application. The research reported in this thesis addresses some issues associated with the high cost of III-V semiconductor materials and improves their PEC performance to meet the demands of economic hydrogen production.

Highlights:

- Group III-V semiconductor photoelectrodes directly grown on a Si substrate by solid-source molecular beam epitaxy (MBE) with a high-quality structure will reduce the cost of the electrode due to the maturity of Si-based fabrication technologies.
- Stabilization of III-V photoelectrodes by using an earth-abundant co-catalyst and protection layer shows potential for the widespread deployment of cost-effective photoelectrodes for hydrogen generation compared to III-V photoelectrode single crystalline commercial wafers.
- Exploration and growth of a new ternary III-V semiconductor photoelectrode as a single absorber is advantageous due to a balanced combination of

simplicity in fabrication and efficient photon harvesting for hydrogen production.

- The unique design structures, suitable band gap, stability and efficiency of the photoelectrodes are promising for PEC water splitting applications.

Acknowledgements

First and foremost, I would like to express my deepest thanks to my principal supervisor, Prof. Ivan P. Parkin, Dean of Mathematical & Physical Sciences, UCL, who has offered me constant support and guidance. I would also like to thank my subsidiary supervisor, Prof. Huiyun Liu, for his support and for growing some structures at his MBE lab. I also thank Prof. Shuji Nakamura (Nobel Laureate) and Dr. Abdullah Alhassan at the University of California, Santa Barbara (UCSB) for growing my InGaN/GaN MQWs device structure.

Thank you to our collaborator Prof. Charles Cornet, Head of the OHM research group at the University of Rennes, INSA, for growing the $GaP_{1-x}Sb_x$ structure on the Si substrate.

My special thanks to Prof. Jiang Wu, who supported and provided me with countless valuable comments and insightful discussion in the field. Thank you to Prof. Chris Blackman at the Department of Chemistry, UCL for providing the ALD reactor and related discussion.

I would also like to thank Dr. Sanjayan Sathasivam and Dr. Andreas Kafizas, as they always brought a new point of view and broadened my horizons in many ways.

I especially like to thank my family. My parents, brothers, and sisters deserve many thanks for their continued support and encouragement. My wife, Hind, and daughter, Deem have been extremely supportive of me throughout my entire PhD and have made countless sacrifices to help me get my PhD.

I gracefully acknowledge the support and scholarship from King Abdulaziz City for Science and Technology (KACST), which provided excellent opportunities for me to

meet scientists, graduate students, and post-doctoral fellows to discuss the latest developments in my field. This support was undoubtedly of great value to my research and overall career development.

List of Journal Publications and Conference Presentations

Journal Publications

1- Alqahtani, M.; Sathasivam, S.; Cui, F.; Steier, L.; Xia, X.; Blackman, C.; Kim, E.; Shin, H.; Benamara, M.; Mazur, Y. I.; Salamo, G. J.; Parkin, I. P.; Liu, H.; Wu, J., Heteroepitaxy of GaP on silicon for efficient and cost-effective photoelectrochemical water splitting. *Journal of Materials Chemistry A* **2019,** *7* (14), 8550-8558.

2- Alqahtani, M.; Sathasivam, S.; Chen, L.; Jurczak, P.; Piron, R.; Levallois, C.; Létoublon, A.; Léger, Y.; Boyer-Richard, S.; Bertru, N.; Jancu, J. M.; Cornet, C.; Wu, J.; Parkin, I. P., Photoelectrochemical water oxidation of $GaP_{1-x}Sb_x$ with a direct band gap of 1.65 eV for full spectrum solar energy harvesting. *Sustainable Energy & Fuels* **2019**.

3- Alqahtani, M.; Sathasivam, S.; Alhassan, A.; Cui, F.; BenJaber, S.; Blackman, C.; Zhang, B.; Qin, Y.; Parkin, I. P.; Nakamura, S.; Liu, H.; Wu, J., InGaN/GaN Multiple Quantum Well Photoanode Modified with Cobalt Oxide for Water Oxidation. *ACS Applied Energy Materials* **2018,** *1* (11), 6417-6424.

4- Alqahtani, M.; Ben-Jabar, S.; Ebaid, M.; Sathasivam, S.; Jurczak, P.; Xia, X.; Alromaeh, A.; Blackman, C.; Qin, Y.; Zhang, B.; Ooi, B. S.; Liu, H.; Parkin, I. P.; Wu, J., Gallium Phosphide photoanode coated with TiO_2 and CoO_x for stable photoelectrochemical water oxidation. *Opt Express* **2019,** *27* (8), A364-A371.

5- Zhang T, Wu J, Zhang P, Ahmad W, Wang Y, **Alqahtani M**, et al. High Speed and Stable Solution-Processed Triple Cation Perovskite Photodetectors. Advanced Optical Materials. **2018**;6(13).

Conference Presentations

1- "Protective nanostructure for an efficient and stable water-splitting GaAs photoanode", May 28, 2018, International Conference on Hybrid and Organic Photovoltaics celebrated in Benidorm, Spain.

List of symbols and abbreviations

(hkl)	Miller indices of plane
E_g	Bandgap
E_f	Fermi level
c	Speed of light
a_0	Lattice parameter
K_B	Boltzmann constant
J_{sc}	Short-Circuit photocurrent density
J_{ph}	Photocurrent density
T	Temperature
V_{oc}	Open-Circuit Voltage
α	Absorption coefficient
ε_0	Vacuum permittivity
ε_r	Relative permittivity
λ	Wavelength
ΔG	Gibbs Free Energy
h^+	Hole
F	Faraday constant
E_{fb}	Flat band potential
e^-	electron
C	capacitance
h	Planck's constant
I	Current
q	Electronic charge
R	Gas Constant
T	Transmittance
hv	Photon energy
E_C	Conduction band
E_V	Valance band

AFM	Atomic Force Microscopy
SEM	scanning electron microscope
TEM	Transmission electron microscopy
APB	Anti-Phase Boundary
APD	Anti-Phase Domain
J-V	Photocurrent Density Versus Voltage
MBE	Molecular Beam Epitaxy
MOCVD	Metal-Organic Chemical Vapour Deposition
PL	Photoluminescence
RHEED	Reflection High Energy Electron Diffraction
TD	Threading Dislocation
UHV	Ultra-High Vacuum
UV	Ultraviolet
XRD	X-Ray Diffraction
Ar	Argon
As	Arsenic
Be	Beryllium
Ga	Gallium
In	Indium
CoO_x	Cobalt oxide
MoS_2	Molybdenum sulfide
Ni	Nickel
O	Oxygen
P	Phosphorus
Pt	Platinum
Sb	Antimony
Si	Silicon
Ti	Titanium
GaP	Gallium Phosphide
InGaN	Indium Gallium Nitride
GaPSb	Gallium Phosphide Antimony
CE	Counter Electrode
EDX	Energy Dispersive X-ray Spectroscopy
EIS	Electrochemical Impedance Spectroscopy
IPCE	Incident Photon to Current Efficiency

RHE	Reversible Hydrogen Electrode
WE	Working Electrode
STH	Solar-hydrogen efficiency

Table of Contents

List of Figures

List of Tables

Chapter 1: Introduction and Principle of Photoelectrochemical (PEC) Water Splitting

1.1. Solar Water Splitting

Fossil fuels (coal, natural gas, and oil) account for the majority of carbon emissions and are currently responsible for enhanced greenhouse effects (30, 31). The development of renewable energy sources, such as solar energy, is becoming increasingly urgent to satisfy the global demand for energy. Solar energy is converted directly into electricity by solar cells (photovoltaic cells) but the disadvantage of electricity is that it is challenging to store. A device that stores electricity is generally called a battery. However, battery technology continues to suffer due to its short lifetime and small energy density (32). Another solar conversion route is to convert solar energy into hydrogen, which is envisioned to be the ideal energy carrier for storage and distribution through transportation. In terms of power consumption, 120,000 TW of solar energy reaches the earth's surface (the remainder being scattered by the atmosphere and clouds), and only 36,000 TW reaches the land, which means that a photoelectrochemical (PEC) efficiency of only 10% would be sufficient to meet global energy needs in the year 2050 (31, 33-35). Since 1972, PEC water splitting has attracted considerable attention, and involves splitting water molecules directly into individual hydrogen and oxygen molecules (1).

Over the last 40 years, researchers have extensively investigated a variety of semiconductors for water splitting (e.g. photoanodes and photocathodes) (2, 5, 36-39). In this process, PEC water splitting utilizes semiconductor materials immersed in a water-based electrolyte. When incident sunlight strikes the surface of the semiconductor, the photon energy is converted into electrochemical energy, which can

split water into hydrogen and oxygen. This process offers a long-term and cost-effective way to produce hydrogen without greenhouse gas emissions (19). However, the development of efficient semiconductor photoelectrodes with a suitable band gap and band alignment remains challenging (40, 41).

1.2. Hydrogen Fuel as an Energy Carrier

Hydrogen gas is a non-toxic, clean solar fuel and the most abundant element in the universe. Compared with other fuels such as gasoline, hydrogen contains very high energy by weight, more than three times the energy density of gasoline, which means that hydrogen has a higher efficiency than gasoline (22%) (29). Thus, hydrogen gas can be a storable energy carrier and can deliver energy in a usable form, but it does not exist in nature and needs to be produced from diverse sources (42). As a result of its abundance, hydrogen can be extracted from a variety of materials and compounds or be produced by utilizing a wide range of methods, including some clean and "green" approaches. It can be produced from a variety of renewable and non-renewable sources of energy (43). For instance, non-renewable energy sources include fossil fuels such as coal, nuclear, oil, and natural gas, which account for the majority of carbon dioxide emissions. Renewable sources of energy such as water, wind, and biomass produce clean energy but there are some limitations (26, 35). For example, fluctuations in wind velocity limit the use of wind power. Another promising way to produce hydrogen is via PEC water splitting, which directly converts sunlight to split water into hydrogen and oxygen. Figure 1.1 shows the worldwide hydrogen production from different sources. Unfortunately, most hydrogen is produced from non-renewable energy sources. As shown in the chart, currently hydrogen is mostly produced from steam reforming of natural gas (48%); it is also produced from oil (30%) and coal

gasification (18%), whereas only 4% of hydrogen production worldwide results from water electrolysis. However, using renewable solar energy for hydrogen production minimizes greenhouse gases such as carbon dioxide produced from the utilization of conventional sources such as coal, oil, and natural gas (35).

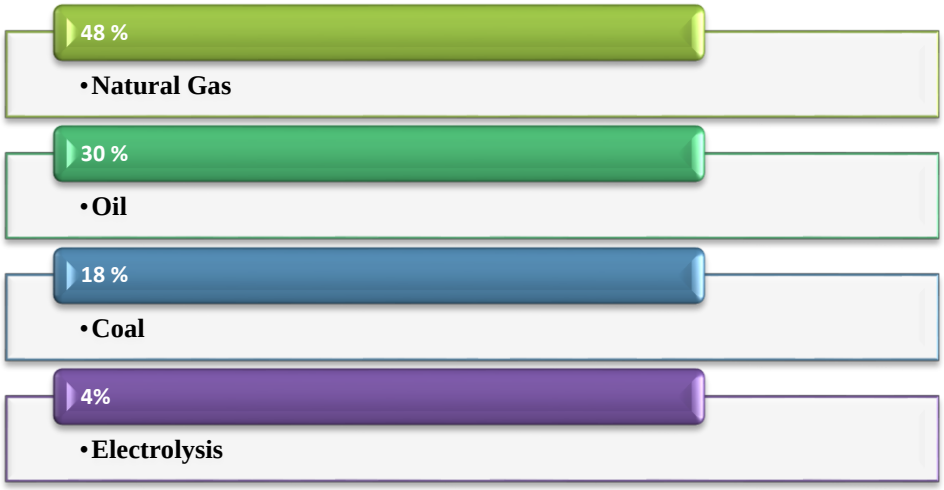

Figure 1.1. World hydrogen production capacity from different sources (35, 44).

1.3. Principle of Photoelectrochemical (PEC) Water Splitting

The concept of PEC water splitting was first demonstrated in 1972 by Fujishima and Honda (1). A PEC cell consists of an anode and a cathode immersed in an electrolyte and connected to an external circuit under illuminated light (45). The design of efficient PEC water splitting systems requires several key criteria to be met: first, the photoelectrode must have a suitable band gap to generate the water splitting potential (> 1.6); second, the band alignment edge must straddle the hydrogen and oxygen redox potentials; third, the absorption spectral range should cover the entire solar spectrum (visible range), which leads to high photocurrent and solar-to-hydrogen (STH) efficiency; fourth, high chemical stability in the dark and under illumination is required (19, 36, 46, 47). According to oxidation and reduction half-reactions, the

electrolysis of water for oxygen evolution reaction (OER) at the anode and the hydrogen evolution reaction (HER) at the cathode can be described in two electrochemical reactions (44):

In acid electrolyte,

$$2H_2O + 4e^- \rightarrow O_2 + 4H^+ \quad (V_{Anode} = 1.23\,V\ vs.RHE) \quad (1.3.1)$$

$$4H^+ + 4e^- \rightarrow 2H_2 \quad (V_{Cathode} = 0.0\,V\ vs.RHE) \quad (1.3.2)$$

In alkaline electrolyte:

$$4OH^- \rightarrow 4e^- + O_2 + 2H_2O \quad (V_{Anode} = 1.23\,V\ vs.RHE) \quad (1.3.3)$$

$$2H_2O + 4e^- \rightarrow 2H_2 + 4OH^- \quad (V_{Cathode} = 0.0\,V\ vs.RHE) \quad (1.3.4)$$

1.3.1. Energy Levels in a Semiconductor

In a semiconductor, the electrons in an isolated atom can be located at only discrete energy levels. However, if two or more atoms are brought together, these discrete energy levels split into band levels; the splitting of energy levels to form essentially continuous bands of energy is due to the Pauli Exclusion Principle (48). Naturally, in a semiconductor, the electron energy levels consist of upper bands (conduction bands) and lower bands (valence bands) that are separated by the band gap (49), as shown in Figure 1.2.

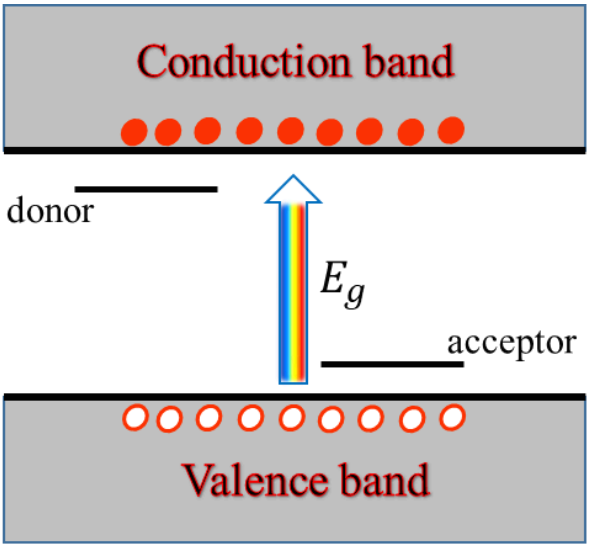

Figure 1.2. Schematic diagram showing the valence and conduction bands of a semiconductor separated by a band gap (48, 49).

The electronic conductivity of a semiconductor can be changed either by electrons of atoms in the crystal (intrinsic conductivity) or by adding an impurity of atoms (extrinsic conductivity) to make it suitable for a certain function. For an extrinsic conductivity semiconductor, the impurities are classified as either donors, which are located slightly below the conduction band, creating electron conductivity (with the semiconductor becoming an n-type semiconductor), or acceptors, which are located above the valence band, creating hole conductivity (with the semiconductor becoming a p-type semiconductor) (48), as shown in Figure 1.3. In the bulk of the semiconductor, the position of the Fermi level depends on the doping concentration. However, the density of electrons in the conduction band is related to the corresponding quasi-Fermi levels of electrons $E_{f,n}$, which can be shown as:

$$n = (N_c \exp(-(E_c - E_{f,n})/KT) \qquad (1.3.1.1)$$

where $N_c = \frac{8\sqrt{2\pi}}{h^3} (m_e^*)^{3/2} (E - E_c)^{\frac{1}{2}}$ (1.3.1.2)

Similarly, the density of holes in the valence band, which is related to the corresponding quasi-Fermi levels of holes $E_{f,p}$, is given by (50):

$$p = (N_v \exp(-(E_{f,p} - E_v)/KT) \quad (1.3.1.3)$$

where $N_v = \frac{8\sqrt{2\pi}}{h^3} (m_h^*)^{3/2} (E - E_h)^{\frac{1}{2}}$ (1.3.1.4)

in which N_c *and* N_v are the effective densities of the energy states in the conduction and valence bands, respectively; h is Planck's constant; and m_e^* and m_h^* are the effective masses of electrons and holes, respectively (48).

An intrinsic conductivity semiconductor refers to an ideal single crystal and no dopant present; there is an equilibrium concentration of electrons and holes at room temperature as a result of the thermal excitation of some electrons from the valence band to the conduction band. At equilibrium, the Fermi levels of electrons and holes are equal, which leads to

$$np = n_i^2 = constant \quad (1.3.1.5)$$

Where n_i is the intrinsic carrier density which is given by (50):

$$np = N_c N_v \exp\left(-\frac{E_c - E_v}{KT}\right) = n_i^2 \quad (1.3.1.6)$$

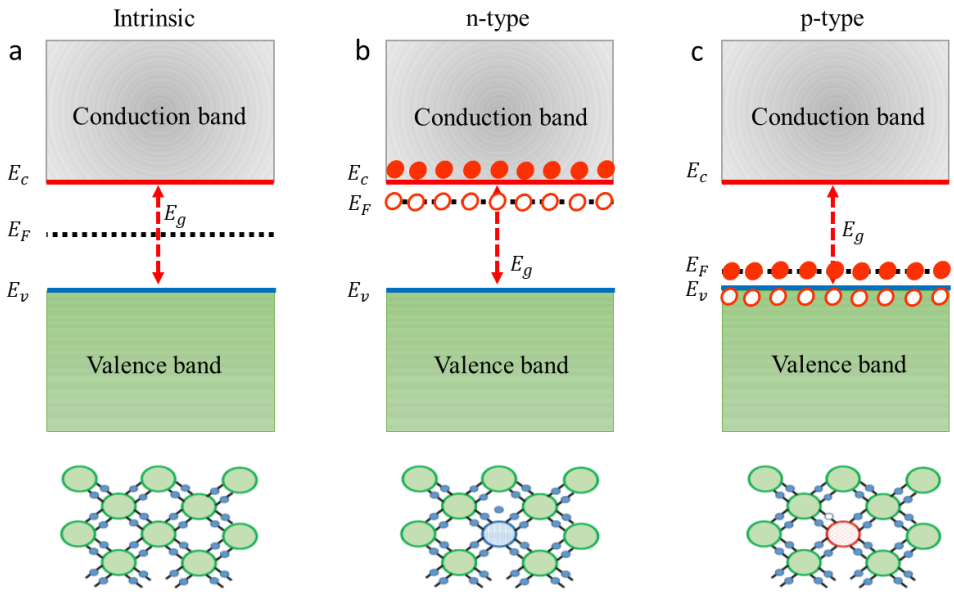

Figure 1.3. Energy band illustration. **(a)** Intrinsic semiconductor. **(b)** n-type semiconductor. **(c)** p-type semiconductor (47, 48).

1.3.2. Direct and Indirect Band Gaps

The band gap represents the minimum energy gap between the conduction band and the valence band. However, the top of the valence band and the bottom of the conduction band are generally not at the same value of electron momentum. In the case of a direct band gap semiconductor, the valence band and the conduction band occur at the same value of momentum (48), as shown in Figure 1.4(a), which implies that a photon of energy $E_c - E_v = E_g$ is required.

In an indirect band gap semiconductor, the maximum energy of the valence band is located at a different value of momentum from the minimum in the conduction band because the excitation of an electron from the valence band to the conduction band requires a change in the electron momentum. Specifically, it requires an electron to interact not only with an absorbed photon but also with the lattice vibration, called a phonon (48, 51), as shown in Figure 1.4(b).

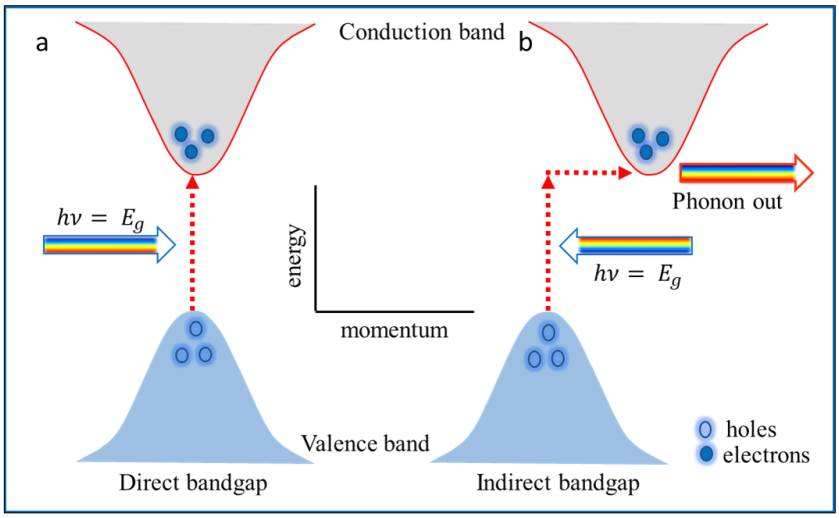

Figure 1.4. Schematic band diagrams for the photoluminescence processes. **(a)** In a direct band gap semiconductor. **(b)** an indirect band gap semiconductor (48, 51).

1.3.3. The Semiconductor/Electrolyte Interface

In electrochemistry, the chemical potential of electrons for the redox couple is given by the Nernst equation (47, 52):

$$\varphi_{redox} = \varphi^0_{redox} + KTln\left(\frac{a_{ox}}{a_{red}}\right) \qquad (1.3.3.1)$$

Where φ_{redox} is the standard redox potential, which is equivalent to the Fermi level, and a_{ox} and a_{red} are the concentrations of the oxidized and reduced species of the redox couple, respectively. The redox potentials are generally given on a conventional scale using the normal hydrogen electrode (NHE) or the saturated calomel electrode (SCE) as a reference electrode (47), whereas the electron energy at the vacuum level has been used as a reference in semiconductor solid-state physics (47, 49, 51). Thus, the energy of the redox couple can be written as:

$$E_{redox} = E_{ref} - e\varphi_{redox} \qquad (1.3.3.2)$$

Where φ_{redox} is the redox potential versus NHE and E_{ref} is the energy of the reference electrode relative to the energy of a free electron at the vacuum level. The value of E_{ref} corresponding to the vacuum level is approximately $-4.50\ eV$ for NHE, so the equation yields (47, 53):

$$E_{redox} = -4.50\ eV - e\varphi_{redox} \qquad (1.3.3.3)$$

Fundamentally, the anode or cathode consists of a semiconductor that absorbs sunlight, and the other electrode is a metal. Under dark conditions, when a semiconductor is immersed in an electrolyte solution, the Fermi level of the semiconductor is higher than that of the electrolyte. For an n-type semiconductor, electrons will transfer between the semiconductor and the electrolyte until equilibrium is established, $E_f = E_{f,redox}$. Thus, the Fermi level, which is the electrochemical potential, is the same in the semiconductor and the electrolyte.

An energy diagram of an n-type semiconductor electrode in contact with an electrolyte under dark and illuminated conditions is show in Figure 1.5. Upon illumination, the semiconductor will have a positive charge that is distributed in the region close to the surface, which is called the space-charge region, whereas the electrolyte will have a negative charge that spreads throughout the electrolyte in the region close to the semiconductor interface, which is called the Helmholtz layer. The electric field in the space-charge region causes the band to bend upwards, which directs the minority carriers towards the electrolyte. Similarly, for a p-type semiconductor, the negative charge is distributed in the space-charge region, whereas the electrolyte is positively charged. Thus, the electron flow into the electrolyte results in downward band bending due to the electric field (29, 49, 52).

In addition to the Fermi level of the redox system, this model introduces the existence of occupied and empty energy states corresponding to the reduced and oxidized species of the redox system, respectively (47). In the electrolyte, the fluctuation of solvent dipoles arising from the thermal energy $K_B T$ leads to a Gaussian distribution of redox states (reduced species and oxidized species) as a function of the electron energy (54). The distribution functions for the states are given by (47, 54):

$$D_{ox} = \exp\left[-\frac{(E - E_{f,redox} - \lambda)^2}{4KT\lambda}\right] \qquad (1.3.3.4)$$

$$D_{rd} = \exp\left[-\frac{(E - E_{f,redox} + \lambda)^2}{4KT\lambda}\right] \qquad (1.3.3.5)$$

Where λ is the reorganization energy of electron transfer.

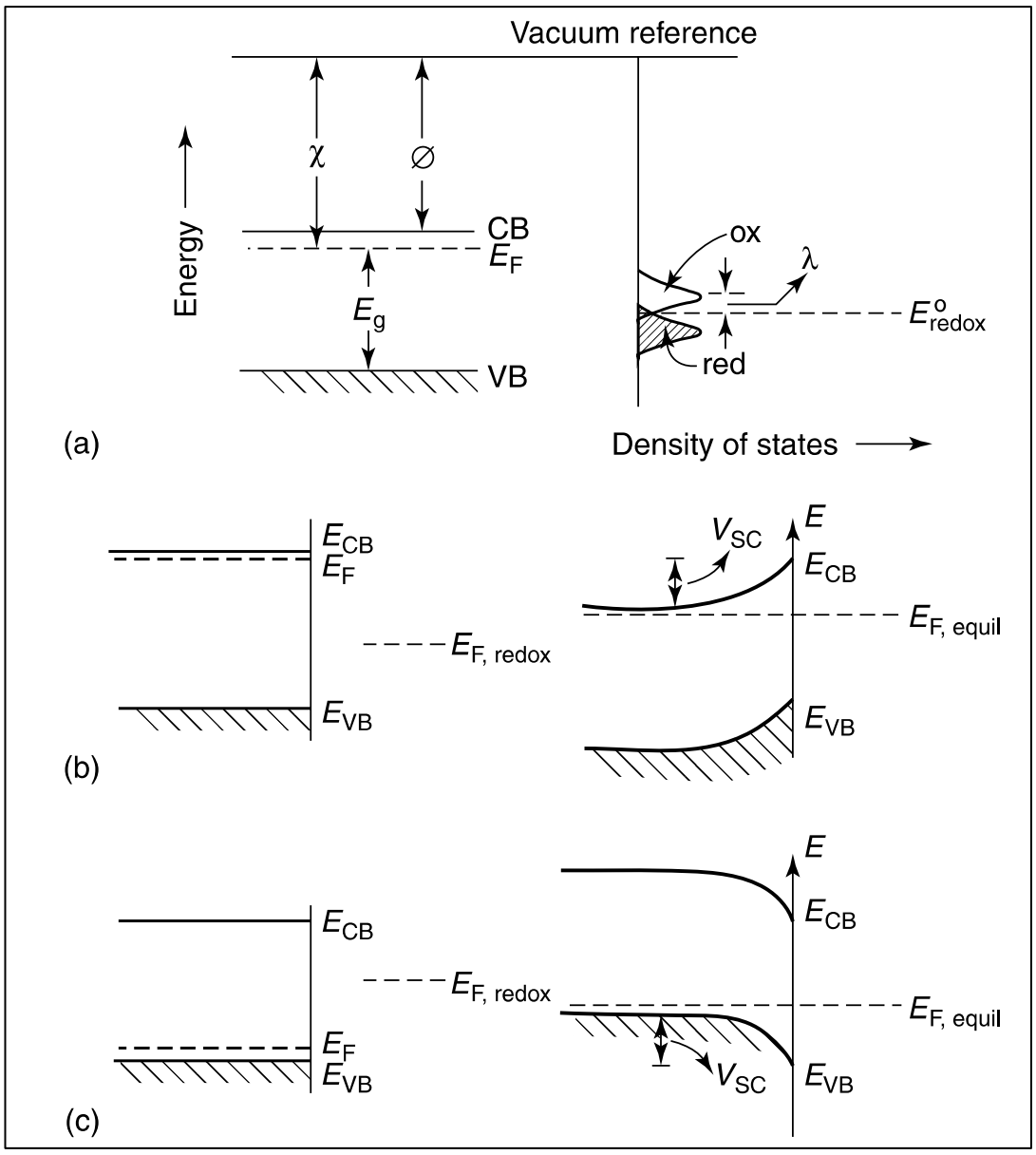

Figure 1.5. Schematic illustration of electronic energy levels at semiconductor/electrolyte interface. **(a)** The electron energy levels of a redox couple and semiconductor. **(b)** A diagram of n-type semiconductor photoanode before and after contact with the electrolyte. **(c)** A diagram of a p-type semiconductor before and after contact with the solution (51).

The band position of the energy levels for the interfacial region can be experimentally determined by investigating the charge and potential distribution across the interface. Thus, the total potential difference across the interfacial region is given by (55):

$$U_E = \phi_{SC1} + \phi_H + C \qquad (1.3.3.6)$$

Where U_E is the electrode potential that is measured between an ohmic contact on the rear surface of the semiconductor electrode and the reference electrode, ϕ_H is the potential drop across the Helmholtz layer, and ϕ_{SC1} is the potential across the space-charge layer (55). The potential distribution across the semiconductor/electrolyte interface is shown in Figure 1.6.

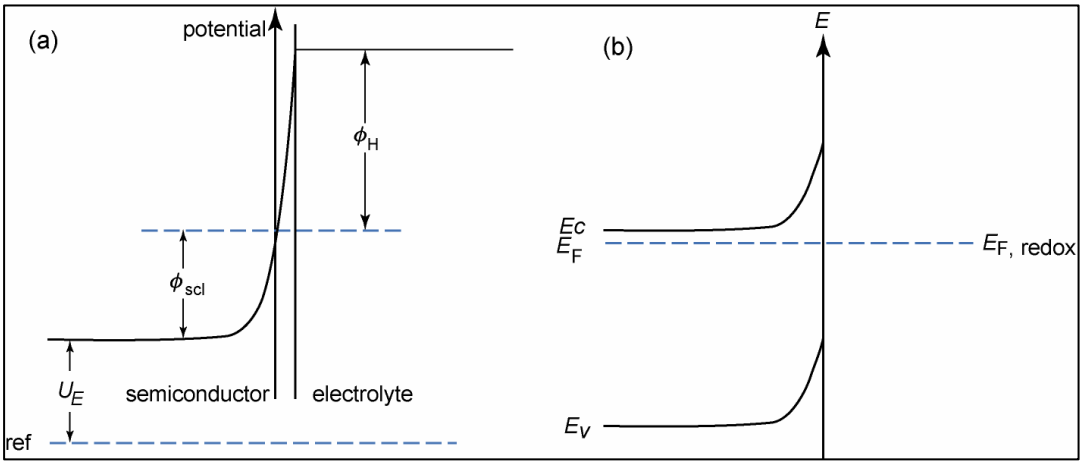

Figure 1.6. Potential distribution. **(a)** At the semiconductor/electrolyte interface. **(b)** Energy scheme of the same interface (55).

The Helmholtz layer is formed by adsorption of ions or molecules on the surface of the semiconductor by oriented dipoles or by the formation of surface bonds between the solid surface and species in the electrolyte. However, since the potential across the Helmholtz layer is unknown, it can thus be obtained by measuring the capacitance of the space-charge layer, which is called a Mott–Schottky *(M–S)* measurement (7, 51, 56).

$$\left(\frac{1}{C_{sc}^2} = \frac{2}{\epsilon_r\,\epsilon_o\,N_D\,eA^2}\left(E - E_{\text{fb}} - \frac{\text{KT}}{e}\right)\right) \qquad (1.3.3.7)$$

Where ϵ_r is the relative permittivity of the semiconductor, ϵ_o is the permittivity in vacuum, A is the surface area, e is the charge of an electron, N_D is the free carrier density, K is the Boltzmann constant, T is the temperature, E_{fb} is the flat-band potential, and E is the applied potential. Moreover, the conductivity type of the electrolyte can be explored by Mott–Schottky analysis. The p-type materials possess a negative slope and n-type materials possess a positive slope, (56) as shown in Figure 1.7.

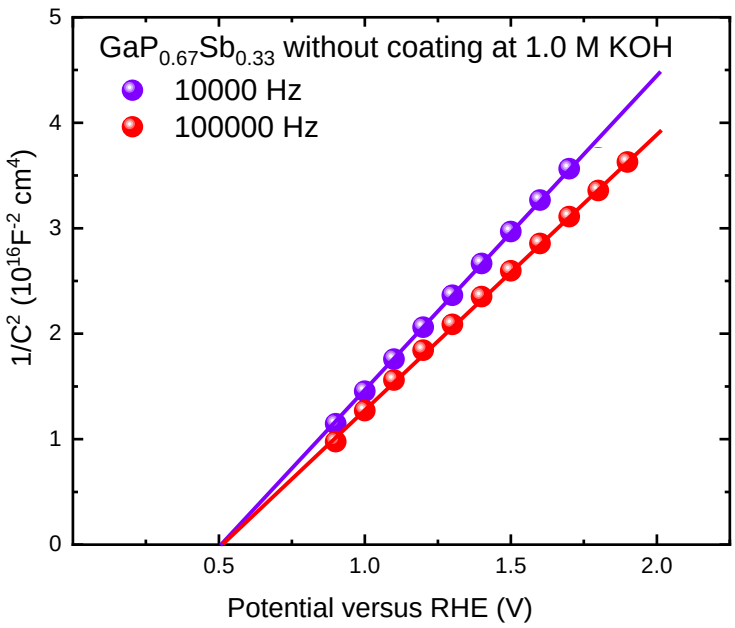

Figure 1.7. Mott–Schottky (*M–S*) plot as a function of the applied potential (E) for the $GaP_{0.67}Sb_{0.33}$ without coating at 10000 and 100000 Hz at 1.0 M KOH. The slope is positive, which indicates that the electrode is an n-type material. The flat-band potential (V_{FB}) and the donor concentration were 0.5 V and 3.86 $\times 10^{15}$ cm^{-3} versus RHE, respectively.

Figure 1.8 shows the band gaps and band positions of several n-type and p-type semiconductors at pH ~1. The photocorrosion resistance of the semiconductors depends upon the alignment of band edges relative to oxygen and reduction evolution potentials. The semiconductors are thermodynamically unstable when the anodic potential is above the valence band potential for photoanodes and the cathodic redox potential is below the conduction band for photocathodes (29, 57-59). For those materials with band positions that mismatch with the redox potentials of water splitting, an external applied potential is required in order to split the water.

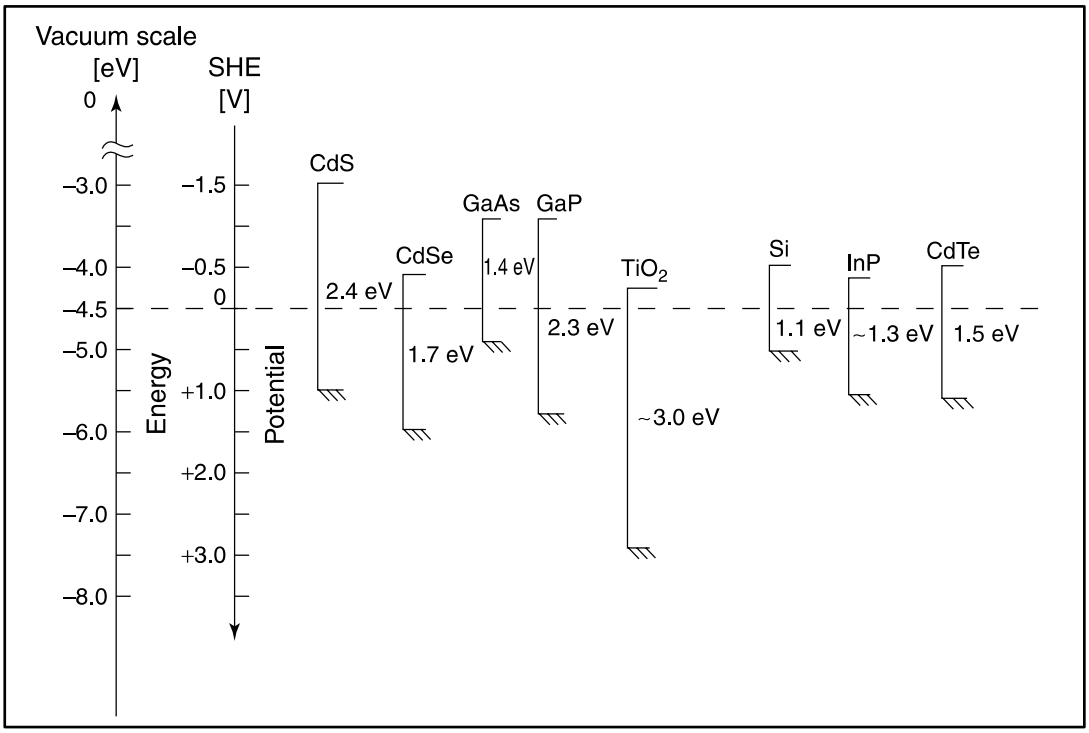

Figure 1.8. Band gaps (eV) and band edge positions of common semiconductor photoelectrodes with respect to the oxidation and reduction potentials of water at pH ~ 1(51).

1.4. III-V Semiconductor Photoelectrodes for PEC Water Splitting

PEC water splitting is one of the most promising solutions to the escalating energy demand and environmental issues. For decades, Honda and Fujishima demonstrated solar-driven PEC water splitting using an n-TiO_2 photoelectrode under UV light. Later on, extensive research efforts have focused on improving PEC water splitting performance. For example, metal oxides such as TiO_2 (band gap of 3.4 eV), $SrTiO_3$ (3.2 eV), and $KTaO_3$ (3.5 eV) have performed water splitting without extra bias, but they limited photon absorption in the ultraviolet irradiation due to a large band gap (3). However, the requirement of photoelectrodes for a narrow band gap to increase absorption of a large portion of the solar spectrum has driven investigation of metal oxides, including iron oxide (Fe_2O_3), bismuth vanadate ($BiVO_4$), and tungsten oxide (WO_3), but these oxide photoelectrodes are limited by higher applied biases due to their poor electronic properties (2, 60-64). Group III-V semiconductor materials have an excellent optical property, band gap tunability, and have held the record for solar-to-hydrogen conversion efficiency for decades but are unstable in alkaline or acidic electrolytes (10, 11, 13, 65). The half-cell photoelectrode consists of only one absorber semiconductor in which the single absorber semiconductor photoelectrode can be either a photocathode or a photoanode for water oxidation or reduction, as shown in Figure 1.9(a-b). For semiconductor photoelectrodes to be practical, they should meet several requirements: a sufficiently narrow band gap to harvest the solar spectrum and suitable band-edge potentials for water reduction or oxidation (19, 26, 29). In this context, a variety of III-V semiconductor photoelectrodes have been widely reported on regarding their half-cell efficiency for water reduction and oxidation (10, 21, 24, 29, 66).

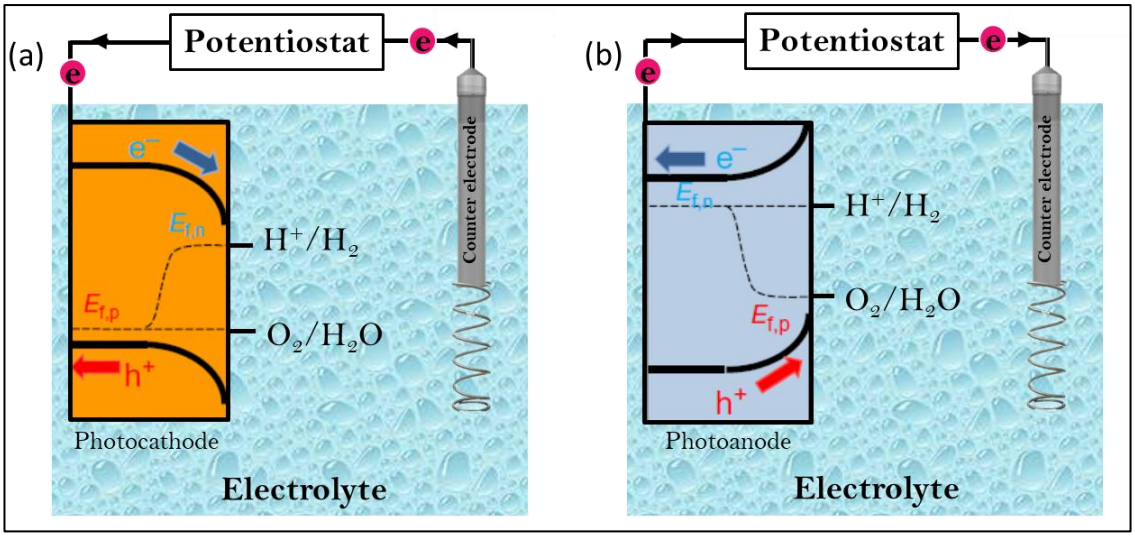

Figure 1.9. Schematic illustration of semiconductor/interface. **(a)** A single absorber semiconductor photocathode in contact with electrolyte for water reduction. **(b)** A single absorber semiconductor photoanode in contact with electrolyte for water oxidation.

1.5. III-V Photoelectrodes as Photocathodes for Water Reduction

Indium phosphate (InP) with a band gap of ~1.3 eV was investigated due to the direct band gap and suitable band alignment edge for water reduction (17, 24). Recently, the nanostructured single-crystalline commercial wafer InP nanopillar photocathode combined with TiO_2 and Ru as the co-catalyst led to a record solar-to-hydrogen (STH) efficiency of 14% for efficient water reduction (67). At the cost of photoelectrode reduction, an InP photocathode passivated with a TiO_2 layer and Pt co-catalyst achieved an STH efficiency of 11.6% for water reduction by a vapor−liquid−solid growth to reduce the high cost of the single-crystalline wafer (68). In addition, the MoS_3 co-catalyst nanoparticle modified the InP photocathode nanowire resulting in an STH of 6.4% (24).

Another interesting absorber semiconductor, gallium phosphate (GaP), has a 2.25 eV indirect band gap and a 2.78 eV direct band gap; it has been studied for decades but

suffers from corrosion under aqueous solutions (15, 69-72). A GaP photocathode has been reported to have a high open circuit potential of 0.710 V by forming a heterojunction of n-TiO_2 or n-Nb_2O_5 onto the GaP surface under one solar sun illumination (14). Moreover, a GaP nanowire with a direct band gap with optimized geometry to extend the large portion of solar absorption has been reported. By modifying the GaP NW with a suitable co-catalyst of Pt, a high STH efficiency of 2.9% was obtained (15). Recently, a GaP photocathode thin film was monolithically grown directly on a silicon substrate, resulting in a significant reduction in the cost of the photoelectrode compared to a single-crystal GaP wafer. The GaP was passivated with an amorphous TiO_2 and MoS_2 co-catalyst, which led to a slight improvement in PEC performance (73). Gallium arsenide (GaAs) has been investigated as a photocathode due to the conduction band edge alignment for water reduction. Surface modification using the spalling process on the GaAs photocathode leads to a shifting of onset potential and high photocurrent density (74).

1.6. III-V Photoelectrodes as Photoanodes for Water Oxidation

The III-V photoelectrodes are less frequently demonstrated as photoanodes for water oxidation, due to the relatively high overpotential and slow kinetics of the four-hole reaction; the water oxidation process is widely considered a bottleneck for the sustainable and efficient generation of H_2(g) by solar-driven water splitting (18, 29, 75-82). Therefore, the development of PEC water splitting systems has been hindered in part by the lack of semiconducting photoanodes that are efficient and stable under alkaline or acidic conditions, which is a vital attribute in order to be able to use the solar hydrogen technology. Numerous efforts, however, have been made regarding the development of photoanodes but with very limited success. For example, applying

metal over-layer thin films such as Pt grain, Au, Pd, and Ru onto the GaAs photoanode surface improved the stability of photoelectrodes to some extent but led to either low repeatability or low PEC performance due to the formation of Schottky barriers (83-85). In contrast, a thin oxide such as Mn-oxide and $SrTiO_2$ or polymer films increase the lifetime stability of GaAs electrodes (86-88). By combining with a NiO_x-based electrocatalyst, amorphous TiO_2 thicker film has suppressed the photodegradation of the GaAs photoanode and produced an evolution of O_2(g) 30 min from water under alkaline conditions (10). On the other hand, a leaky TiO_2 (~143 nm) combined with Ni co-catalyst extended the stability of the GaP photoanode over 6 hours in a 1.0 M KOH electrolyte (10). Moreover, the GaP photoanode was protected via an ALD-TiO_2 and CoO_x co-catalyst, which achieved remarkable stability over 24 h in a 1.0 NaOH electrolyte under one solar sun illumination (71). For the InP photoanode, a sputtering NiO_x thin film deposited onto an InP photoanode surface has been demonstrated, resulting in the onset potential being negatively shifted to 0.86 V versus RHE (23).

1.7. Ternary Alloys of III-V Semiconductor as a Photocathode and Photoanode

Ternary alloys of III-V semiconductor photoelectrodes are promising and have received considerable attention in relation to PEC water splitting because of the tunability of the band gap (82, 89-91). Figure 1.10 shows the mismatch lattice and band gap of various semiconductor alloys. As shown in Figure 1.10, most of the III-V semiconductors can tune the band gap by combining two of the elements.

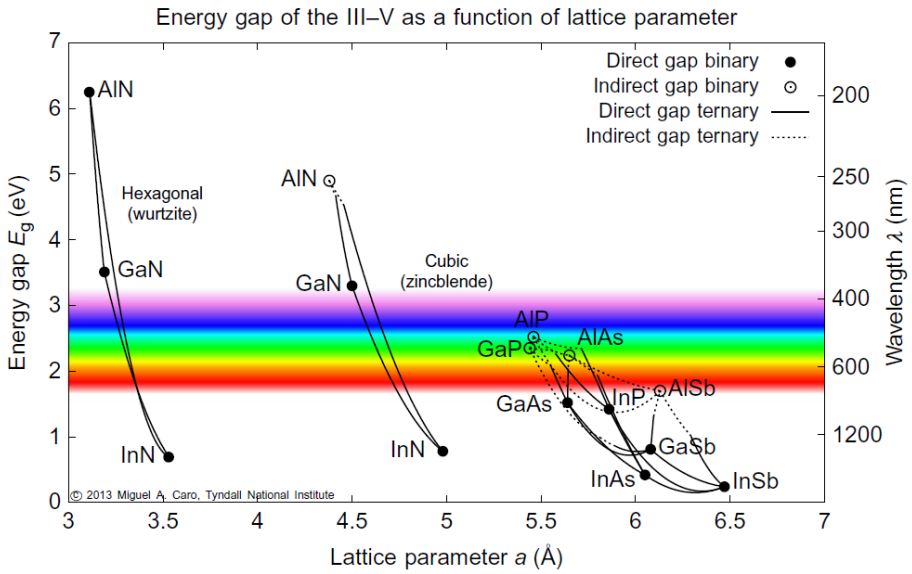

Figure 1.10. Lattice parameter a (Å) and band gap (eV) for a variety of III-V semiconductor materials and their alloys (90).

In order to increase the solar absorption coverage and provide a higher STH efficiency, a combination of two absorber materials can be utilized, in which the large band gap material (~ 1.7 eV) is the top cell to absorb the short wavelength, while a smaller band gap material (~1.1 eV) is the bottom cell to absorb the long-wavelength solar spectrum. In this case of two absorbers (tandem structure), the combination of 1.7 eV and 1.1 eV can achieve the highest theoretical STH efficiency of 27.0% (72, 73).

Figure 1.11 illustrates the tandem structure of two absorber photoelectrodes. $GaAs_{1-x}P_x$ has received much interest as an important ternary alloy material with a tuneable band gap from 1.42 to 2.3 eV, which is suitable for PEC water splitting devices (11, 92). The PEC performance of a p–n homojunction 1.7 eV GaAsP nanowire photocathode has been reported for water reduction. The GaAsP was fabricated by MBE and coated with a nanoparticle of Pt co-catalyst onto the surface of GaAsP, resulting in the shifting of anodic potential in 0.1 M buffer electrolyte (11). Like GaAsP, tuning the band gap of InGaN is feasible. GaN has a large band gap of

~3.4; using indium content to form InGaN can tune the band gap to a visible region and can straddle water oxidation and hydrogen reduction potentials nearly up to the band gap of 1.23 eV, which is thermodynamically required to split water (93-98). Recently, extensive studies have investigated InGaN and GaN photoelectrodes (78, 80, 99-101). For instance, an InGaN nanowire has been demonstrated with high contents up to ~50%, corresponding to a band gap of 1.7 eV. The InGaN nanowire photoanode was passivated with a nanoparticle iridium oxide (IrO_2) co-catalyst that exhibited a high photocurrent density but degraded quickly in solution (95). Co_3O_4 nano-islands coated GaN NW photoanode improved the stability of the electrode and shifted the onset potential (102). Due to incomplete coverage over the electrode surface with nano-islands, the stability was limited under electrolyte conditions. Moreover, cobalt oxyhydroxide phosphate (CoPi) deposited onto the surface of the GaN photoanode obtained a slight improvement by shifting the onset potential but was unstable in aqueous solution (100).

In another example of ternary alloys of III-V materials, the p-GaInP photocathode was investigated by protecting it via TiO_2 and a cobaloxime molecular co-catalyst (22). The photoelectrode exhibited long-term stability and high photocurrent density compared with the GaInP electrode without coating (22). In addition, molybdenum disulphide, MoS_2 coated on the GaInP photocathode and led to long-term stability over 60 h (103).

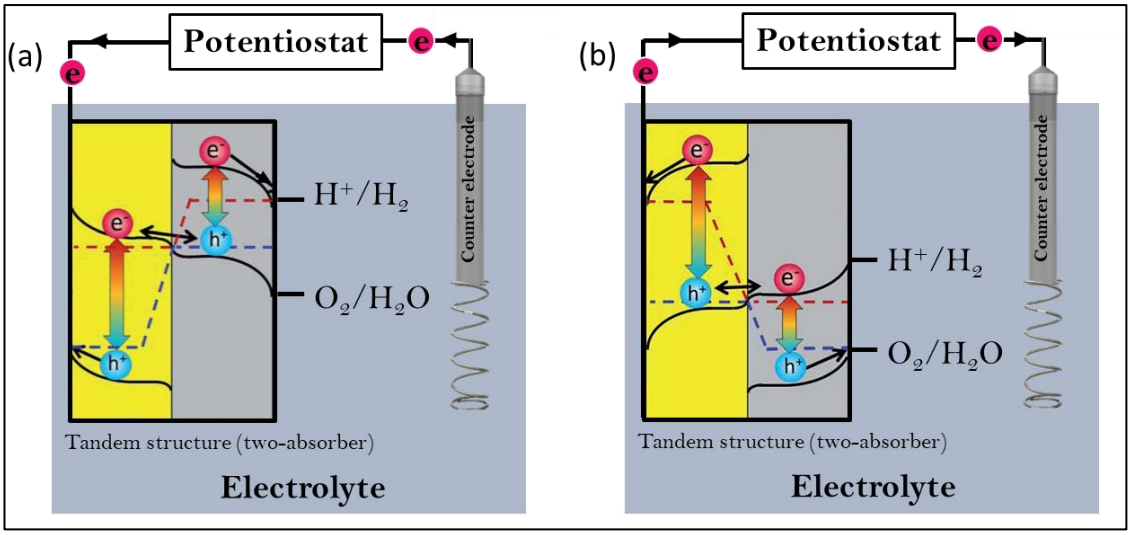

Figure 1.11. Energy diagram of tandem configuration for water splitting. **(a)** Tandem structure of the two-absorber photocathode for water reduction. **(b)** Tandem structure photoanode for water oxidation.

Another system configuration using multiple absorbers to increase the force drive of the water splitting reaction consists of an integrated PEC cell and photovoltaic cell (PV), which is shown in Figure 1.12. The PV cell-assisted photocathode or photoanode can directly perform either a water oxidation or reduction reaction. Recently, a monolithically integrated GaInP/GaInAs photocathode has been reported to have a high STH efficiency of 14% but it gradually degraded during the reaction (104). The PV/PEC GaAs/$GaInP_2$ photocathode was demonstrated and to date holds the highest STH of 12.4% (105). In addition, Verlage et al. reported a monolithically integrated system consisting of a tandem-junction GaAs/InGaP photoanode protected by a TiO_2 and Ni co-catalyst, which achieved a STH of 10.4% (106). A monolithic photoelectrochemical device of a dual-junction tandem photoelectrode was reported with a high STH of 19% (107). The photoelectrode was protected by a crystalline TiO_2 layer and coated with Rh catalyst nanoparticles, but was limited by degradation under electrolyte (108).

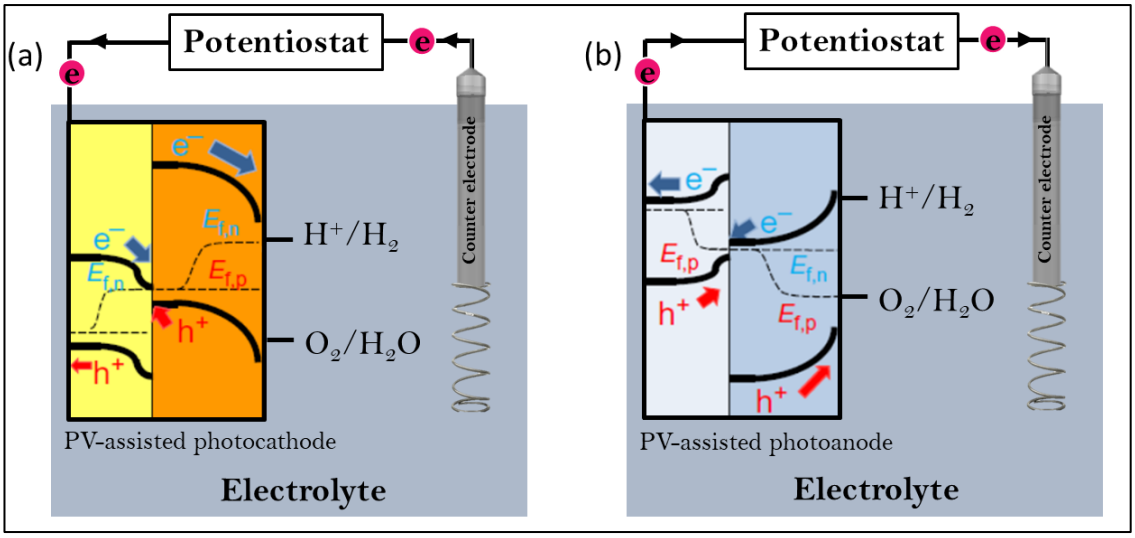

Figure 1.12. Energy illustration for photovoltaic-assisted photoelectrode. **(a)** PV-assisted photocathode for water reduction. **(b)** PV-assisted photoanode for water oxidation.

1.8. Efficiency of PEC Water Splitting

Efficiency is the key factor in determining the performance and characteristics of materials, and it can be used to compare various reported materials (31, 38, 109). There are four primary definitions of PEC water splitting efficiency according to the U.S. Department of Energy (DOE) Office of Energy Efficiency and Renewable Energy: solar-to-chemical conversion efficiency (STH), incident photon-to-current efficiency (IPCE), applied bias photon-to-current efficiency (ABPE), and absorbed photon-to-current efficiency (APCE) (38, 40, 56, 110).

1.8.1. Solar-to-Hydrogen Conversion Efficiency

STH efficiency is the key factor in evaluating the overall STH conversion efficiency. However, the PEC performance of the electrode must be investigated in a two-electrode configuration using the counter electrode (CE) and the working electrode (WE) under one-sun illumination and zero-bias conditions. Zero-bias means that no

voltage is applied between the WE and the CE and that all the energy for the water splitting process is supplied by sunlight. The two electrodes must be immersed in electrolyte with the same pH without any sacrificial reagents. The overall STH conversion efficiency is calculated by (38):

$$STH = \left[\frac{J_{SC}\,(mA/cm^2)\ \times (1.23)(V) \times \eta_{\mathcal{F}}}{P_{total}\ (\,mA/cm^2)}\right] \qquad (1.8.1.1)$$

Where J_{SC} is the short-circuit photocurrent density, 1.23 V corresponds to the Gibbs free energy (ΔG) of the reaction, and $\eta_{\mathcal{F}}$ is the Faradaic efficiency.

1.8.2. Incident Photon-to-current Efficiency (IPCE)

The IPCE describes the photocurrent collected per incident of photon flux as a function of wavelength. Additionally, the IPCE can be estimated by the band gap of the materials. The IPCE is calculated using the following equation (38, 56, 110):

$$\text{IPCE} = \frac{1239.8\ (\,V\ nm\,) \times [\,J\ (mAcm^{-2})\,]}{P_{mono}\,(mW\ cm^{-2}) \times \lambda\ (nm)} \qquad (1.8.2.1)$$

Where J is the photocurrent density, P_{mono} is the power intensity, and λ is the wavelength.

1.8.3. Applied Bias Photon-to-current Efficiency (ABPE)

The ABPE shows the material performance with respect to the applied voltage bias using a two-electrode system consisting of the working electrode and the counter electrode and is given by(56):

$$ABPE = \left[\frac{J_{ph}\,(mA/cm^2)\ \times (1.23 -\ V_b)(V) \times \eta_{\mathcal{F}}}{P_{total}\ (\ mA/cm^2)}\right] \qquad (1.8.3.1)$$

Where J is the photocurrent density, P is the incident illumination intensity (100 mW/cm^2), V_b is the potential versus the counter electrode, and $\eta_{\mathcal{F}}$ is the faradaic efficiency.

1.8.4. Absorbed Photon-to-current Efficiency (APCE)

To understand the performance of the materials, the APCE is useful for assessing the efficiency based on photon absorption without any reflection or transmission photons (29, 56).

Absorptance is estimated with Beer's Law (48):

$$\left[\eta_{e^-/h^+} = \frac{I_o - I}{I_o} = 1 - \frac{I}{I_o} = 1 - 10^{-A}\right] \qquad (1.8.4.1)$$

$$A = -\log\left(\frac{I}{I_o}\right) \qquad (1.8.4.2)$$

$$APCE(\lambda) = \left[\frac{J_{ph}\ (mA/cm^2)\ \times 1240\ (V \times nm)}{P_{mono}\,(mW/cm^2)\ \times \lambda\ (nm)\ \times (1 - 10^{-A})}\right] \qquad (1.8.4.3)$$

Where J_{ph} is the photocurrent density, P_{mono} is the power intensity, and λ is the wavelength.

1.9. Contents of This Thesis

This thesis presents an effective strategy for developing an efficient and stable photoelectrodes (e.g. photoanode and photocathode) based on III-V semiconductor photoelectrodes (such as InGaN, GaP, and $GaP_{1-x}Sb_x$) for PEC water splitting. In the introductory chapter, a comprehensive review of the fundamental principle of PEC water splitting and an introduction to solar water splitting and hydrogen production is presented. Chapter 2 discusses all of the experimental methods in detail, including the structural, optical, and PEC characterizations used in this thesis. Chapter 3 illustrates the fabrication of a GaP photocathode on a silicon substrate grown by molecular beam epitaxy (MBE) and a GaP single-crystalline wafer and compares their PEC water splitting performance. Additionally, an amorphous TiO_2 (~10 nm) layer was deposited onto the surface of the GaP photocathode by atomic layer deposition (ALD) to protect from photocorrosion. An amorphous molybdenum sulfide (MoS_2) co-catalyst was deposited onto the GaP/TiO_2 photocathode to enhance the charge kinetics and stability of the HER in acidic environments. Moreover, the degree of photocorrosion of the GaP photocathode grown on the Si substrate is investigated before and after the PEC test by SEM, AFM, and XPS. Chapter 4 describes a new and promising single-semiconductor light absorber, a $GaP_{1-x}Sb_x$ alloy epitaxially grown on a low-cost silicon substrate for water oxidation by MBE. A thin layer of amorphous TiO_2 and Ni co-catalyst using ALD was deposited onto the surface of the $GaP_{1-x}Sb_x$ photoanode to prevent the corrosion of the photoelectrode, as evidenced by atomic force microscopy, XPS, and PEC water splitting measurements. Chapter 5 describes the InGaN/GaN MQWs photoanode and investigations for water oxidation. The InGaN/GaN MQWs photoanode stabilized for long-term under alkaline condition by modified with cobalt oxide ultra-thin film is described and compared their PEC water splitting

performances. Moreover, the oxidation/photocorrosion of photoanode studied before and after PEC water oxidation by SEM and XPS. Finally, the thesis is summarized and guidelines for future work are discussed.

Chapter 2: Experimental Methods

This chapter describes in detail all of the experimental methods used for materials growth, materials analysis, and the photoelectrochemical techniques used in this research study. Materials such as GaP, InGaN/GaN MQWs, and $GaP_{1-x}Sb_x$ grown on silicon substrates for the PEC device were grown at the Department of Electronic and Electrical Engineering-UCL, University of California, Santa Barbara (UCSB)-Department of Materials, and the University of Rennes, INSA Rennes, CNRS, Institut FOTON–Rennes, France respectively. The material characterization utilized atomic force microscopy (AFM), Raman spectroscopy, photoluminescence (PL), a scanning electron microscope (SEM), energy-dispersive X-ray spectroscopy (EDS), and a scanning transmission electron microscope (STEM) to determine the morphology, crystal structures, and elemental analysis. Atomic layer deposition (ALD) and sputtering equipment were used to form a protection layers and co-catalysts to protect the surface of the photoelectrodes.

2.1. Molecular Beam Epitaxy Growth

The molecular beam epitaxy system (MBE) is an ultra-high vacuum technique used to grow high-quality epitaxial structures with monolayer control especially for III-V semiconductor materials. The system of MBE growth has three main vacuum chambers: a loadlock chamber, a preparation chamber, and a growth chamber. An ultra-high vacuum gate is required to prevent any contamination (111). The principle of MBE growth is the following: it consists essentially of atoms, which are produced by heating up a solid source. They then migrate in an UHV environment and impinge on a hot substrate surface, where they can diffuse and eventually incorporate into the growing film. A schematic drawing of the growth chamber of an MBE device is

illustrated in Figure 2.1. The III-V semiconductor materials for this project were grown by a solid-source Veeco Gen 930 molecular beam epitaxy system, as shown in Figure 2.1(b).

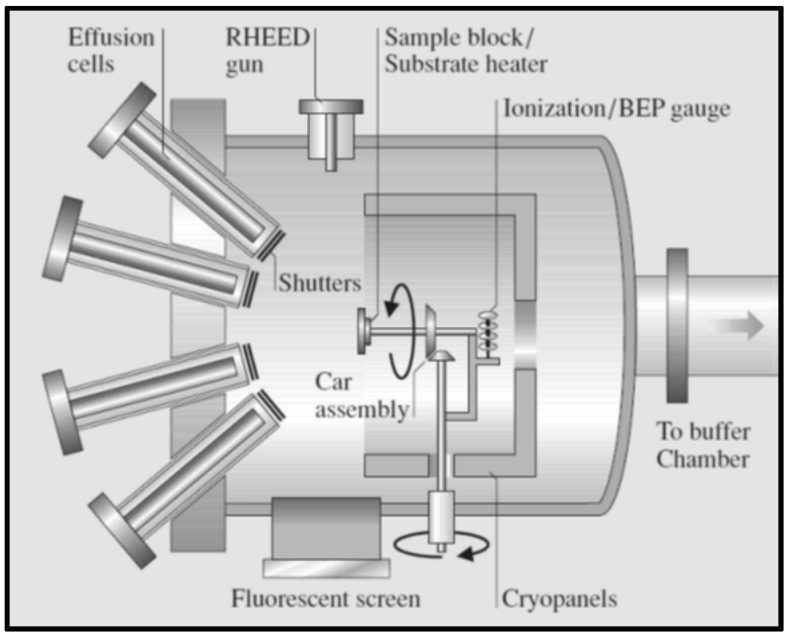

Figure 2.1. (a) Schematic diagram of a molecular beam epitaxy growth chamber. The main experimental feature components of the system are shown (111).

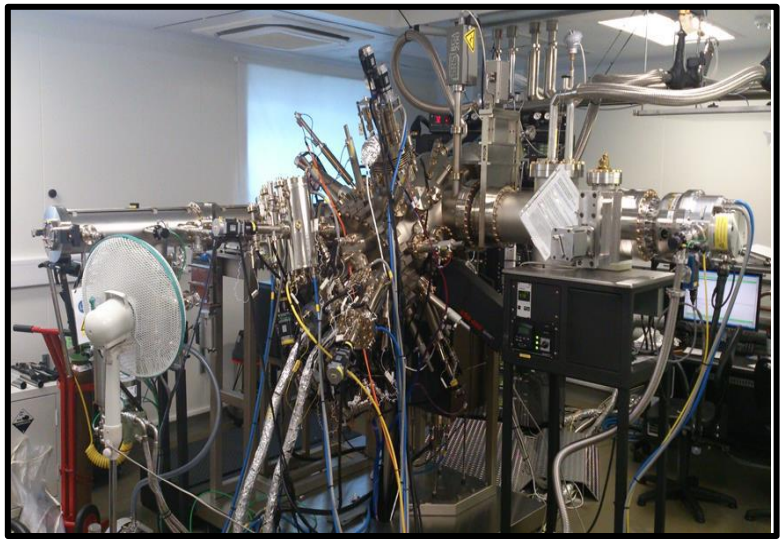

Figure 2.1. (b) Veeco Gen930 solid-source MBE.

2.2. Thin Film Deposition

The synthesis methods to produce efficient catalysts and protection layers on the surface of photoelectrodes are essential to improve PEC performance which is limited by the high overpotentials. The dimensions and synthesis of catalysts onto the surface of photoelectrodes have an influence on aspects of their PEC performance such as stability and efficiency. Several deposition techniques will be discussed in the following section.

2.2.1. Sputter Deposition

Sputter deposition is a physical vapour deposition method which is widely used to deposit thin film metallization on semiconductor materials such as Pt, Ti, Ni, and Au with different thicknesses. In sputtering, the target material and substrate are placed in a vacuum chamber, as shown in Figure 2.2. To initiate plasma generation, high and strong bias is applied between the target (cathode) and substrate (anode), and the plasma is created by ionizing a sputtering gas (generally argon). The plasma collides the sputter target (e.g. Ti, Pt, and Au) and eject the atoms into the chamber. The ejected atoms deposit on top of the sample surface forming a thin film layer (112).

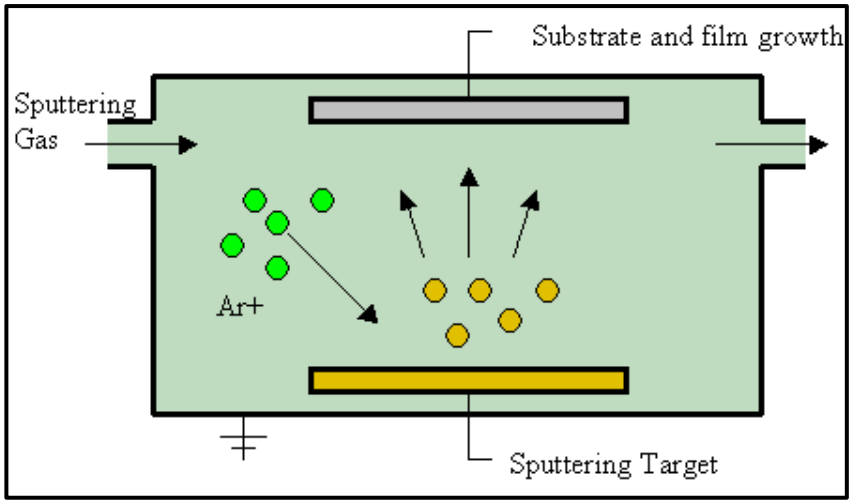

Figure 2.2. Schematic diagram of the sputtering process (112).

2.2.2. Atomic Layer Deposition

Atomic layer deposition (ALD) is a vapour phase technique for depositing thin films of a variety of materials such as metal oxides and noble metals. ALD offers precise control of the thickness at the angstrom or monolayer level. The basic process is illustrated in Figure 2.3. The first precursor is pulsed into the reaction chamber, producing a monolayer on the substrate surface through a self-limiting process. The chamber was purged with an inert carrier gas, usually N_2 or Ar, and the second precursor is pulsed into the chamber to react with the first precursor to produce another monolayer on the substrate surface; this process constitutes a single cycle. This process is repeated to obtain the desired film on the substrate surface (113, 114).

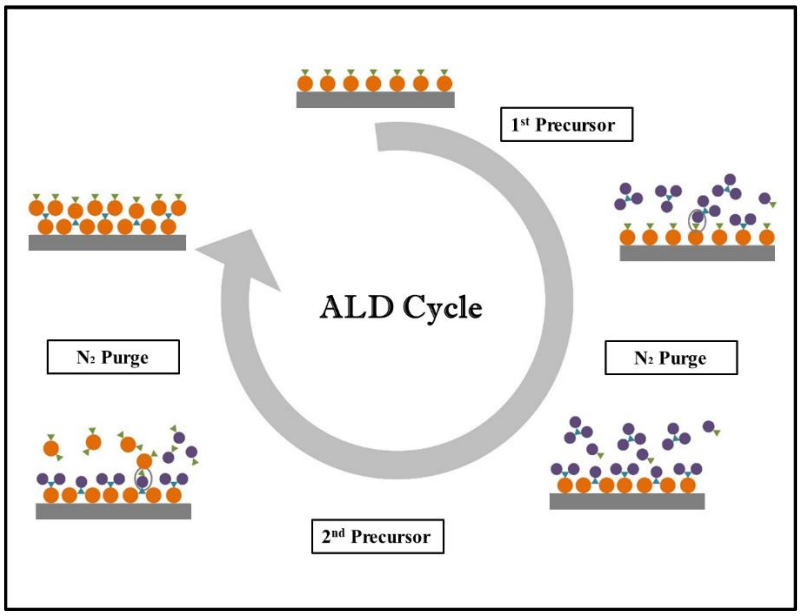

Figure 2.3. Schematic diagram of a single cycle of the atomic layer deposition (ALD) process (113, 114).

2.3. Structural Characterization

2.3.1. Scanning Electron Microscopy (SEM)

To understand the structural morphology of the surface of semiconductor photoelectrodes before and after the PEC water splitting test, it is essential to investigate this using scanning electron microscopy (SEM). The principle of SEM is relativity simple. It utilizes a focused beam of electrons directly across the sample surface, which interact with atoms and result in several signals such as backscattered electrons, secondary electrons, and absorbed electrons. Measuring these signals with suitable detectors reveals information about the sample, including the external morphology (texture), chemical composition, and crystalline structure and orientation of materials (115). To obtain high-resolution SEM images, the sample is coated with an ultrathin layer of gold or by using silver paste to attach the conductive samples to the specimen holder. This layer provides good conduction for nonconductive samples.

In this thesis, SEM images were produced using a Hitachi S-4800 SEM at 3 kV accelerating voltage at EEE UCL. Figure 2.4 shows the SEM images for GaAs combined with TiO_2 and Ni nanorods.

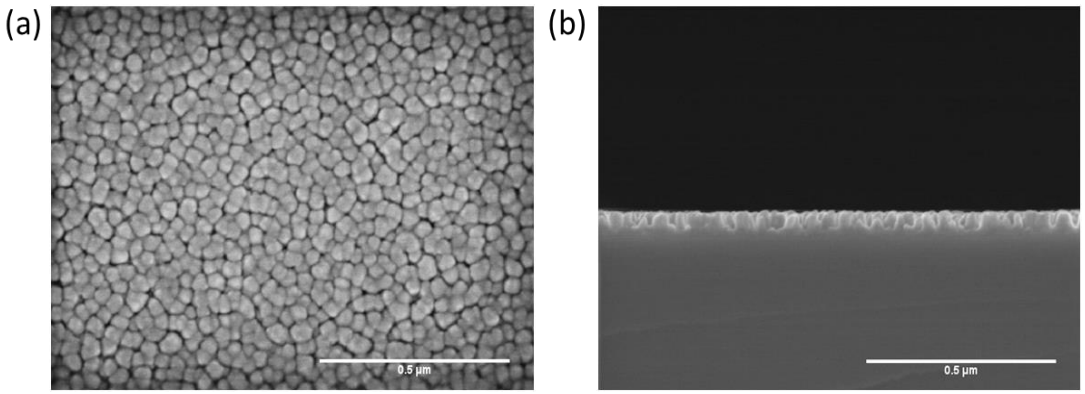

Figure 2.4. Scanning electron microscopy (SEM) images for GaAs combined with TiO_2 and Ni nanorods. **(a)** Plane view and **(b)** cross-section view.

2.3.2. Energy dispersive X-ray spectroscopy (EDX)

Energy dispersive X-ray spectroscopy (EDX) is a technique for elemental composition extraction. In this technique, an energetic electron beam is directed toward onto the desired sample and excite the electrons from the inner shells of the sample atoms. When this occurs, the electron will leave behind a hole that a higher energy electron can fill in with an electron from an outer shell, and it will release energy as it relaxes. At this transfer, X-ray photons are simultaneously emitted specific wavelengths of X-rays that are characteristic of the atomic structure of the elements. Figure 2.5 shows the Energy-dispersive X-ray spectroscopy analysis (EDX) of a GaAs nanowire photoanode.

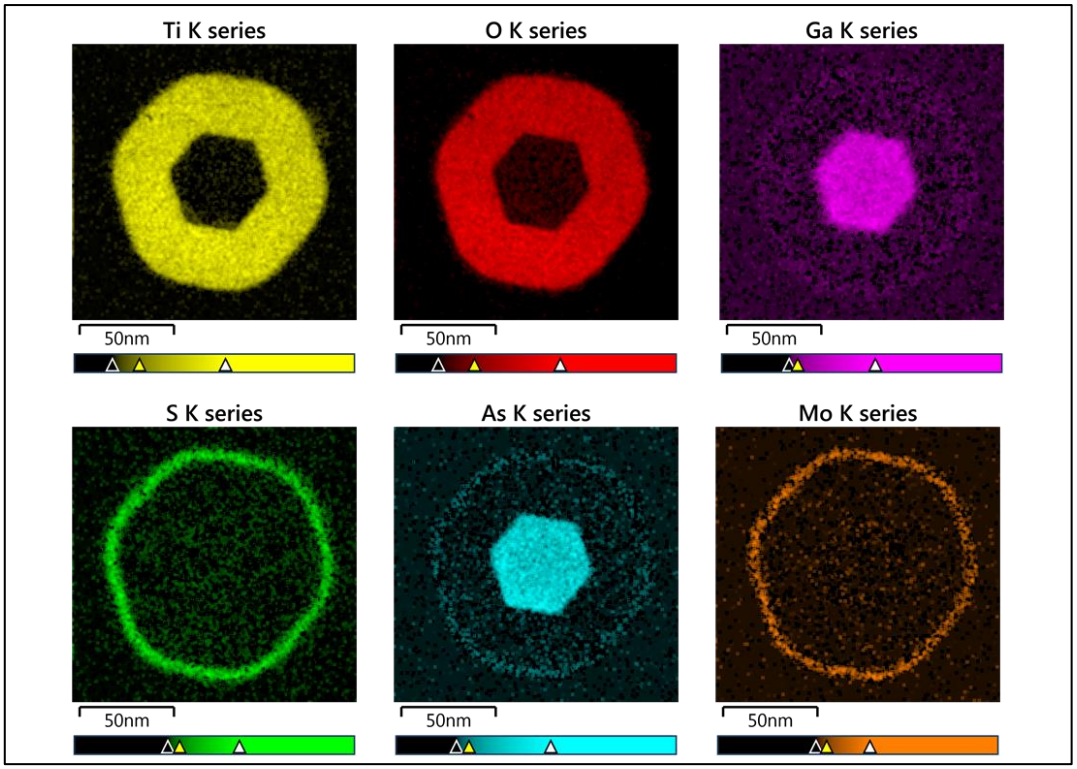

Figure 2.5. Energy dispersive X-ray spectroscopy (EDS) mapping of GaAs core-shell nanowire shows the individual layer thickness associated with the Ti, O, Ga, S, As, and Mo elements.

2.3.3. X-Ray Diffraction (XRD)

X-Ray Diffraction (XRD) is an analytical technique used for identification of crystalline phases which provides detailed information about the internal lattice of crystalline structures, including unit cell dimensions, and crystal defects. In principle, The X-rays are generated in a cathode ray tube by heating a filament and high voltage is applied to accelerate the electrons toward a target material. As shown in Figure 2.6 (a-b), when electrons have high energy to eject electrons of the target material, characteristic X-ray spectra are generated. Thus, the X-rays are directed toward the sample surface and interact with crystal lattice to produce constructive interference if the conditions satisfy the Bragg's Law:

$$n\lambda = 2d \sin\theta$$

Where n is positive integer, λ is the wavelength of the X-ray, d is the interplanar distance, and θ is the incident angle. In this thesis, the XRD measurement was performed by a Jordan Valley D1 X-ray diffraction instrument.

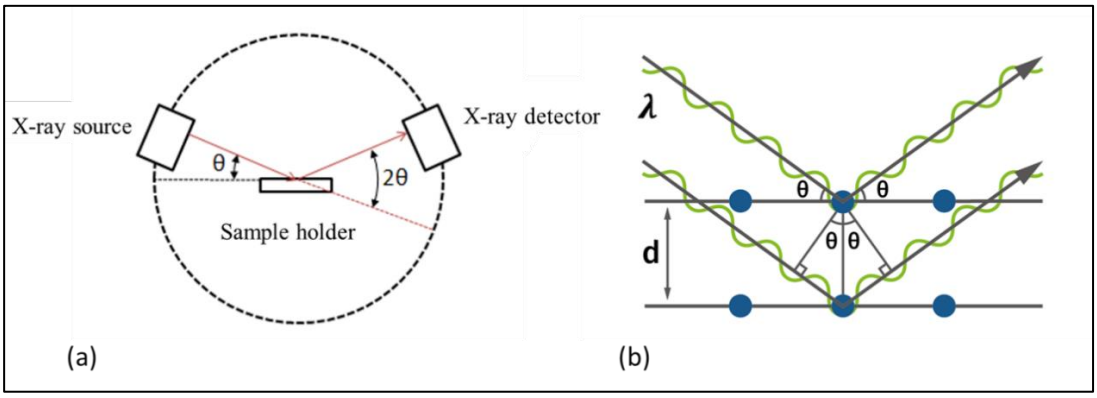

Figure 2.6. (a) Illustration of an X-Ray Diffraction (XRD) system. (b) Illustration of principle of X-Ray Diffraction (XRD) measurements.

2.3.2. Atomic Force Microscopy (AFM)

Atomic force microscopy (AFM) is a useful technique for imaging the surface using a sharp tip to probe the surface features. It can image the height or depth of the surface topography with 1 million times magnification and generate a three-dimensional picture to characterize the surface roughness of the sample (115). In this project, AFM images were produced with a Vecco Dimension V Scanning Probe Microscope with tapping mode at atmospheric pressure and a Si cantilever with a 10 nm radius. Figure 2.7 shows AFM images of the surface of a GaP film grown on a Si substrate.

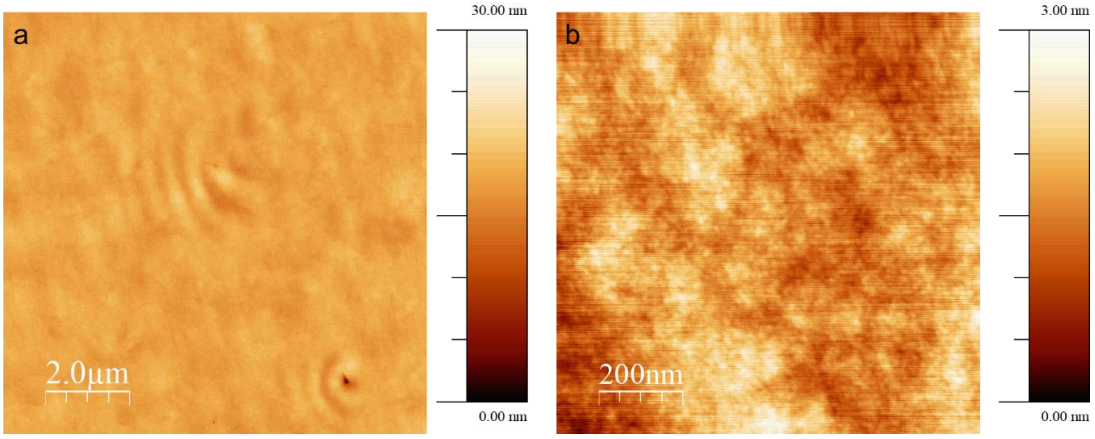

Figure 2.7. Atomic force microscopy (AFM) images of a GaP thin film directly grown on a silicon substrate. (**a)** 10 × 10 µm^2 and (**b)** 1 × 1 µm^2. The z-scale is 30 nm and 3 nm for the AFM images in (a) and (b), respectively. The root mean square roughness measured from the AFM images in (a) and (b) is 0.8 nm and 0.39 nm, respectively.

2.3.3. X-Ray Photoelectron Spectroscopy (XPS)

X-ray photoelectron spectroscopy (XPS) is an important technique for obtaining information about the composition of materials and for investigating the influence of chemical composition on the photoelectrode surface before and after the PEC water splitting test. This technique is based on the photoelectric effect, whereby an Al source X-ray beam hits the sample surface and ejects a core-level electron. The kinetic energy of the ejected electrons is measured, and the electron binding energy can be calculated. In this project, XPS was performed using a Thermo Scientific K-alpha spectrometer with monochromated Al K < radiation, a dual-beam charge compensation system, and constant pass energy of 50 eV (spot size 400 µm). Survey scans were collected in the range 0–1200 eV.

2.4. Optical Characterization

2.4.1. Photoluminescence

Photoluminescence (PL) is a characterization technique widely used on various semiconductor materials such as epitaxially grown III-V semiconductors and nanostructures such as quantum wells and nanowires. PL is a useful technique that offers insight into the band structure and material quality of semiconductor layers. In PL measurement, the light is impinged onto the surface of the semiconductor and electron jumps to the higher electronic states and then releases energy (photons) as it relaxes and returns to a lower energy level. This emission of light is so-called PL. In this project, the excitation source is a laser diode operating at 405 nm and laser spot size diameter on the sample is about 50 µm and the power is 9.3 mW. The luminescence signal was collected using an IHR 320 spectrometer with 300 mm^{-2} grating and an open-electrode Si CCD. The entrance slit of the spectrometer was set to 100 µm.

2.4.2. Raman Spectroscopy

Raman spectroscopy is a vibrational spectroscopic technique used to provide information about a material, such as its crystal structures, dopant concentration, and orientation. The Raman technique is conducted by illuminating the sample with laser radiation (usually IR or UV). This light interacts with the sample by vibration and generates a quantity of Raman scattered light. The light incidence on the sample surface can be reflected, absorbed, or scattered. Most scatter light is an elastic process, which means no change in energy while the inelastic process can be shifter up or down compared to original of photon energy (115). In this thesis, Raman studies were

conducted using a Renishaw 1000 spectrometer equipped with a He-Ne laser (λ = 633 nm). Other wavelengths were used with a Renishaw inVia Raman microscope equipped with multi-wavelength lasers of 325, 465, 514.5, and 785 nm. Both instruments were coupled to a microscope with a 50× objective. The Raman system was calibrated using a silicon reference. The acquisition time of all Raman measurements is 10 s unless stated otherwise. Raman scattering spectra were recorded in a range of 150–2000 cm^{-1} and up to 3200 cm^{-1} for the samples.

2.5. Photoelectrochemical Techniques

2.5.1. Electrode Fabrication

In order to form low-loss electronic contact (e.g. ohmic contact), before the PEC experiments layers of suitable metals were deposited onto the back side of the sample using a sputter deposition system and annealed by rapid thermal annealing (RTA) at a certain temperature and time. Then, the sample was attached by a copper wire using silver paste and covered by insulating epoxy, as shown in Figure 2.8.

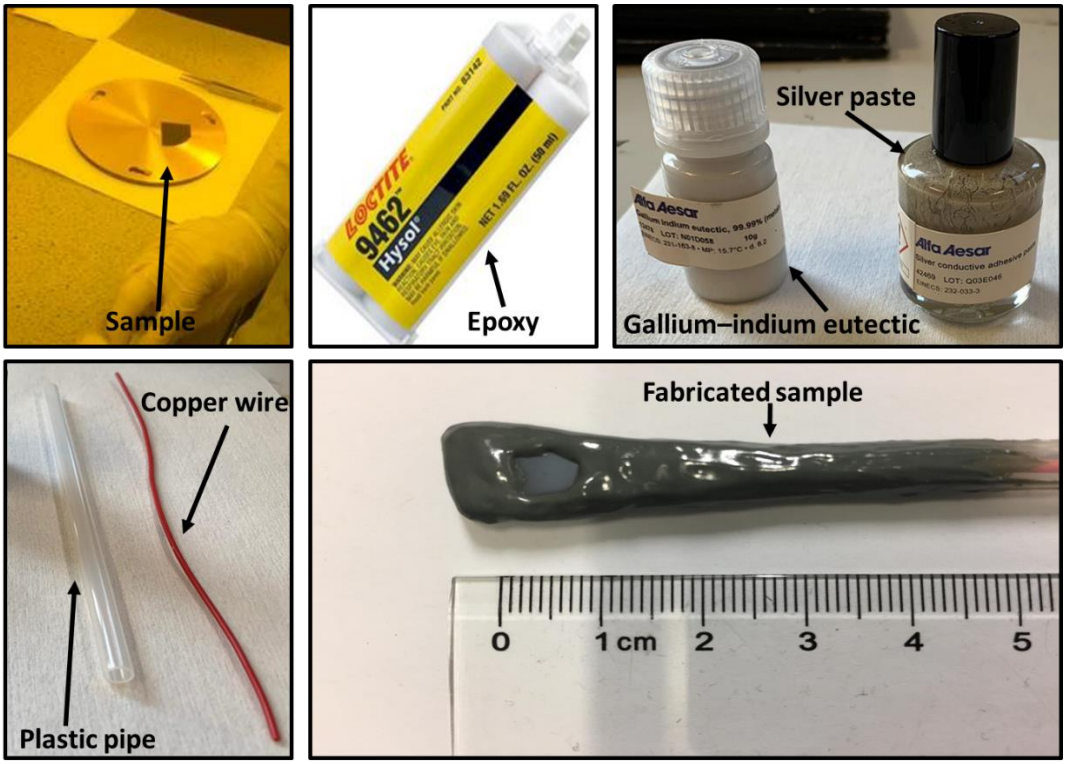

Figure 2.8. Main steps in PEC electrode fabrication. The electrode was attached by a copper wire using silver paste and covered by insulating epoxy. A ruler is used to set the scale for the surface area determination.

2.5.2. PEC Measurement Setup

In order to investigate the PEC properties and performance of photoelectrodes, a three-electrode configuration including the working electrodes, silver/silver chloride ($Ag/AgCl$) as the reference electrode, and a Pt coil or mesh as the counter electrode were used without any sacrificial agent. The photoelectrochemical cell setup is shown in Figure 2.9. Additionally, a 200 W Xe arc lamp (66477-200HXF-R1 Mercury-Xenon) was used as a light source with an AM 1.5 G filter to one sun based on the $AM\ 1.5G$ standard. The current-potential characteristic, IPCE, ABPE, and stability of electrodes were measured by potentiostat (Ivium technology) throughout the study.

The measured potentials versus Ag/AgCl were converted into the reversible hydrogen electrode (RHE) scale using the following Nernst equation:

$$V_{RHE} = V_{Ag/AgCl} + 0.059 \times pH + V_{o\ Ag/AgCl}$$

Where $V_{Ag/AgCl}$ the potential is experimentally measured versus Ag/AgCl reference electrode, and $V_{o\ Ag/AgCl}$ is the standard potential of Ag/AgCl at 25 °C (0.1976 V vs. RHE).

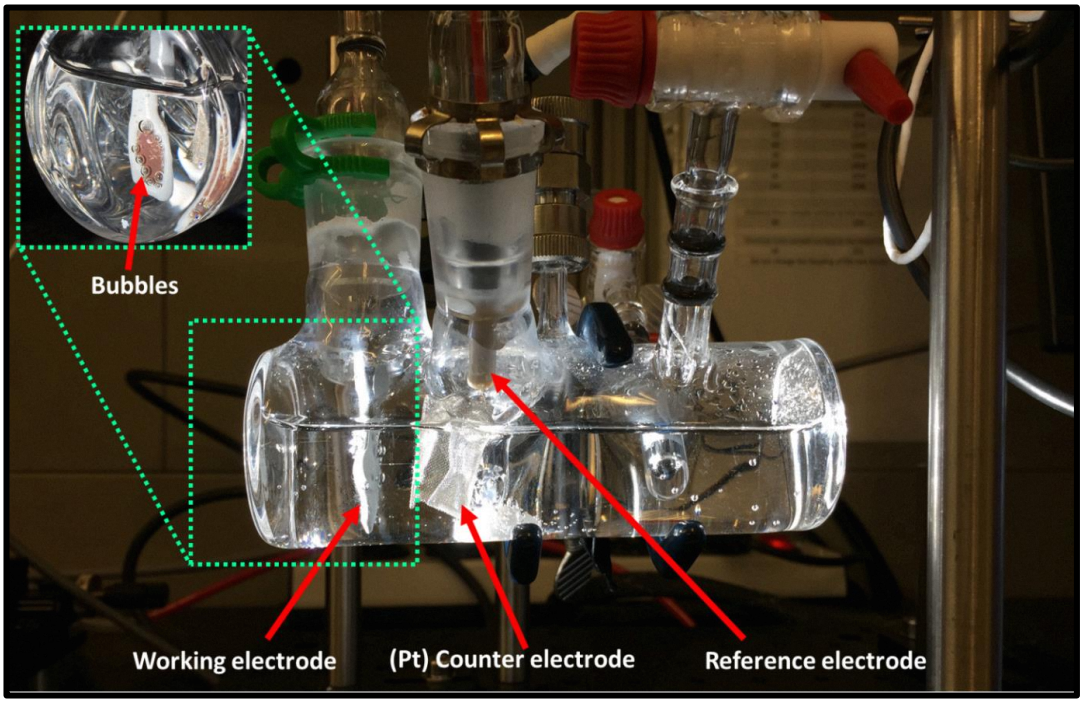

Figure 2.9. Schematic diagram of the experimental setup used for the PEC measurements, consisting of the working electrode, reference electrode (Ag/AgCl), and counter electrode (platinum coil) in one PEC cell.

2.5.3. Gas Chromatography (GC)

The chemical products (e.g. hydrogen and oxygen gases) of PEC water splitting processes can be detected through gas chromatography (GC). GC analysis is a sensitive and powerful technique for the quantitative detection of Hydrogen and Oxygen in the gas phase and provides direct evidence for solar-to-hydrogen (STH) efficiency measurements. A schematic diagram of GC is shown in Figure 2.10. For gas injection, a conventional method is to fill a syringe with a known amount of gas product from the headspace of the electrochemical cell and inject it through the injector port. The gaseous sample is carried by a carrier gas and separated by a column. Since different gases have a different retention time in the column, individual gases can be detected by a detector, followed by signal generation via a data recorder. In this thesis, A Varian 450- Gas Chromatography (GC) equipped with flame ionization detector (FID) and thermal conductivity detector were used to measure the products of hydrogen (H_2) and oxygen (O_2).

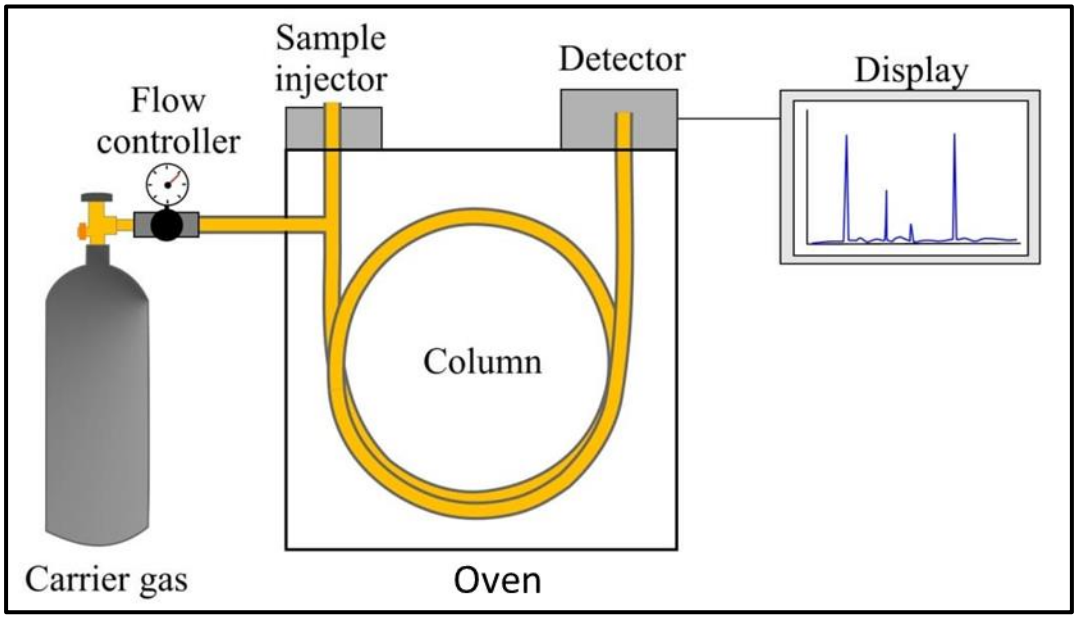

Figure 2.10. Schematic diagram showing the main parts of a gas chromatograph (56).

Chapter 3: GaP Photocathode Grown on a Silicon Substrate by Molecular Beam Epitaxy (MBE) for Water Reduction

A gallium phosphide (GaP) photocathode is an attractive photocathode for PEC water splitting due to a high conduction band energy, large photovoltage, relatively high carrier mobility, and a suitable band gap (2.25 eV), which can split water without application of an extra voltage. This chapter describes how a high-quality GaP photocathode was directly grown on a silicon substrate by solid-source molecular beam epitaxy (MBE). The GaP photocathodes were passivated by titanium dioxide (TiO_2) and MoS_2 was deposited by atomic layer deposition to protect the surface of GaP from the electrolyte and to promote the charge transfer. The structures of GaP photocathodes were investigated by high-resolution XRD, STEM-EDS, PL, and STEM. Additionally, the GaP photocathodes were investigated for photoelectrochemical water splitting using linear sweep voltammetry, chronoampeometry, and chronopotentiometry, as well as microscopy studies being carried out using scanning electron microscopy (SEM), atomic force microscopy (AFM), and X-ray photoelectron spectroscopy (XPS) before and after the PEC measurements.

3.1. Introduction

PEC water splitting is a promising and sustainable approach for clean energy generation by using sunlight to simultaneously generate hydrogen (H_2) and oxygen (O_2) (19, 26, 36, 116). Based on the free energy required to split water, a semiconductor must have a sufficient energy band gap greater than 1.23 eV and suitable band edges that straddle the redox potentials for water splitting (19, 21, 29, 40, 117, 118). Recent studies of solar hydrogen technologies show that the cost of

hydrogen production can be reduced by decreasing the cost of photoelectrodes combined with enhancing their efficiencies (28, 119-121). However, the development of low-cost, efficient, and stable semiconductor photoelectrodes is still a great challenge. For instance, wide band gap metal oxides, such as TiO_2 and $SrTiO_3$, absorb a small part of the solar spectrum and therefore only low solar-to-hydrogen (STH) conversion efficiency can be achieved (1-3, 63, 122, 123). On the other hand, group III-V semiconductors are efficient photoelectrodes for PEC water splitting owing to their superior optical properties and appropriate band gaps in the visible range, but their performance over time is limited by photocorrosion in the alkaline or acidic electrolyte solutions (10, 11, 15, 16, 22, 24, 65, 67, 72, 73, 103). Additionally, the relatively high cost of III-V materials cannot meet the demands for economic hydrogen production. III-V semiconductors are generally grown on native III-V substrates, which are a few orders of magnitude more expensive than Si substrates. Given the dominant role of Si in the photovoltaic industry and the possibility of using III-V/Si tandem PEC cells, hetero-integration of III-V semiconductors and Si is an attractive approach for the production of cost-effective and efficient PEC cells.

A silicon substrate is not typically used for the heteroepitaxy of III-V semiconductors due to the lattice mismatch and incompatible thermal expansion coefficients, which leads to a high density of threading dislocations. Recently, some III-V semiconductors, such as gallium phosphide (GaP), have been shown to overcome these obstacles due to the low lattice mismatch between GaP and Si (0.36% at room temperature) (124). Furthermore, GaP is an attractive photocathode for PEC water splitting due to a high conduction band energy and a suitable band gap (2.25 eV), which can provide a maximum photocurrent density of 10 (mA/cm^2) under one-sun solar illumination (30, 72, 73, 125, 126). In particular, a few studies on GaP photocathodes and photoanodes

have been carried out (14, 15, 127-131). For example, a GaP photocathode has been shown to have a high open circuit voltage of 710 mV versus a reversible hydrogen electrode (RHE) when using it in a heterojunction with a n-TiO_2 layer in an acidic aqueous solution under one-sun illumination (14). Distinct improvements in the performance of GaP photocathodes have also been shown by using Pt-modified GaP nanowires (NWs) grown on commercial single-crystalline GaP wafers (15). Despite the relatively high performance, prior work on GaP photocathodes has primarily focused on commercial single-crystal wafers, which limits the practical use due to their prohibitive cost.

In this chapter, a high-quality GaP photocathode was directly grown on a silicon substrate by solid-source molecular beam epitaxy (MBE). The GaP grown on Si substrate photocathodes were investigated for photoelectrochemical water splitting and compared to GaP single crystalline commercial wafer photocathodes. Moreover, different protection layers and co-catalysts were used to stabilize the Si/GaP photocathodes and compared to GaP single crystalline photocathodes. Overall, this approach indicates that both the good efficiency and stability of the Si/GaP photocathodes are advantages of the hetero-integrated III-V semiconductor materials on Si substrate.

3.2. Experimental Method

Fabrication of GaP photocathodes: For the single-crystalline reference GaP photocathode, Ti/Au (50/100 nm) metals were deposited on the back side of the GaP sample by thermal evaporation as an ohmic contact to collect the holes generated from the photoelectrode. The contact metals were alloyed at 400 °C for 10 s by rapid thermal annealing to form a good ohmic contact. The GaP photocathode grown on the

Si substrate was fabricated by etching down the GaP top layer on the side and depositing Ti/Au (50/100 nm) metals on the exposed GaP bottom layer. Before the PEC experiments, the electrodes were attached by a copper wire using silver paste and covered by insulating epoxy.

Photoelectrochemical measurement: The PEC performance of all p-GaP photocathodes was evaluated in a three-electrode configuration in 1 M perchloric acid $HClO_4$ (pH 0) including the working electrodes, silver/silver chloride (Ag/AgCl) as a reference electrode, and a Pt coil as a counter electrode without any sacrificial agent. A 200 W Xe arc lamp (66477-200HXF-R1 Mercury-Xenon) was used as a light source with AM 1.5G filter to one sun based on the AM 1.5G standard. The illumination intensity was calibrated using a silicon reference cell with a power meter (Thorlabs, Model PM100A). The measured potentials versus Ag/AgCl were converted to the reversible hydrogen electrode (RHE) scale using the following equation:

$$V_{RHE} = V_{Ag/AgCl} + 0.059 \times PH + V^{0}_{Ag/AgCl}$$

Where $V_{Ag/AgCl}$ the potential is experimentally measured versus the Ag/AgCl reference electrode, and $V^{0}_{Ag/AgCl}$ is the standard potential of Ag/AgCl at 25 °C (0.1976 V versus RHE). Before the PEC experiments, the electrolyte was purged by Ar for 30 min. All linear sweep voltammetry measurements with a scan rate of 50 mV s^{-1} were performed under both dark and illumination conditions using Ivium CompactStat. The incident photon-to-current conversion efficiency (IPCE) measurement at each wavelength for the photocathodes was taken using the same three-electrode setup equipped with a monochromator at -0.80 V versus RHE.

Hydrogen measurements: Hydrogen was detected in the gas phase using a Clark electrode (Unisense, Denmark) while the photoelectrode was held at a constant

potential and one-sun illumination in a gas-tight PEC cell consisting of the GaP working electrode, a Ag/AgCl reference electrode, and a Platinum mesh counter electrode immersed in 0.1 M H_2SO_4 (pH 1.1). The O_2 and H_2 microsensors connected the microsensor monometer. Then the microsensors placed in the lid of the electrochemical cell and lowered the sensors into the sample. Prior to taking gas measurements, the PEC cell was purged with nitrogen (99.999% pure, BOC) such that the oxygen sensor (Unisense, Denmark) showed a sufficiently low voltage indicative of only trace amounts. Then the N_2 flow was cut, the cell was sealed and after 5 min the chronoamperometric measurement under illumination started. After the H_2 measurement was taken, a calibration of the Clark electrode was carried out, injecting known volumes of H_2 into the same PEC reactor using a gas-tight syringe. The Faradaic efficiency (FE) was calculated according to FE = nNF/Q where n is the number of moles of H_2, N is the number of electrons in the reaction (= 2 for proton reduction), F is the Faradaic constant (= 96485 C/mol), and Q is the charge passed through the working electrode (calculated from the current produced in the chronoamperometry measurement).

Atomic layer deposition of TiO_2: Atomic layer deposition of amorphous TiO_2 thin films on the Si/GaP substrate was obtained by a home-built ALD system using titanium isopropoxide (TTIP) as the metal precursor and water as the precursor (132). TTIP was kept at room temperature (25 °C) while water was kept at 5 °C. The deposition temperature was maintained at 150 °C. Each ALD cycle consisted of a 2 s TTIP pulse, a 1 min argon purge, and then followed by a 2 s water pulse and a 3 min argon purge. The gas flow rate was set to 70 standard cubic centimetres per minute (sccm). The growth rate of the ALD process through this system was approximately 0.4 Å/cycle.

Atomic layer deposition of MoS_2: The MoS_2 layer was also deposited by the ALD system using $MoCl_5$ and H_2S mixed gas (4 mol%, with N2 gas) as the molybdenum and sulfur precursor, respectively. $MoCl_5$ was kept at 70 °C and injected with Ar (50 sccm) carrier gas. H_2S mixed gas was injected with a flow rate of 30 sccm without carrier gas. Each ALD cycle consisted of a 0.2 s $MoCl_5$ pulse and 0.2 s H_2S pulse separated a 15 s Ar purge step. Deposition temperature was kept at 250 °C and the growth rate was approximately 0.6~0.7 Å/cycle

Sputtering of platinum: Platinum catalysts were deposited using a sputter deposition system with a background pressure below 5×10^{-8} Torr. Deposition conditions were as follows: power 75 W, target voltage 436 V, and target current 0.15 A. The growth rate was 4 nm/min[1].

Material characterization: For cross-sectional TEM imaging of the thick GaP structures on Si, samples were prepared using mechanical polishing followed by ion-milling in a Fischione 1010 ion mill. A FEI Titan 80-300S TEM at 300 kV, fitted with a CEOS image corrector, was used to perform the observations. The high-resolution scanning TEM (STEM) images of the surface protection layer and catalysts were obtained using a Hitachi HD2700 TEM operated at 200 kV in bright-field modes. Energy-dispersive X-ray spectroscopy (EDS) data was acquired using a Bruker Quantax system. The STEM sample was prepared by a FEI FIB200 focused ion beam and thinned to electron transparency. Scanning electron microscopy (SEM) analysis was carried out using a Hitachi S-4800 SEM at 3 kV accelerating voltage. The AFM images were acquired with a Vecco Dimension V Scanning Probe Microscope with tapping mode at atmospheric pressure with a Si cantilever with a 10 nm radius. X-ray photoelectron spectroscopy (XPS) measurements were performed with a Thermo

monochromated aluminium k-alfa photoelectron spectrometer, using monochromic Al-Kα radiation (1486.7 eV). Survey scans were collected in the range of 0–1300 eV. High-resolution peaks were used for the principal peaks of Ga, P, Ti, O, Mo, S, and Pt. The area underneath these bands is an indication of the concentration of the element within the region of analysis (spot size 400 μm). Data was analysed using CasaXPS software.

3.3. Results and Discussion

3.3.1. Growth of the GaP Photocathode on Silicon Substrate

GaP thin film was directly grown on silicon substrate with a 4° offcut to the [011] orientation was used for the heteroepitaxy by a solid-source Veeco Gen 930 molecular beam epitaxy system. Prior to epitaxy growth, the silicon wafer was thermally annealed at 900 °C for 5 min to remove the silicon native oxide and form double atomic steps on the silicon surface to avoid the formation of antiphase domains (APDs). The GaP layer was grown in a two steps procedure after high-temperature thermal treatment of the silicon wafer, a 5 nm GaP nucleation layer was deposited by migration-enhanced epitaxy at a low-growth temperature of 440 °C. Two layers of low-temperature GaP were then grown at 440 °C and 500 °C for 20 nm and 100 nm, respectively. Finally, a 4 μm GaP layer doped with Be (Beryllium) was grown at 580 °C. Figure 3.1(a) shows a cross-sectional transmission electron microscopy (TEM) image of the Si/GaP interface. A sharp interface with no antiphase boundary was observed.

3.3.2. Structural Characterization of GaP on a Silicon Substrate Photocathode

The structural properties of the GaP thin films grown on silicon were analysed by scanning transmission electron microscopy (STEM). Figure 3.1(a) shows a cross-sectional STEM image of the GaP/Si interface. A sharp interface with no antiphase boundary was observed. A cross-sectional scanning STEM image of the GaP/Si heterostructure in a large area at low magnification is shown in Figure 3.1(b). Although a high density of threading dislocations was generated at the GaP/Si interface, only a small number of dislocations propagated towards the upper part of the GaP film. The threading dislocation density in the upper GaP layer was estimated to be only ~ 1-3×10^6 cm^{-2} by STEM measurements, despite no dislocation filter layers being used in the buffer. This value is in agreement with the pit density measured from a 10 μm × 10 μm AFM image in Figure 3.1.

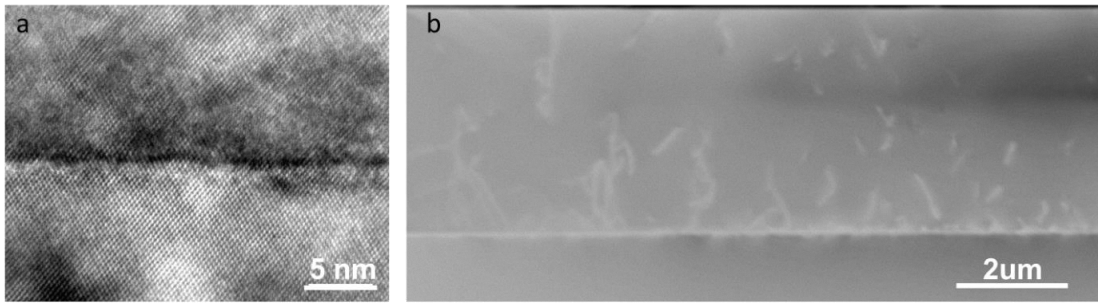

Figure 3.1. Structural characterization of a GaP thin film grown on a silicon photocathode. **(a)** Cross-sectional HRTEM image of the GaP/Si interface. The scale bar is 5 nm. **(b)** High-angle annular dark-field (HAADF) STEM image of the GaP epilayer grown on a Si substrate. The scale bar is 2 μm.

Atomic force microscopy (AFM) is an excellent characterization method with nanoscale resolution to assess the surface morphology. An AFM image of the GaP film grown on a silicon substrate is shown in Figure 3.2(a). The AFM image shows a very flat surface with a root mean square roughness as low as 0.39 nm. A large-scale AFM image also confirms that the GaP film was highly smooth and free of APDs, as shown in Figure 3.2(b).

Figure 3.3(a-b) shows a small number of threading dislocations, terminating at the surface. Most of the dislocations were annihilated in the epilayer, but some of the threading dislocations propagated towards the surface and terminated at the surface pits. The density of dislocations propagating from the interface is very similar to the density throughout the entire structure. The AFM image over the 10 μm × 10 μm scan region gives a low density of threading dislocation in the order of 2×10^6 cm^2, which supports the STEM and XRD measurements in Figure 3.4.

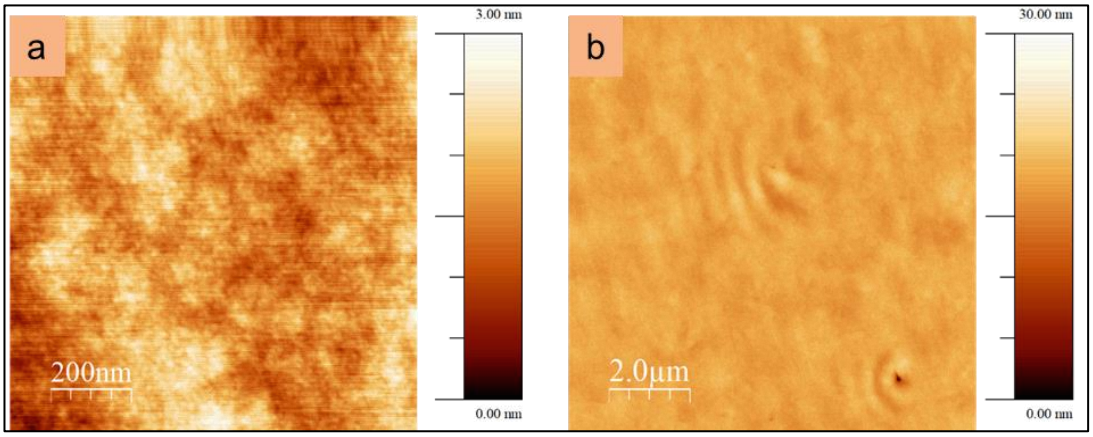

Figure 3.2. Atomic force microscopy (AFM) images of the GaP thin film directly grown on a silicon substrate. **(a)** 10 × 10 μm^2 and **(b)** 1 × 1 μm^2. The z-scale is 30 nm and 3 nm for the AFM images in (a) and (b), respectively. The root mean square roughness measured from the AFM images (a) and (b) is 0.8 nm and 0.39 nm, respectively.

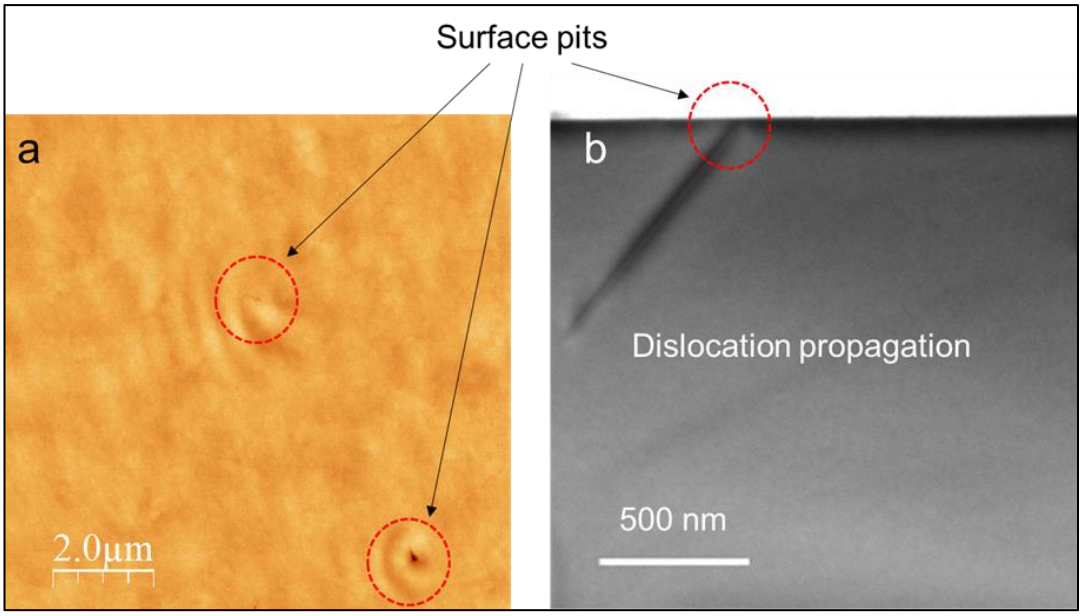

Figure 3.3. Surface morphology of GaP thin film grown on a silicon photocathode. **(a)** Atomic force microscopy (AFM) image of the surface topography of the GaP thin film grown on a silicon substrate. **(b)** A STEM bright-field image of the GaP thin film grown on a silicon substrate.

To further investigate the material properties of GaP grown on silicon, symmetric (004) X-ray ω-2θ scans of the GaP film grown on Si were performed; the XRD pattern of GaP grown on silicon is shown in Figure 3.4. Figure 3.4 shows the ω-2θ curves for the Si (004) and GaP (004) reflections, respectively. The GaP (004) peak shows full width at half maximum (FWHM) as narrow as 162 arc sec. The FWHM is directly related to the dislocation density, and the low value of the FWHM indicates a low density of dislocations.

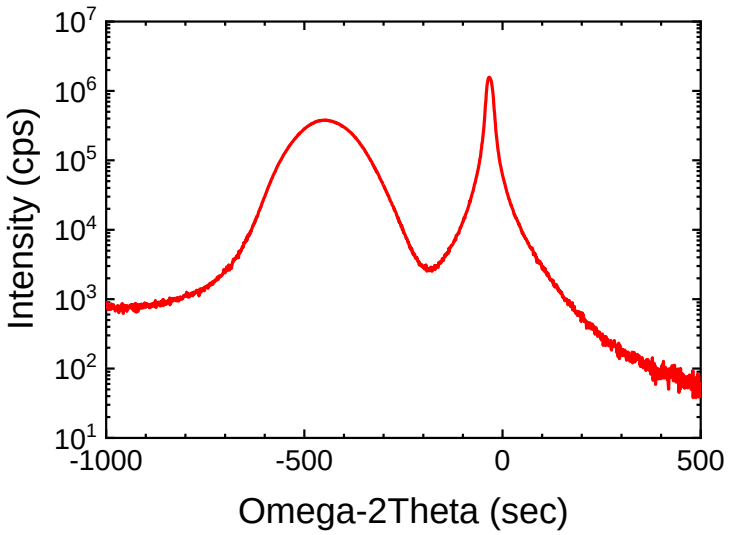

Figure 3.4. High-resolution X-ray diffraction of the GaP film grown on a silicon substrate.

Additionally, the optical properties of a single-crystalline GaP wafer (black curve) and the GaP film grown directly on the Si substrate (red curve) were further studied using photoluminescence (PL) spectroscopy, as shown in Figure 3.5(a). Like the GaP wafer, the broad PL peak of the GaP/Si film can be fitted with two peaks in Figure 3.5(b). The primary emission peaks for both the GaP wafer and the GaP/Si film were located at approximately ~600 nm (2.1 eV), which corresponds to the emission from dopant states close to the band edge (133). A weak peak was observed at around 550 nm (2.25 eV), which matches the primary indirect energy gap of GaP. The GaP/Si film remains at about 50% of the PL intensity for the peak at 600 nm and nearly unchanged PL intensity at 550 nm, compared with the GaP wafer. The reduced PL at 600 nm of the GaP/Si sample may be due to a lower doping concentration in the GaP film-grown Si. On the other hand, the nearly unchanged emission intensity at 550 nm indicates a good optical property of the GaP film grown on the silicon wafer.

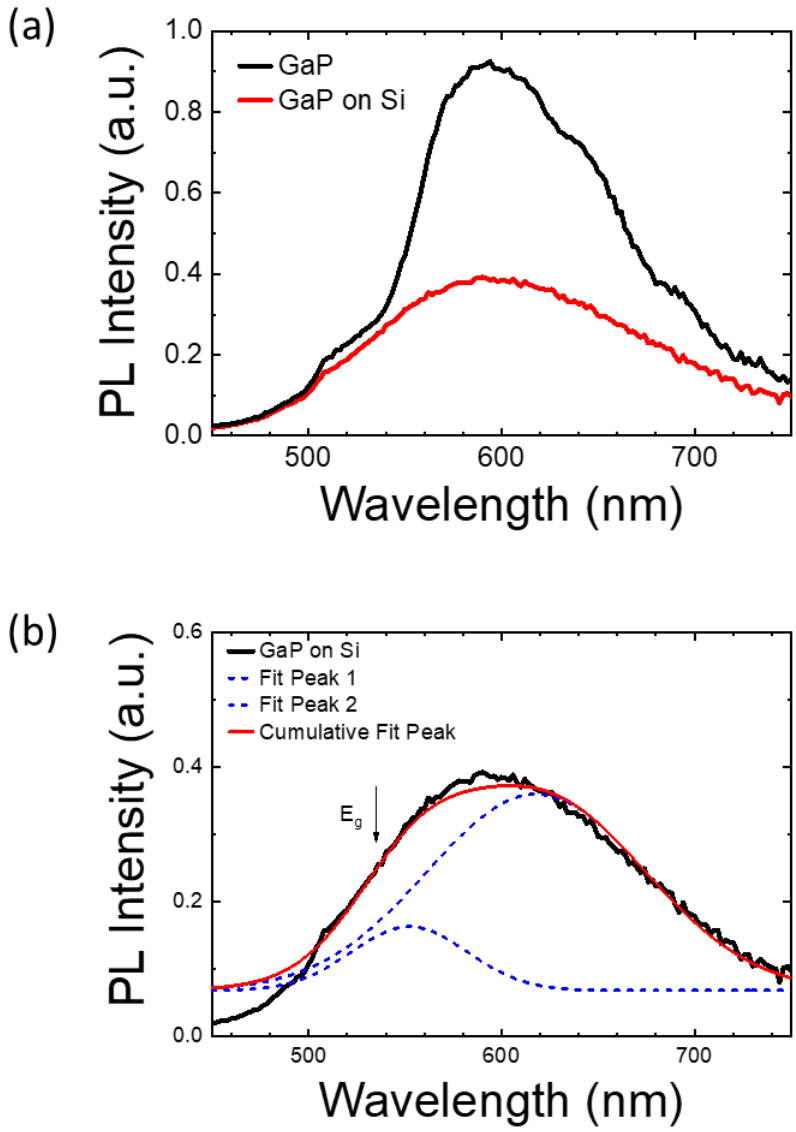

Figure 3.5. Photoluminescence spectra of a GaP single-crystal wafer and GaP on silicon. **(a)** PL spectra of a GaP wafer (black curve) and the GaP film (red curve) grown directly on a silicon substrate at room temperature. **(b)** Fitting of the photoluminescence spectrum of the GaP grown on Si. The first peak at around 550 nm corresponds to the band gap of GaP.

3.3.3. Structural Modification of the GaP Photocathode with Pt Co-catalyst

It is commonly known that III-V semiconductors, e.g. GaP, are readily susceptible to corrosion in aqueous solution during PEC water splitting (10, 14, 15, 127, 128). Therefore, it is important to have a suitable protection layer as well as a catalyst to accelerate the charge transfer to the semiconductor/electrolyte interface, which reduces photocorrosion and surface recombination (21, 25, 134, 135). Previous studies have shown that amorphous leaky titanium dioxide (TiO_2) film grown by atomic layer deposition (ALD) protects photoelectrodes (e.g. photocathode and photoanode) because it provides favourable surface energy band bending, allowing for the transfer of electrons to the electrolyte (10, 14, 20, 22, 29, 136-138). Therefore, in this study, a 10 nm amorphous TiO_2 thin film was deposited by ALD onto the Si/GaP photocathode surface and a p-type single-crystalline GaP reference photocathode, respectively. The TiO_2 layer was used as a protective layer to prevent photocorrosion of the GaP absorber during the PEC test. In addition, Pt was deposited onto the surface of both GaP photocathodes as an efficient catalyst for the hydrogen evolution reaction (HER) to enhance PEC hydrogen production, as shown in Figure 3.6. The cross-sectional scanning (STEM) images show a well-defined amorphous TiO_2 layer deposited onto the GaP surface, as shown in Figure 3.6.

The GaP photocathodes were analysed by energy dispersive X-ray spectroscopy (EDS) mapping to further probe the interface structure and showed a clear difference in topology between as-deposited TiO_2 and Pt on the surface of GaP, as shown in Figure 3.6 and 3.7. The STEM and EDS measurements also confirmed a 10 nm thick Pt co-catalyst layer deposited by sputtering onto the TiO_2 protection layers of the GaP grown on the Si photocathode and the GaP reference photocathode. The two photocathodes are denoted as Si/GaP-TiO_2-Pt and GaP-TiO_2-Pt.

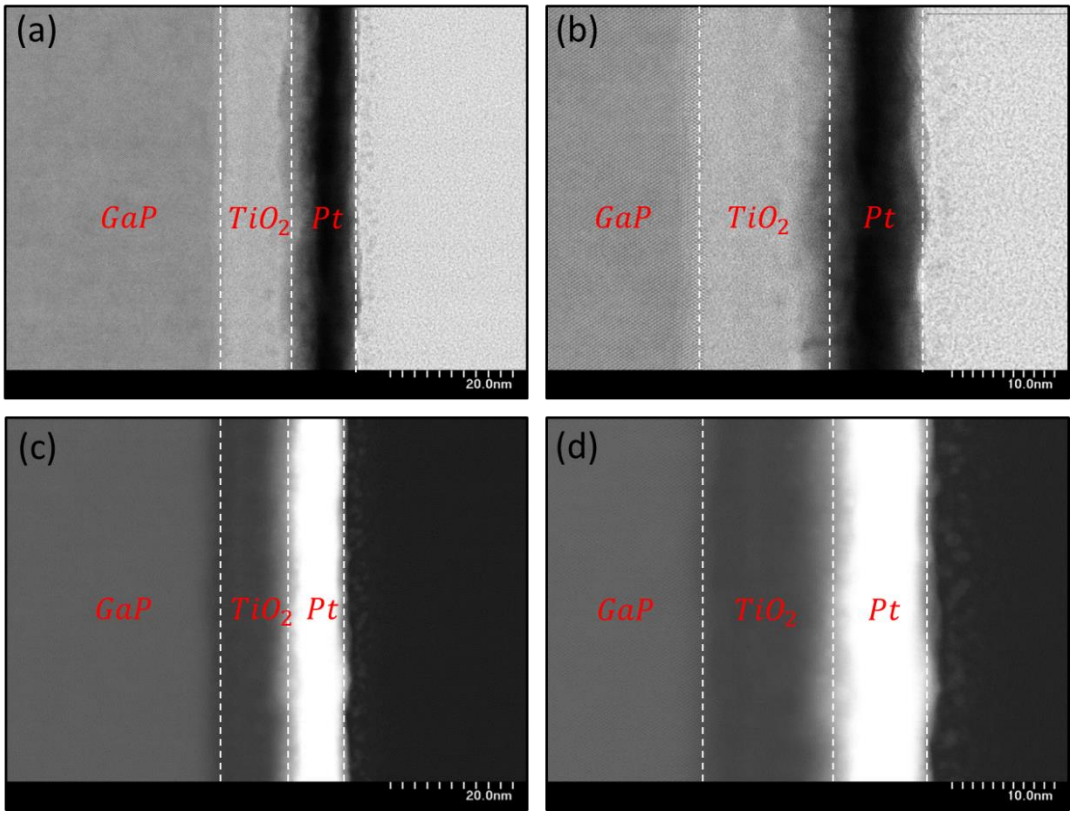

Figure 3.6. Characterization of GaP surface modified with TiO_2 and Pt using STEM. **(a-b)** Cross-sectional high-angle annular dark-field (HAADF) image of the GaP-TiO_2-Pt. **(c-d)** Cross-sectional high-angle annular bright-field (ABF) image of the GaP-TiO_2-Pt.

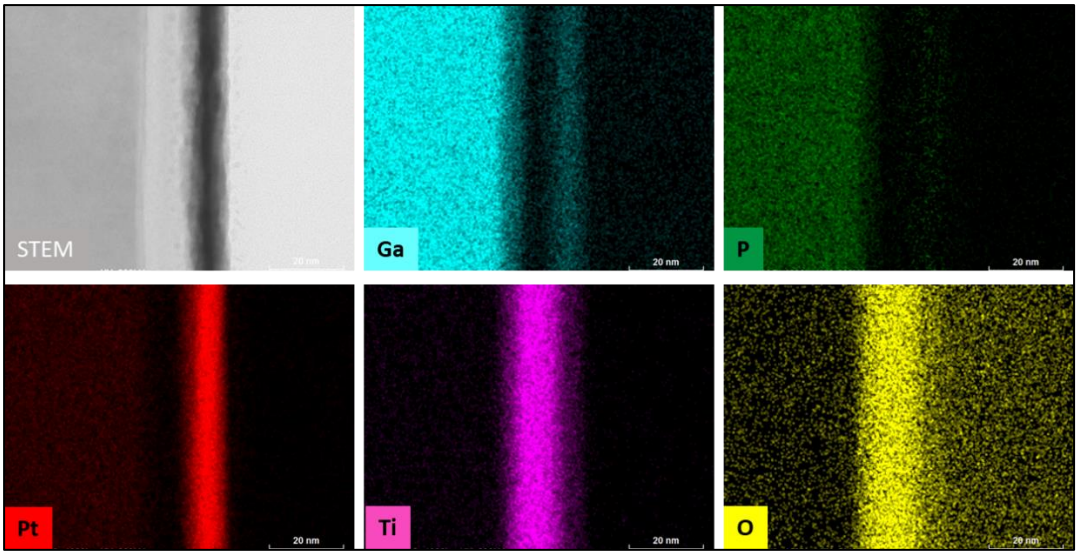

Figure 3.7. Structural chemical profiling of the Si/GaP-TiO_2-Pt photocathode. Energy dispersive X-ray spectroscopy (EDS) mapping shows the individual layer thickness associated with the Ti, O, Ga, P, and Pt elements.

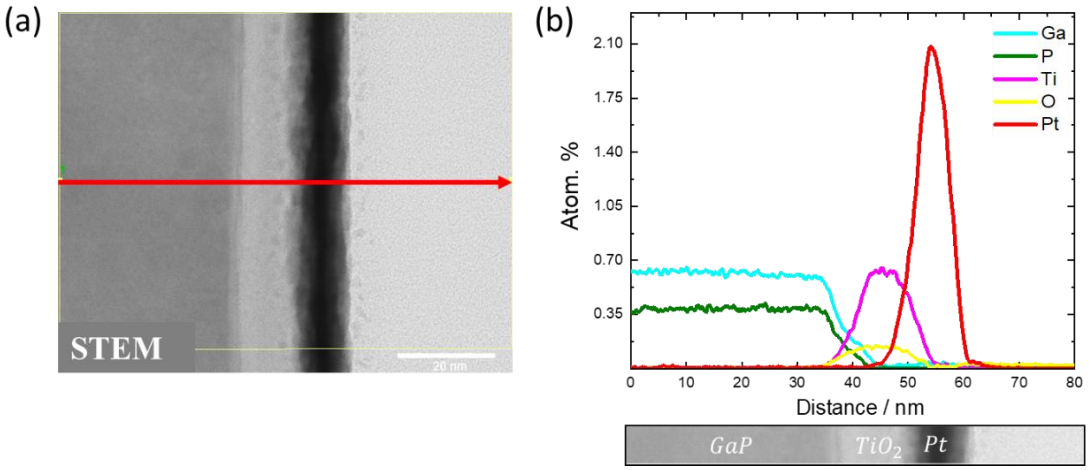

Figure 3.8. STEM EDS line profiling coupled with spectral component matching showing the individual layer thickness for TiO_x and Pt. The Y-axis denotes un-calibrated element intensity. Note that there is some inter-diffusion in the GaP/TiO_x interface and TiO_x/Pt interface. The inset is the STEM image where the EDS line profiling was taken.

3.3.4. Structural Modification of GaP with MoS_2 Co-catalyst

The structural properties of the MoS_2-modified surface of the GaP photocathode grown on a Si substrate were analysed using cross-sectional high-angle annular dark-field (HAADF) and annular bright field (ABF) imaging, as shown in Figure 3.9(a-d). The cross-sectional STEM images of the GaP-TiO_2-MoS_2 interfaces show well-defined junctions between the layers. However, the STEM-based energy-dispersive X-ray spectroscopy (EDS) line profiling shows the individual layers are also well resolved from the EDS mapping in Figure 3.10 and 3.11, indicating good layer compactness and little intermixing at the interface. Compared with the Pt layer, the MoS_2 is not as dense but thicker with a larger surface area. The MoS_2 layer was about 20 nm thick and consisted of needle-like features protruding from the flat and uniform TiO_2 layer. As shown in Figure 3.9, the corresponding EDS mapping and line-profiling graph also provides quantitative evidence for the composition of the individual layers as well as their thickness (20 nm MoS_2 and 10 nm TiO_2).

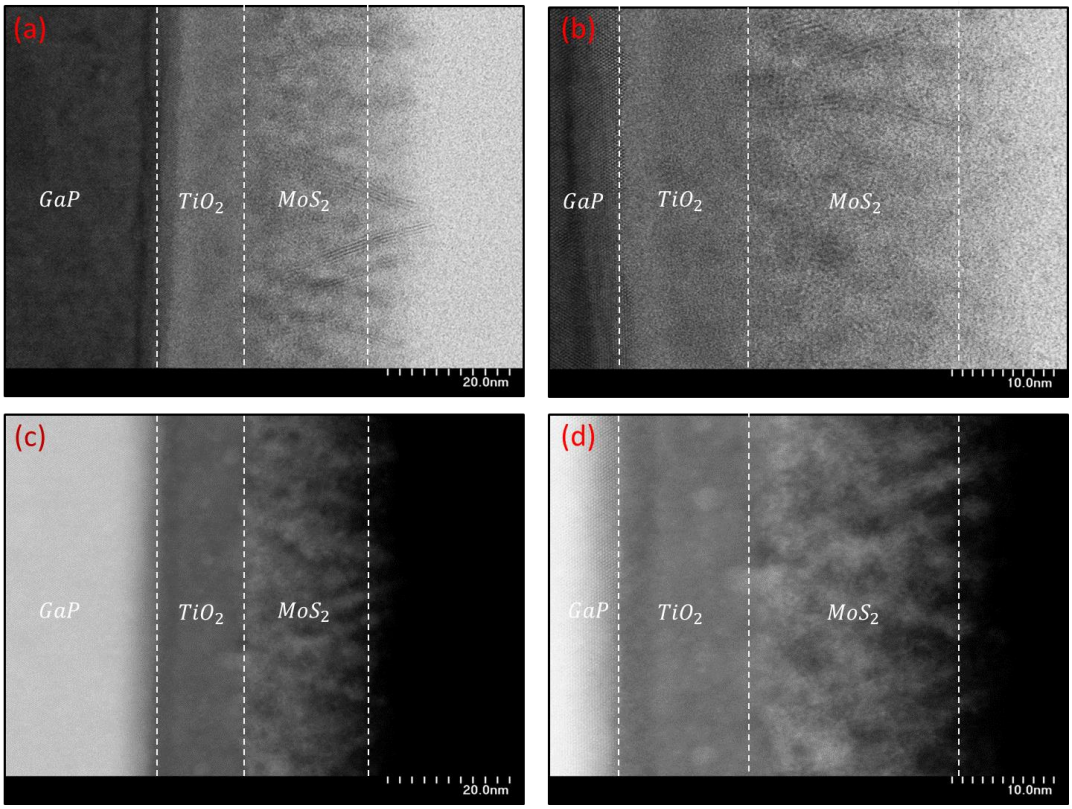

Figure 3.9. Structural characterization of GaP photocathode modified with TiO_2 and MoS_2. **(a-b)** Cross-sectional high-angle annular dark-field (HAADF) image of the Si/GaP-TiO_2-MoS_2 photocathode. **(c-d)** Cross-sectional high-angle annular bright-field (ABF) image of the Si/GaP-TiO_2-MoS_2 photocathode.

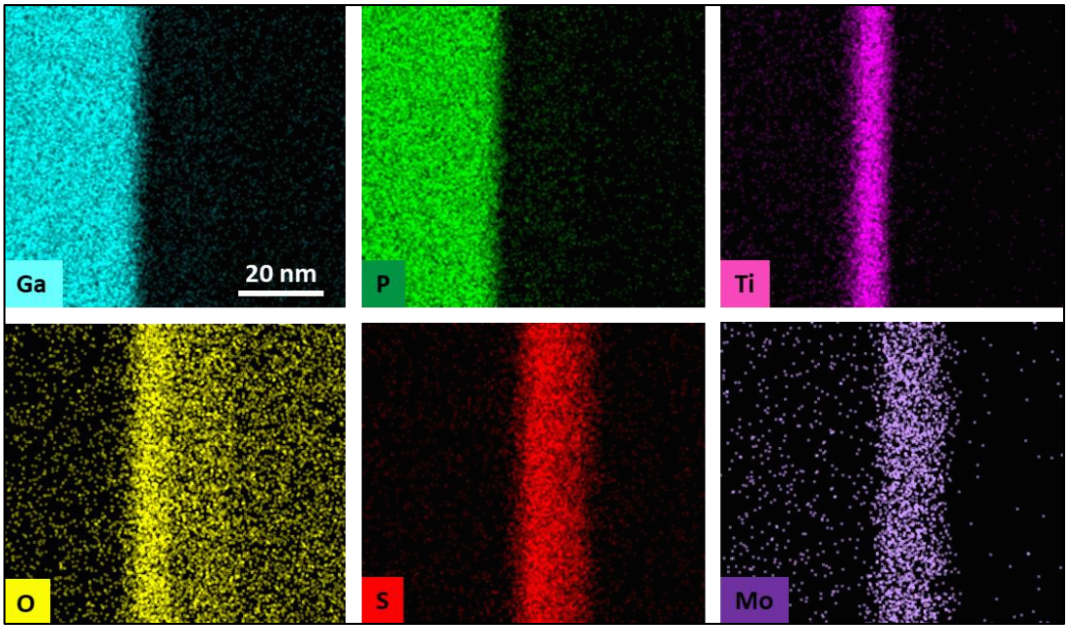

Figure 3.10. Structural chemical profiling of the Si/GaP-TiO_2-MoS_2 photocathode. Energy dispersive X-ray spectroscopy (EDS) mapping shows the individual layer thickness associated with the Ti, O, Ga, P, S, and Mo elements.

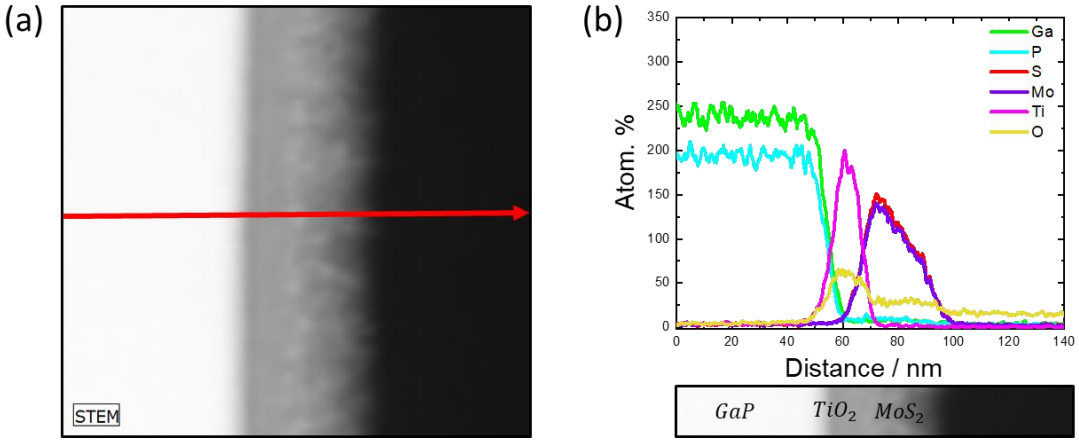

Figure 3.11. STEM EDS line profiling coupled with spectral component matching showing the individual layer thickness for TiO_x and MoS_2. The Y-axis denotes un-calibrated element intensity. Note that there is some inter-diffusion in the GaP/TiO_x interface and TiO_x/MoS_2 interface. The inset is the STEM image where the EDS line profiling was taken.

3.3.5. Photoelectrochemical Performance of the GaP Photocathodes

A schematic illustration of the GaP photocathodes modified by amorphous TiO_2 and MoS_2 is shown in Figure 3.12. The photocurrent density (J) versus potential (V) for the GaP photocathodes is shown in Figure. 3.13(a). Under one-sun AM 1.5G illumination, the Si/GaP-TiO_2-Pt photocathode showed a saturated photocurrent density of 0.96 (mA/cm^2) at -0.80 V versus the reversible hydrogen electrode (RHE) and an onset potential at approximately 0.477 V versus RHE. In comparison, the GaP-TiO_2-Pt reference photocathode showed a saturated photocurrent of 1.74 (mA/cm^2) at -0.80 V versus RHE with an onset potential at 0.487 V versus RHE. The incident photon-to-current conversion efficiency (IPCE) was evaluated for the GaP photocathodes at -0.80 V versus RHE, as shown in Figure 3.13(b). The IPCE values of the Si/GaP-TiO_2-Pt and GaP-TiO_2-Pt photocathodes are 18.3% and 36.2% at 400 nm, respectively. The reduced IPCE for the Si/GaP-TiO_2-Pt photocathode is due to a lower electron diffusion length in the GaP film on Si, which is in good agreement with the *J–V* measurements. In the range 450–500 nm, the IPCE of both photocathodes drops sharply due to the weak absorption in indirect-bandgap GaP (~ 2.26 eV). The slightly reduced onset potential of the Si/GaP-TiO_2-Pt photocathode compared to that of the GaP reference photocathode is attributed to the observable crystal defects such as threading dislocations. Nonetheless, the penalty paid to reduce the cost is minor; the reduction in onset potential is only 10 mV and the photocurrent density remains about 55.2% of that of the photocathode reference. Further optimization of growth conditions, e.g. using dislocation filter layers, may lead to further reduction of defects and improvements to the photocathode performance.

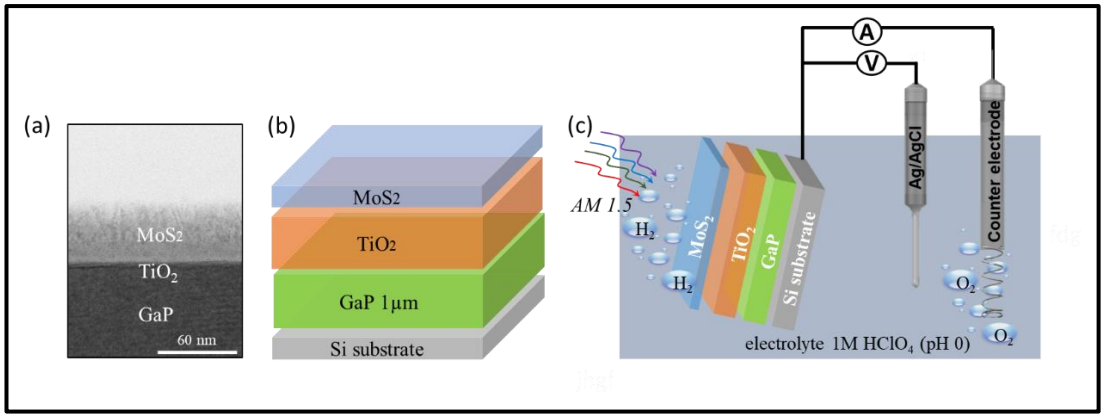

Figure 3.12. Surface modification and structural characterization of GaP photocathodes. **(a)** Cross-sectional STEM image of the GaP photocathode modified by MoS_2 and TiO_2 nanostructure. **(b)** Schematics of the growth of the GaP photocathode modified by MoS_2 and TiO_2 nanostructure. **(c)** Schematic diagram of the experimental setup used for the photoelectrochemical measurements, which consists of the working electrode (GaP), reference electrode (Ag/AgCI), and counter electrode (platinum mesh) in 1.0 M $HClO_4$ pH zero.

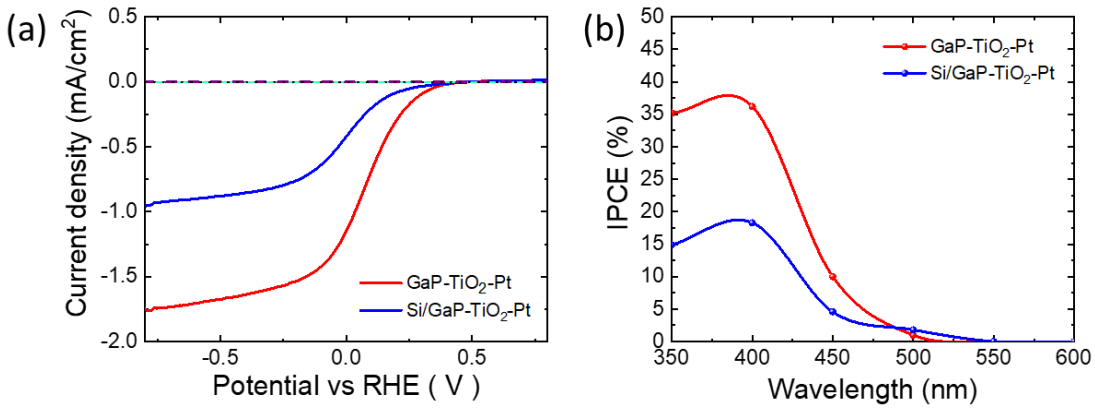

Figure 3.13. Photoelectrochemical measurements for GaP photocathodes. **(a)** Photocurrent density–potential (*J*–*V*) curves (scan rate is 50 mV s^{-1}) of GaP-TiO_2-Pt (red line) and Si/GaP-TiO_2-Pt (blue line) photocathodes in 1 M $HClO_4$ under one-sun illumination. **(b)** Incident photon-to-current conversion efficiency (IPCE) of GaP-TiO_2-Pt (red line) and Si/GaP-TiO_2-Pt (blue line) photocathodes in 1 M $HClO_4$ at -0.8 V versus RHE.

On the other hand, earth-abundant catalysts such as molybdenum sulphide (MoS_2) are promising alternatives to precious metals such as platinum, ruthenium, and iridium. Moreover, MoS_2 showed high activity with regard to hydrogen evolution reactions under strongly acidic conditions (21, 24, 25, 66, 103, 139-141). Therefore, to demonstrate the potential for further cost reduction, TiO_2 and MoS_2 thin layers were deposited by ALD onto the Si/GaP photocathode and single-crystalline GaP reference photocathode as the surface protection layer and co-catalyst layer, respectively, as described in the Methods section. The two new photocathodes based on the Si/GaP and single-crystalline GaP reference photocathodes are denoted as Si/GaP-TiO_2-MoS_2 and GaP-TiO_2-MoS_2, respectively. As shown in Figure 3.14(a), the Si/GaP-TiO_2-MoS_2 photocathode exhibited a photocurrent onset potential of 0.46 V versus RHE and a saturated photocurrent density of 0.95 mA cm^{-2}. In contrast, the MoS_2-modified GaP reference photocathode had an onset potential of about 0.657 V versus RHE and a saturated photocurrent density of 1.53 mA cm^{-2}. To further investigate the wavelength-dependent PEC contribution of GaP on silicon to the photocurrent, the incident-photon-to-current conversion efficiency (IPCE) was measured. As shown in Figure 3.14(b), the IPCE at 400 nm was 34.1% for the GaP-TiO_2-MoS_2 photoelectrode and 23.8% for the Si/GaP-TiO_2-MoS_2 photoelectrode. The IPCE of all photocathodes decreased towards longer wavelengths (> 550 nm). Again, by using the MoS_2 co-catalyst instead of the Pt co-catalyst, the performance of the GaP photocathode grown on Si substrate is still remarkable, with a comparable onset potential photocurrent density to the state-of-the-art GaP photocathodes (14, 127, 128, 142). More importantly, GaP photocathodes grown on Si substrates with low-cost co-catalysts appear to be a promising approach in the move towards cost-effective hydrogen generation.

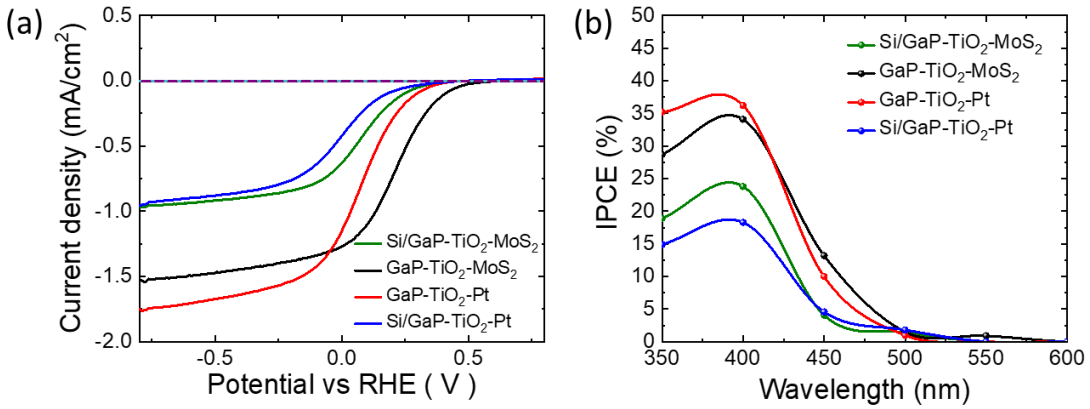

Figure 3.14. Photoelectrochemical performance of GaP photocathodes. **(a).** Photocurrent density–potential (*J*–*V*) curves (scan rate is 50 mV s^{-1}) of GaP-TiO_2-Pt (red line), Si/GaP-TiO_2-Pt (blue line), Si/GaP-TiO_2-MoS_2 (green line), and GaP-TiO_2-MoS_2 (black line) photocathodes in 1 M $HClO_4$ under one-sun illumination. **(b).** Incident photon-to-current conversion efficiency (IPCE) of GaP-TiO_2-Pt (red line), Si/GaP-TiO_2-Pt (blue line), Si/GaP-TiO_2-MoS_2 (green line), and GaP-TiO_2-MoS_2 (black line) photocathodes in 1 M $HClO_4$ at -0.8 V versus RHE.

3.3.6. Hydrogen Gas Production of the GaP Photocathode

To gain further insight into the PEC performance of the Si/GaP-TiO_2-MoS_2 photocathode, the hydrogen production of both photocathodes was measured over 100 min by chronoamperometry under illumination in a gas-tight photoelectrode cell using a Clark electrode sensor. As shown in Figure 3.15(a), the Si/GaP-TiO_2-MoS_2 photocathode reached a calculated Faradaic efficiency (FE) of 73.4±20.2% after a ~25 min induction period. Figure 3.15(b) shows that the GaP-TiO_2-Pt photocathode reached a FE of 105.4±8.7% after a much longer induction period of 90 min. Part of the initially lower FE might be due to a delay in the equilibration of the H_2 concentration in solution and gas phases. Note that the Clark sensor was positioned in the gas phase. Another delay might have been caused by the activation time of the catalyst layers. The measurements were set at a constant potential, and the 'noisy' photocurrent and H_2 production in Figure 3.14(a-b) originate from accumulation of

gas bubbles at the photocathode surface and sequentially sudden release of gas bubbles.

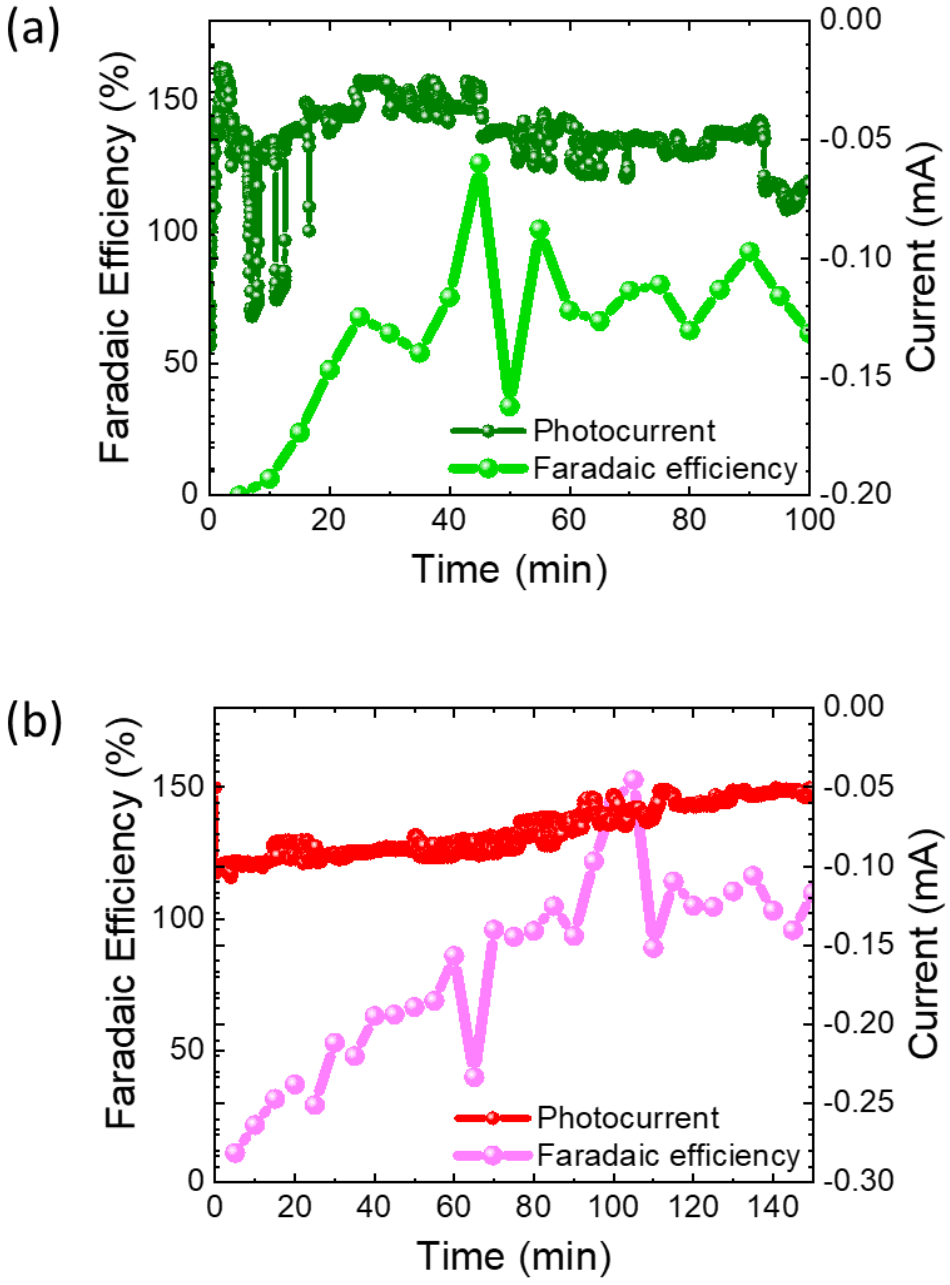

Figure 3.15. Faradaic efficiency of H_2 production measured with a Clark H_2 sensor in a gas-tight three-electrode photoelectrochemical cell under illumination and constant potential. **(a)** FE of the Si/GaP-TiO_2-MoS_2 photoelectrode held at -0.39 V versus RHE. **(b)** FE of the GaP-TiO_2-Pt photoelectrode held at -0.09 V versus RHE.

3.3.7. Stability Assessment of the GaP Photocathodes Grown on Silicon

The short-term and long-term stability of the GaP photocathodes was evaluated for hydrogen evolution under one-sun AM1.5 simulated solar illumination, as shown in Figure 3.16(a-b). These electrodes were configured with a constant potential controlled at 0 V versus RHE in $HClO_4$ (pH 0) electrolyte. As shown in Figure 3.16(a), for the initial stability of the electrodes evaluated, all the photocathodes exhibited rather good stability of photocurrents over the first 30 min (Figure 3.16(a)). However, for the GaP photocathodes with Pt co-catalysts, both the Si/GaP-TiO_2-Pt and GaP-TiO_2-Pt photoelectrode already exhibited some photocurrent decay, which may be attributed to removal of the Pt catalyst from the surface. The long-term stability of all photocathodes was measured at 0 V versus RHE for 3 h, as shown in Figure 3.16(b). The photocurrent density of the Si/GaP-TiO_2-MoS_2 photocathode was stable at -0.89 mA cm^{-2} for 3 hours under continuous simulated solar light illumination, which is attributed to the high-activity MoS_2 for hydrogen evolution reaction in strong acidic conditions. On the contrary, the photocurrent density for Pt-modified GaP photocathodes, both Si/GaP-TiO_2-Pt and GaP-TiO_2-Pt, gradually dropped from 1.4 mA cm^{-2} to 0.8 mA cm^{-2} and from 0.6 mA cm^{-2} to 0.48 mA/cm^2, respectively, which is attributed to the failure of the TiO_2 protection layer and significant photocorrosion of the electrode due to possible removal of Pt catalysts from the surface.

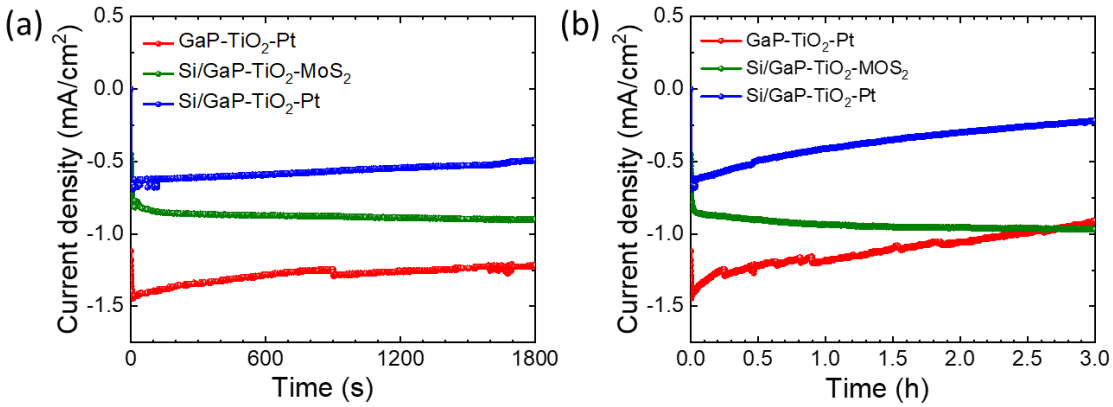

Figure 3.16. Stability test for GaP photocathodes. **(a)** Photoelectrochemical short-term stability measurements of various GaP photocathodes in 30 min photocurrent density–time (J–t) plots held at 0 V versus RHE in 1 M $HClO_4$ under one-sun illumination. **(b)** Photoelectrochemical long-term stability measurements of a various GaP photocathodes for 3 h held at 0 V versus RHE in 1 M $HClO_4$ under one-sun AM1.5 simulated solar illumination.

To compare the degree of photocorrosion of the two GaP photocathodes grown on Si substrates, the surface morphology was studied using SEM, as shown in Figure 3.17(a-d). The SEM images of the surfaces of the MoS_2-modified GaP and Pt-modified GaP photocathodes show a distinct difference in morphology after the stability test. Both photocathodes show some pits on the surface indicating photocorrosion; however, the MoS_2-modified surface shows fewer surface pits compare to the Pt-modified surface. The pits also appear to be more elongated and deeper on the Pt-modified GaP surface, suggesting severe photocorrosion, as shown in Figure 3.17(c-d).

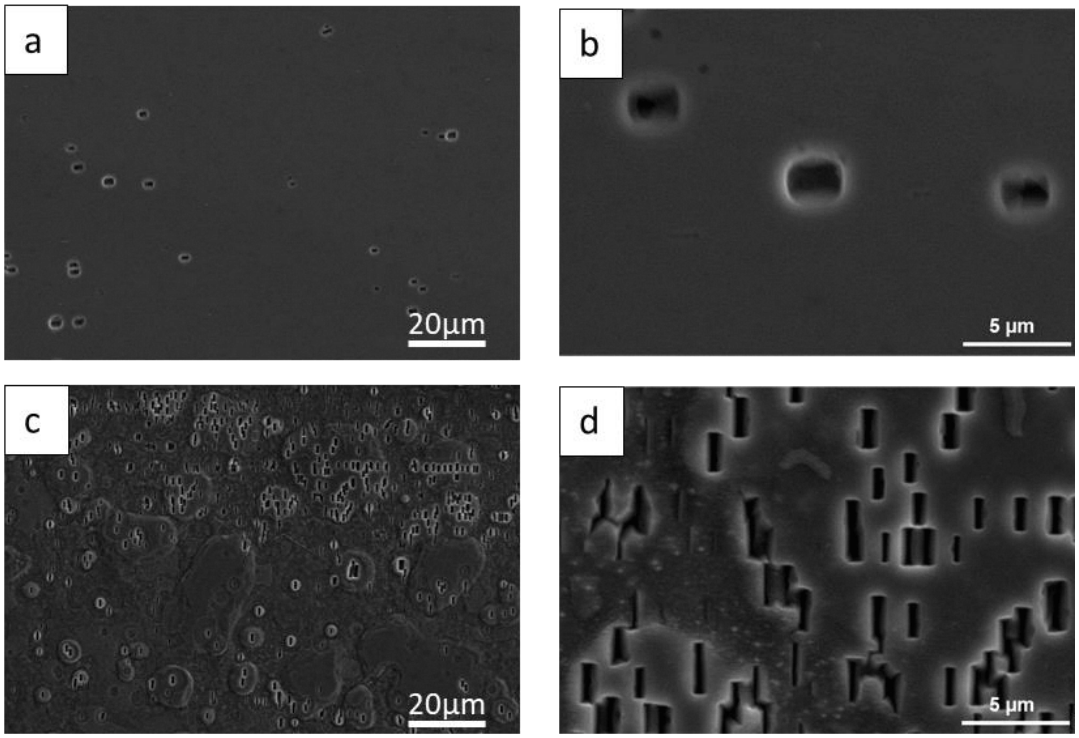

Figure 3.17. Scanning electron microscopy (SEM) images of the photoelectrodes after the reliability test (3 h). **(a-b)** SEM image for the surface of the GaP/Si-TiO_2-MoS_2 photoelectrode after a 3 h stability test. **(c-d)** SEM image for the surface of the GaP/Si-TiO_2-Pt electrode after a 3 h stability test.

Atomic force microscopy (AFM) is an excellent technique for assessing the surface morphology. AFM images of both photocathodes after 3 h stability testing are shown in Figure 3.18(a-d). As shown in Figure 3.18, the surface roughness of the Pt-modified electrode is significantly worse than that of the MoS_2-modified electrode. The Z-scales of the AFM images are 30 nm and 800 nm, respectively, and the RMS roughness of the Pt-modified GaP electrode measured over a 20 µm × 20 µm area is over one order of magnitude higher than that of the MoS_2-modified electrode, as shown in Figure 3.18(c-f). Additionally, the pit depth on the MoS_2-modified electrode is only about 30 nm while it can be over 500 nm on the Pt-modified GaP surface, confirming a distinct improvement in stability using the MoS_2 co-catalysts.

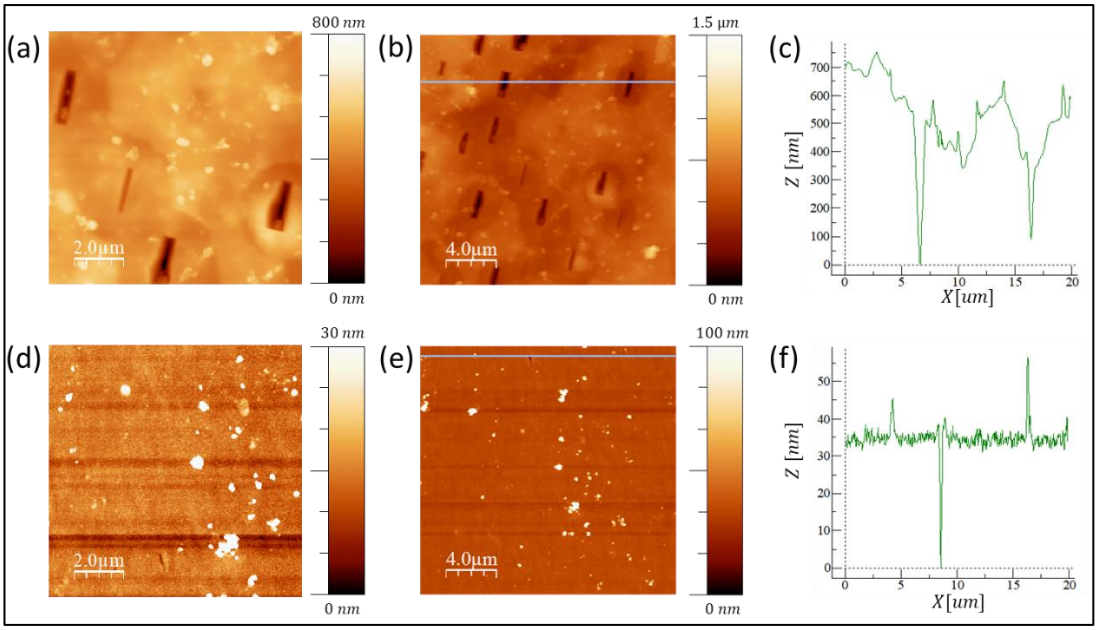

Figure 3.18. Surface morphology of GaP photocathodes after PEC test. (**a)** AFM surface morphology of Si/GaP-TiO_2-Pt. **(b)** 20 µm × 20 µm AFM surface morphology of Si/GaP-TiO_2-Pt after reliability test (> 3h). AFM line profile of the photoelectrode surfaces after reliability test. **(c)** The RMS roughness of Si/GaP-TiO_2-Pt measured from (b) is 97.2 nm. The depth of the etching pits on the Si/GaP-TiO_2-Pt photocathode is about 500 nm. **(d)** AFM surface morphology of Si/GaP-TiO_2-MoS_2. **(e)** 20 µm × 20 µm AFM surface morphology of Si/GaP-TiO_2-MoS_2. **(f)** The RMS roughness of Si/GaP-TiO_2-MoS_2 from (e) is 7.8 nm and the depth of the etching pits on the Si/GaP-TiO_2-MoS_2 surface is 30 nm.

X-ray photoelectron spectroscopy (XPS) was performed to determine the surface composition and chemical state of the Si/GaP photocathodes, as shown in Figure 3.19 and 3.20. Before PEC testing of the Si/GaP-TiO_2-MoS_2 photocathode as shown in Figure 3.19(a-d), only peaks for Mo, S, and O were seen as expected due to the MoS_2 overlayer (Figure 3.19). The deconvolution of the Mo 3d peaks produced two sets of doublets, with the primary Mo $3d_{5/2}$ peak centred at 229.0 eV and corresponding to Mo^{4+} associated with MoS_2. The secondary $3d_{5/2}$ peak was centred at 230.9 eV and belongs to Mo^{4+}, and is ascribed to surface oxidation. The S 2p region showed an overlapping doublet separated by 1.16 eV with the $2p_{3/2}$ peak at 162.1 eV corresponding to MoS_2. After PEC analysis, MoS_2 still remained on the surface. Similar to the spectra before PEC testing, Mo $3d_{5/2}$ peaks were observed at 228.7 eV (Mo^{4+}, Mo-S) and 230.0 eV (Mo^{4+}, Mo-O) with an S $2p_{3/2}$ peak observed at 161.7 eV (S^{2-}, S-Mo). Due to the robust nature of the MoS_2 layer, no signals were observed for Ti, Ga, and P.

The surface composition and chemical state of the Si/GaP-TiO_2-Pt photocathode are shown in Figure 3.20(a-d). Before the PEC test, peaks were only observed for Pt 4f with no signals being seen for Ti, O, Ga, and P. This is expected due to the dense nature of the Pt surface layer. The Pt 4f doublet was deconvoluted using an asymmetric line shape to give the Pt $4f_{7/2}$ peak centre at 71.0 eV corresponding to metallic Pt. After the PEC test, no Pt peaks were seen, suggesting complete degradation of the metallic layer in the acidic solution. Surprisingly, no Ti was observed, suggesting that the TiO_2 layer was also degraded. An oxygen signal was observed, but this is thought to be due to the surface oxidation of Ga in the GaP. The Ga $2p_{3/2}$ peak was centred at 1117.7 eV corresponding to Ga in the 3+ oxidation state. For P 2p, two sets of doublets were observed, with one $2p_{3/2}$ at 129.0 eV that belongs to P in the 3- oxidation state bound

to Ga while a smaller transition at 133.1 eV corresponds to the 5+ oxidation state that belongs to the metal phosphate form. In the end, the surface or composition of the MoS_2-modified GaP photocathode grown on Si substrate did not change after electrolyte testing, as shown by the SEM and XPS measurements.

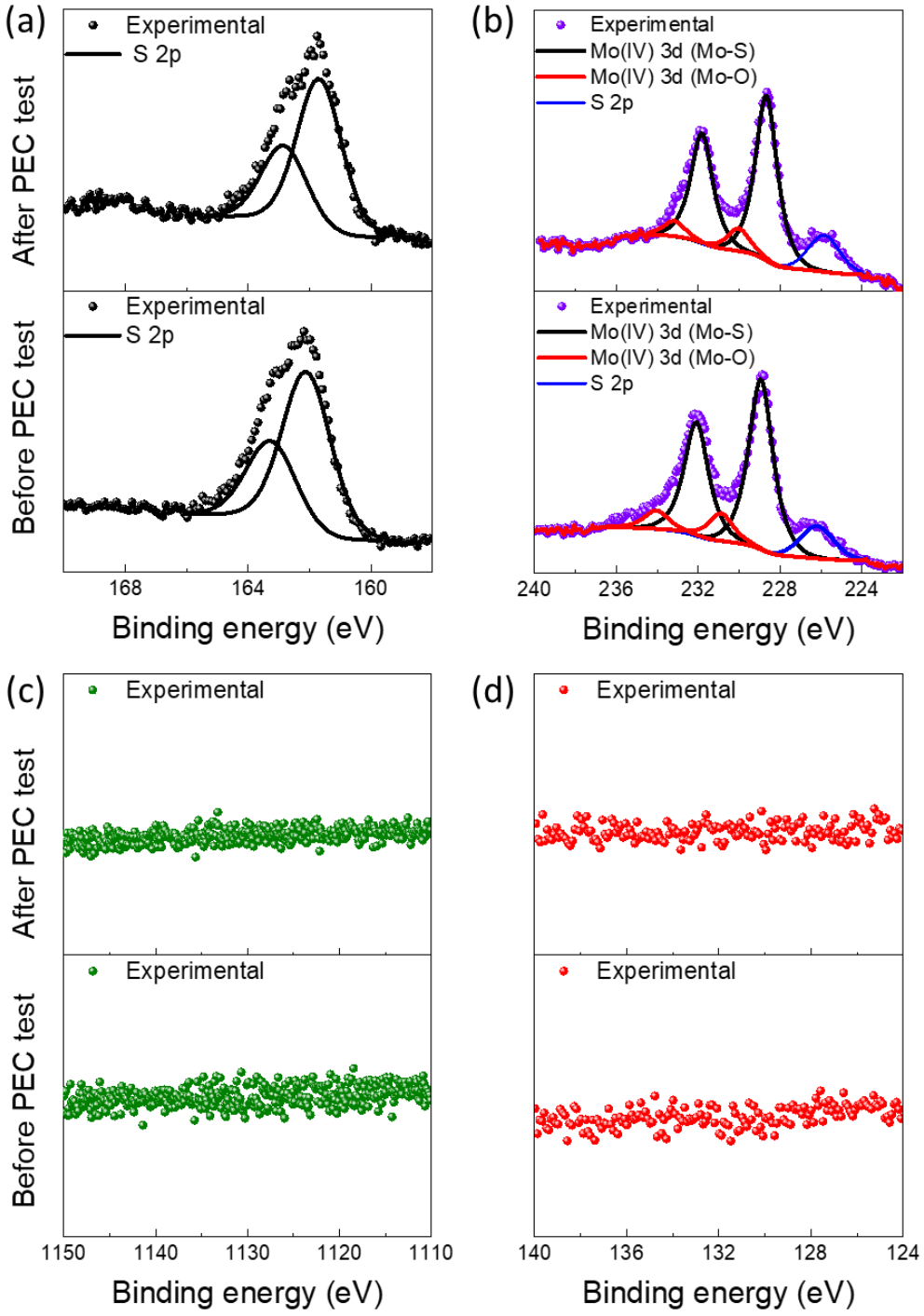

Figure 3.19. XPS measurements of GaP-TiO_2-MoS_2 grown on silicon substrate before and after PEC test. (a-d). XPS measurements of the Si/GaP-TiO_2-MoS_2 photocathode before (bottom column) and after (top column) the photoelectrochemical stability measurement. Before testing, the structure contained Mo 3d and 2p corresponding to MoS_2. There was no presence of Ga or P peaks before testing. After testing, the composition and chemical state remain very similar. There is still no presence of Ga and P peaks after testing, as shown in **(c)** and **(d)**.

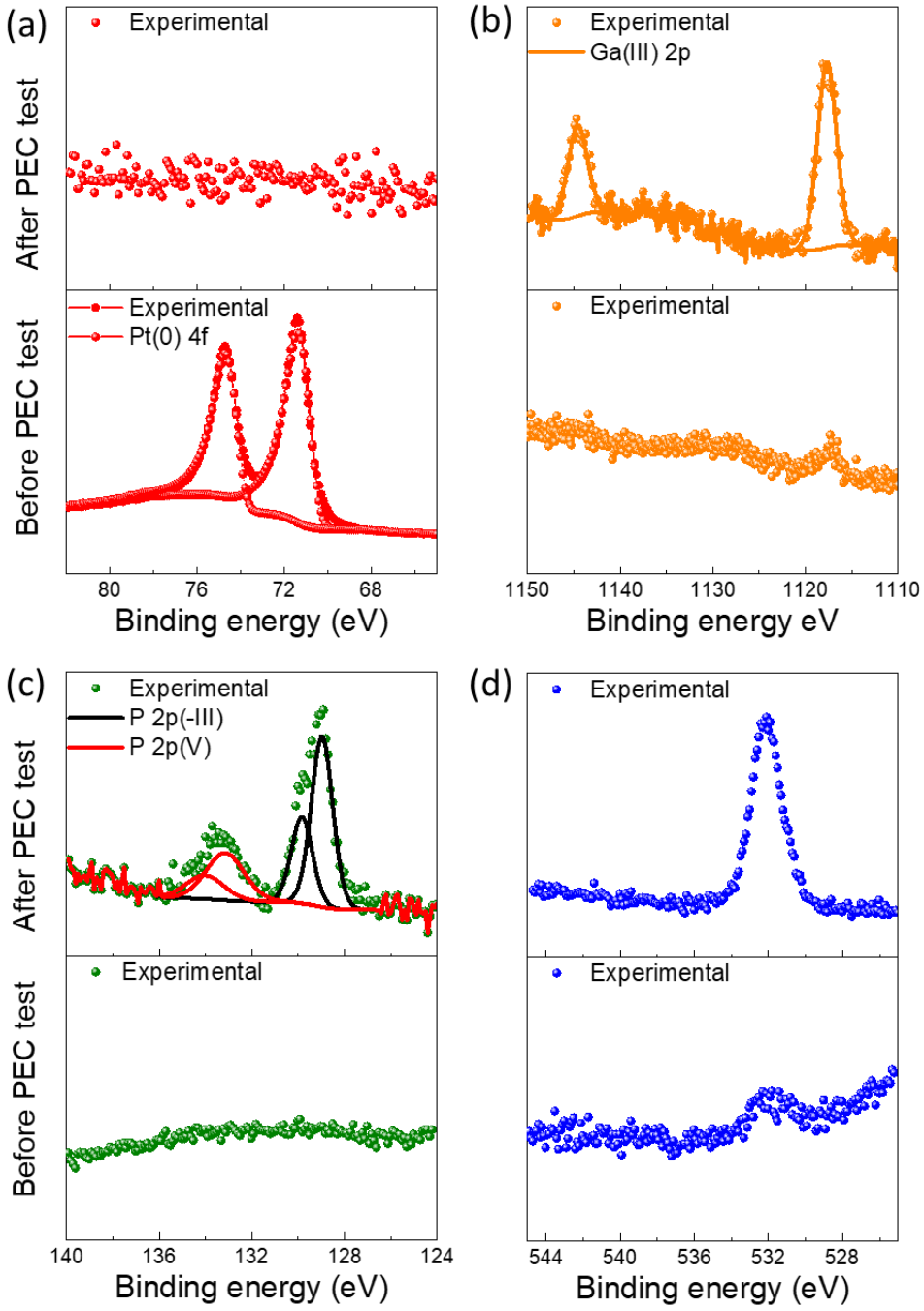

Figure 3.20. XPS measurements of GaP-TiO_2-Pt grown on silicon substrate before and after PEC test. (a-d). XPS measurements of the Si/GaP-TiO_2-Pt photocathode before (bottom column) and after (top column) the photoelectrochemical stability measurement. Before testing, the surface contained Pt 4f, corresponding to Pt. There was no presence of Ga and P peaks before testing. After testing, the Pt peak is no longer present, and this indicates the complete removal of the Pt catalyst. Ga and P peaks clearly appear after testing, as shown in **(c)** and **(d)**. A peak corresponding to O

1s also becomes more dominant but no Ti peak remains observable after testing, confirming the removal of the Pt catalyst layer and TiO_2 protection layer.

3.4 Conclusions

In conclusion, in this chapter the formation of a hetero-integration of a high-quality GaP thin film on a silicon substrate by MBE has been demonstrated. Despite some performance penalty, the GaP-on-Si photocathode, along with an earth-abundant MoS_2 co-catalyst, shows great promise in reducing the cost of photocathodes based on GaP for hydrogen production. Additionally, the TiO_2 and MoS_2 layers, greatly improved the chemical stability of the GaP photocathode and increased the stability of the photocathode up to 3 h under continuous simulated solar light illumination at $HClO_4$ (pH=0), exceeding that of the Pt-modified GaP photocathode. The high-stability and cost-effective GaP photocathode grown on a silicon substrate without the use of noble metal HER catalysts are promising for low-cost, high efficiency, and stable PEC water splitting devices. The present work represents the initial development of the GaP photocathode on a silicon substrate with many promising paths to future improvements. The next chapter describes the addition of antimony (Sb) into GaP grown on a silicon substrate by MBE. Since between the two materials there are some of the desired qualities of a photoelectrode, a mixed alloy might have the right combination of properties to enable water photoelectrolysis.

Chapter 4: $GaP_{1-x}Sb_x$ with a Direct Band Gap of 1.65 eV for Full-spectrum Solar Energy Harvesting

The previous experimental chapter revealed a GaP photocathode grown on a low-cost silicon substrate for PEC water splitting. This chapter will explore a new n-type III-V semiconductor material $GaP_{1-x}Sb_x$ that provides one of the cheapest and most desirable routes for solar fuel application. $GaP_{1-x}Sb_x$ has a widely tunable band gap from 0.726 eV to 2.26 eV and an indirect to direct band gap crossover composition of X= 0.33. The addition of Sb into GaP provides three advantages: (i) direct bandgap transitions; (ii) absorption spectral range extension to the entire solar spectrum (visible range); and (iii) better band alignments between the semiconductor and the water redox potentials, which leads to a high photocurrent and STH efficiency. The growth of $GaP_{0.67}Sb_{0.33}$ epitaxially integrated on Si with a direct band gap of 1.65 eV will be described in this chapter. The $GaP_{1-x}Sb_x$ samples grown by MBE, photoluminescence (PL), ellipsometry, and tight-binding model were performed by collaboration with Prof. Charles at University of Rennes, INSA Rennes, CNRS, Institut FOTON–Rennes.

4.1. Introduction

The combustion of fossil fuels such as coal and oil are recognized as one of the major sources of climate change due to the emission of greenhouse gases such as carbon dioxide. Due to the impact of global warming on society, there is an urgent need to find alternative energy sources that are clean, renewable, and abundant (31, 36, 41, 143). In this regard, the photoelectrochemical (PEC) splitting of water into oxygen and hydrogen using solar radiation is considered as a promising technology (19, 26, 116, 144). To fulfil the sustainable energy objective, PEC systems need to be cost-effective, stable in strongly alkaline or acidic electrolytes, and harvest a large portion

of the solar spectrum. Despite the emerging high solar-to-hydrogen (STH) conversion efficiency of monolithic photovoltaic-biased PEC cells and multiple absorbers, the complexity of their fabrication and prohibitive cost hinder their use in large-scale applications (65, 104-107, 145).

For metal oxides, large band gaps (usually larger than 2 eV) limit solar light absorption, which typically leads to a lower STH conversion efficiency (1-3, 5, 146-149). In that case, using a single photoelectrode, i.e. one absorber photoelectrode, with a direct band gap (ideally 1.6 eV) provides a desirable and potentially low-cost approach due to a balanced combination of simplicity in fabrication and efficient photon harvesting for PEC water splitting. For example, a single semiconductor with a band gap of 1.6 eV can yield a maximum STH efficiency of 30% under one-sun illumination (19). However, due to the relatively high overpotential and the requirement of four holes per oxygen molecule, the water oxidation process presents a bottleneck for the realization of efficient and practical water splitting systems (21, 137). Therefore, the development of high-performance PEC water splitting systems has been hindered due to the lack of an ideal photoanode material that has a sufficiently narrow bandgap and is stable under strongly alkaline or acidic conditions.

On the other hand, it has been recently found that the band edges of III-V semiconductor materials are particularly adjustable such that the band gap of GaP can be tuned from 2.26 to 0.72 eV with the incorporation of Sb and is an ideal candidate photoelectrode for PEC water oxidation (91, 150). More importantly, $GaP_{1-x}Sb_x$ with a band gap of 1.6 to 2.3 eV is a promising top absorber on a Si (1.1 eV) bottom absorber, and may pave the way for the ideal tandem PEC systems corresponding to a theoretical STH efficiency of 27% (11). For instance, Sunkara et al. have demonstrated

that GaP with a 3% incorporation of antimony has a direct band gap of 2.68 eV that enhances the absorption spectrum but leads to relatively low photocurrent density due to the large band gap (151). However, it is commonly known that growing a high-quality GaP structure with a high Sb content on a silicon substrate is challenging, due to the large lattice mismatch. Furthermore, the stability of III-V semiconductor photoanodes for water oxidation is a critical challenge when operated in contact with aqueous solutions (11, 13, 24).

Protective layers and catalysts can stabilize the photoanodes by reducing the kinetic overpotential and prevent the accumulation of holes on surface of the semiconductor photoelectrodes in strongly alkaline solution (152). Titanium dioxide (TiO_2) is one of the best layers to protect the surfaces of III-V materials from photocorrosion (17, 138). The strategy uses either an ultra-thin layer to allow the charge transfer via tunnelling (137) or a "leaky" defect-state formed in a thicker TiO_2 layer (10, 153) due to the high intrinsic chemical stability (21). A metallic oxygen evolution reaction (OER) catalyst, such as Ni, is an earth-abundant catalyst that enhances efficient water oxidation in a strongly alkaline solution (8, 10, 21, 23, 32, 135, 152).

For the first time, the fabricated $GaP_{1-x}Sb_x$ on a silicon substrate by molecular beam epitaxy (MBE) with a high concentration of Sb (X = 0.33) has been demonstrated that allows the band gap to be reduced to a direct bandgap of 1.65 eV. By using an atomic-layer deposition (ALD) grown-TiO_2 (20 nm) as a protection layer and Ni (8 nm) as an oxygen evolution co-catalyst, the $GaP_{0.67}Sb_{0.33}$ photoanode exhibited a high photocurrent of 4.82 mA/cm^2 at 1.23 V and an onset potential of 0.35 V versus a reversible hydrogen electrode (RHE) in 1.0 M KOH (pH 14) electrolyte under one-sun illumination. The narrow bandgap of the $GaP_{0.67}Sb_{0.33}$ photoanode led to an

incident-photon-to-current efficiency (IPCE) value of 67.1% between wavelengths 400 nm to 650 nm. Moreover, the $GaP_{0.67}Sb_{0.33}$ photoanode was stable for 5 h without degradation in the photocurrent in a strongly alkaline condition under continuous illumination at 1 V versus RHE.

4.2. Experimental Methods

MBE growth: The $GaP_{0.67}Sb_{0.33}$/Si sample was grown by molecular beam epitaxy (MBE) on a HF-chemically prepared n-doped ($10^{17}cm^{-3}$) Si (001) substrate, with a 6° miscut towards the [110] direction (144). The substrate was heated at 800 °C for 10 mins to remove hydrogen from the surface. A 1 µm-thick $GaP_{0.67}Sb_{0.33}$ layer was then grown at 500 °C at a conventional continuous MBE growth mode, and at a growth rate of 0.24 ML/s, with a beam equivalent pressure V/III ratio of 5. It should be noted that the whole epilayer was nominally undoped, but on the other hand epitaxial strategies to annihilate antiphase boundaries (APB) (124, 130) were not used here, leading to emerging APBs. These APBS give an equivalent n-doping concentration of the epilayer of about 10^{18} cm^3.

Materials characterization: Scanning transmission electron microscopy (STEM) high-resolution imaging and energy dispersive X-spectroscopy (EDX) were obtained using a Hitachi HD2700 AC-STEM operated at 200 kV in high-angle annular dark field (HAADF) mode. The TEM sample was prepared using an FEI FIB200 FIB and thinned to electron transparency. A focused probe (~0.1–1 nm diameter) was scanned across the sample surface, and transmitted electrons were imaged. A Raman spectrum was obtained on a Renishaw inVia micro-Raman system with 532 nm wavelength incident light.

X-ray photoelectron spectroscopy (XPS) measurements were taken with a Thermoscientific monochromated aluminium k-alfa photoelectron spectrometer, using monochromic Al-Kα radiation (1486.7 eV). Survey scans were collected in the range of 0–1300 eV with high-resolution scans for Ga 2p, Ga 3d, P 2p, Sb 3d/O 1s and C 1s. The raw data was processed using CasaXPS and calibrated to adventitious carbon at 284.5 eV.

X-ray diffraction was performed on a four-circle Brucker D8 Diffractometer (horizontal scattering plane geometry). This diffractometer is equipped with a 1D Gobel Multi-layer Mirror placed on the linear focus window of a standard sealed tube as primary optics. A Bartels asymmetric Ge (220) monochromator was used for both line scan and reciprocal space maps. The detector is a Lynxeye^{TM}, a one-dimensional position sensitive detector (PSD), allowing a collection angle of 2.6° over 2Θ.

Atomic force microscopy (AFM): The atomic force microscopy (AFM) images were obtained using a Veeco Dimension 3100 AFM microscope, which is a high-resolution scanning probe microscope with a resolution of sub-nanometer order. The microscope was used in the soft tapping mode with a standard non-contact probe with the cantilever tuned to around 190 kHz.

Atomic layer deposition of TiO_2: Atomic layer deposition of amorphous TiO_2 (20 nm) on $GaP_{0.67}Sb_{0.33}$ grown on Si substrate was deposited by a Savannah S200 ALD system and the temperature was maintained at 150 °C. The growth rates per cycle for TiO_2 were determined by a spectroscopic ellipsometer.

Optical characterizations: The optical constants of the $GaP_{0.67}Sb_{0.33}$ alloy were measured by variable angle spectroscopic ellipsometry (VASE) at room temperature in the 0.85–5 eV photon energy region. A Tauc-Lorentz model with two oscillators

was applied to fit the ellipsometry data and to extract real and imaginary parts of the refractive index in order to plot the absorption spectrum of the $GaP_{0.67}Sb_{0.33}$ alloy. The electronic structure was investigated through temperature-dependent PL measurements. The samples were placed in an ARS closed-loop cryostat where the temperature can be varied between 15 K and 300 K. The excitation source was a laser diode operating at 405 nm. The laser spot size diameter on the sample was about 50 µm and the power 9.3 mW. The luminescence signal was collected using an IHR 320 spectrometer with 300 mm^{-2} grating and an open-electrode Si CCD. The entrance slit of the spectrometer was set to 100 µm.

Band structure modelling: The band diagram of $GaP_{0.67}Sb_{0.33}$ was calculated using an extended-basis $sp^3d^5s^*$ tight-binding Hamiltonian (154). This method has proved to provide a band structure description with a sub-millielectronvolt precision throughout the Brillouin zone of binary cubic III-V and II-VI (155) semiconductors, including quantum heterostructures (156) and surfaces (157). From the tight-binding parameters of the GaP and GaSb binary compounds (154), a virtual crystal approximation was performed to obtain the $GaP_{0.67}Sb_{0.33}$ alloy band structure. The tight-binding parameters of the virtual crystal are an arithmetic mean of the constituent materials weighted to their concentration (158) except for the diagonal matrix elements related to the atomic energies of anion "s-type" and "p-type" states. For these states, bowing parameters were introduced to model the strong bowing of Γ band gap of 2.7 eV (158).With a bowing parameter equal to 9.0 eV for s-state and equal to 2.8 eV for p-state, the experimental bandgap for $GaP_{0.67}Sb_{0.33}$ is well reproduced.

Device fabrication: Before the PEC experiments were conducted, the $GaP_{0.67}Sb_{0.33}$ photoanode grown on Si substrate was fabricated by applying an indium-gallium

eutectic (Aldrich) to the back of the Si wafer. Also, the single n-GaP wafer has dopant density ~ (1×10^{18} cm^3) and was fabricated as a reference photoanode. All of the sample was attached by a copper wire using silver paste and covered by insulating epoxy.

Photoelectrochemical measurements: The PEC tests were performed in 1.0 M KOH (pH~14) electrolyte using a standard three-electrode configuration, under one-sun simulated solar light irradiation.

IPCE measurements were carried out using the same three-electrode configuration under monochromatic light using a set of filters. The device was biased at 1.23 V versus RHE. The IPCE can be computed by using the following equation.

$$\text{IPCE} = \frac{1239.8\ (V\ nm\ ) \times [\ J\ (mAcm^{-2})\ ]}{P_{mono}\ (mW\ cm^{-2}) \times \lambda\ (nm)}$$

Where J is the photocurrent density, is the monochromated illumination power intensity, and λ the wavelength. The flat-band potential and carrier concentration was calculated using the Mott−Schottky equation as given by (53):

$$\frac{1}{C^2} = -\frac{2}{q\varepsilon\varepsilon_0 A N_{dopant}}(E - E_{FB} - \frac{kT}{q})$$

Where q is the electron charge (1.602×10^{-19} C), ε is the relative dielectric constant of GaPSb, ε_0 is vacuum permittivity (8.85×10^{-12} F m^{-1}), k is the Boltzmann constant (1.38×10^{-23} J K^{-1}), and T is the absolute temperature. E_{FB} is the flat band potential. N_{dopant} is the free carrier density, A is the area of electrode, and E is the applied potential.

4.3. Results and Discussion

4.3.1. Structural Characterization of the $GaP_{0.67}Sb_{0.33}$ Photoanode

The structural properties of the $GaP_{0.67}Sb_{0.33}$ photoanode were analysed by scanning transmission electron microscopy (STEM). Figure 4.1 shows the cross-sectional STEM high-angle annular dark-field (HAADF) and annular bright-field (ABF) images at both low and high magnification of the nominally undoped 1 µm-thick $GaP_{0.67}Sb_{0.33}$ grown on an Si substrate photoanode for PEC water splitting. It shows the presence of numerous crystal twins, originating from the $GaP_{0.67}Sb_{0.33}$ on the Si interface, which introduces non-optimized growth initiation steps (89, 159). Nevertheless, the structural quality of the $GaP_{0.67}Sb_{0.33}$ grown on Si substrate is much improved compared with previous works (150, 151). As shown later, it is remarkable that despite the presence of these crystal defects, and the absence of intentional doping, the photocurrent of the $GaP_{0.67}Sb_{0.33}$ grown on the Si photoanode remains high compared to a reference n-doped GaP photoanode (with a much lower density of crystal defects), introduced in the next discussion. This behaviour is related to the presence of emerging antiphase boundaries (APBs) in the structure. Indeed, common strategies to annihilate APBs (124, 130) were not used to grow this sample, resulting in APBs propagating in the whole volume of the $GaP_{0.67}Sb_{0.33}$ epilayer, as shown in Figure 4.1. It results in an average unintentional n-doping level of 10^{18} cm^{-3}, acting as electrical shunts in the structure (160-162). Photogenerated carriers in the $GaP_{0.67}Sb_{0.33}$ epilayer are then brought to the surface or to the $GaP_{0.67}Sb_{0.33}$/Si interface more easily. Finally, the presence of APBs is also expected to create intermediate band-gap energy levels (161). STEM energy dispersive X-ray spectroscopy (EDS) measurements were carried out for elemental composition extraction. Chemical analysis of the $GaP_{0.67}Sb_{0.33}$ on the Si

photoanode is shown in Figure 4.2. Elemental profiles through the $GaP_{0.67}Sb_{0.33}$/Si interface are plotted for the involved chemical species (Si, Ga, P, and Sb). It shows that the projected interface between $GaP_{0.67}Sb_{0.33}$ and Si is relatively well defined, with an apparent intermixing layer of around 5 nm at the most. This transition area is more likely due to the residual roughness of the Si substrate than to real $GaP_{0.67}Sb_{0.33}$ on Si intermixing (159). Figure 4.2 also shows that the P and Sb contents are stable within the layer, indicating an overall composition homogeneity of the sample, within the EDS resolution.

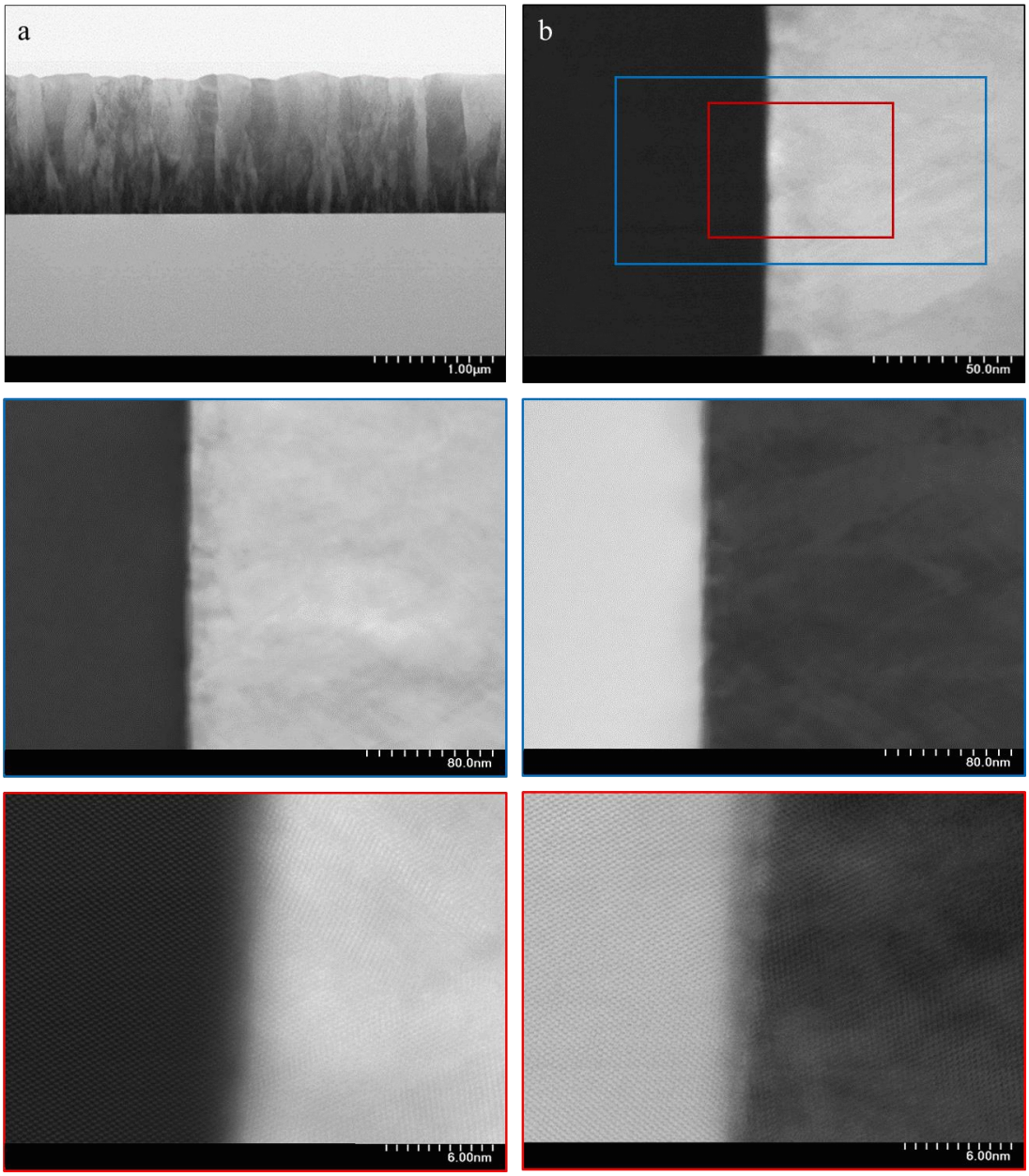

Figure 4.1. Cross-sectional high-angle annular dark-field (HAADF) and annular bright-field (ABF) images of $GaP_{0.67}Sb_{0.33}$ on the silicon photoanode. **(a)** A cross-sectional annular bright-field (ABF) STEM image of $GaP_{0.67}Sb_{0.33}$ grown on Si substrate. **(b)** STEM HAADF and ABF images at both low and high magnification of the $GaP_{0.67}Sb_{0.33}$ grown on the Si photoanode.

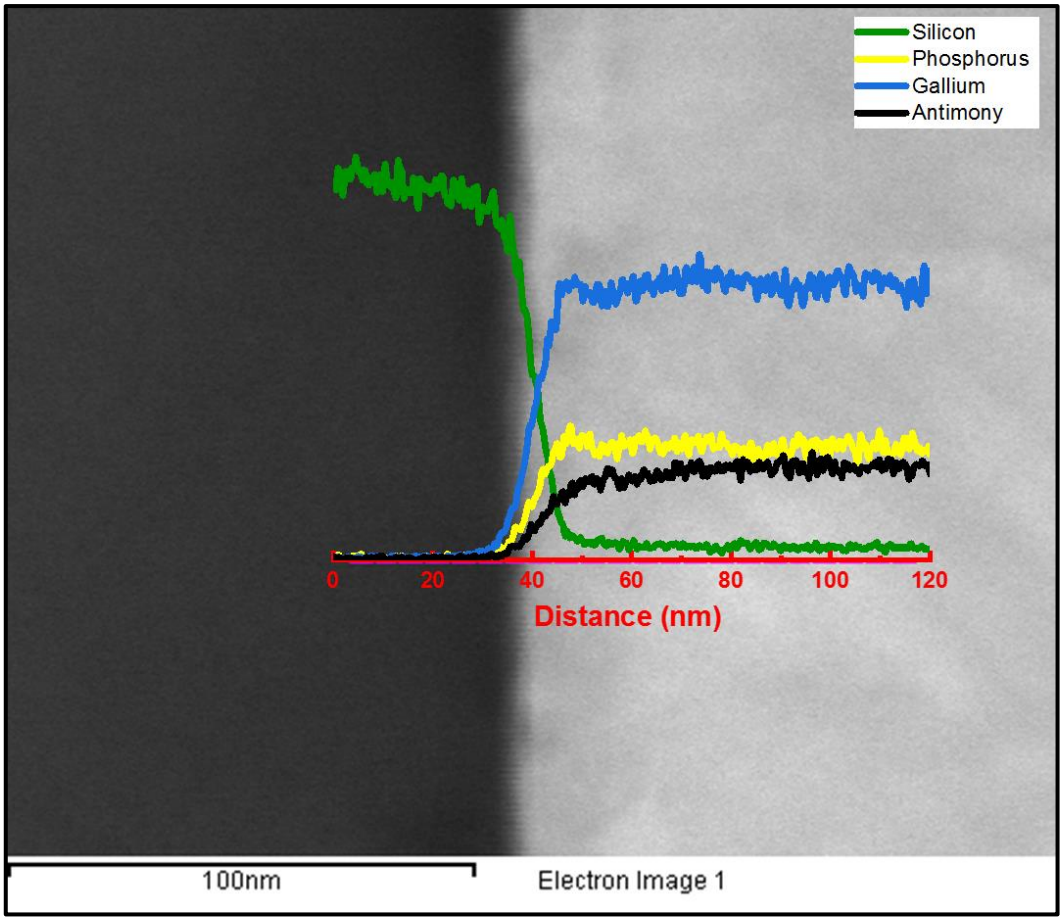

Figure 4.2. STEM-dispersive X-ray spectroscopy (EDS) (colour online) showing the Si, Ga, Sb, and P concentration depth profiles for $GaP_{0.67}Sb_{0.33}$ grown on the silicon substrate.

The X-ray photoelectron spectroscopy (XPS) analysis of the surface also shows the formation of a very standard $GaP_{0.67}Sb_{0.33}$-based native oxide, as shown in Figure 4.3. Surface properties of as-grown $GaP_{0.67}Sb_{0.33}$/Si were inferred from XPS. The XPS survey scan shown in Figure 4.3(a) shows the expected Ga, P, Sb, O, and C transitions on the surface. Figure 4.3(b) shows the Ga 2p transition with the Ga $2p_{3/2}$ peak centred at 1117.0 eV, which matches literature for Ga in the 3+ oxidation state and bound to species such as P or As (163). The Ga 3d peak in Figure 4.3(c) however shows a clear shoulder and thus can be deconvoluted with two sets of doublets, therefore suggesting two different Ga environments. The primary Ga $3d_{5/2}$ peak centred at 19.1 eV corresponds to Ga 3+ bound to P, whereas the secondary Ga $3d_{5/2}$ peak centred at 20.6 eV matches Ga bound to O in the native oxide Ga_2O_3 (164, 165). The P 2p region shows two peaks that can be deconvoluted with the primary $2p_{3/2}$ peak at 128.8 eV and matching P in the -3 oxidation state and therefore corresponding to P bound to Ga in GaP, as shown in Figure 4.3(d) (164, 165). The secondary $2p_{3/2}$ peak at 133.3 eV matches P in the 5+ oxidation state and may be attributed to native oxide species (164, 165). Two Sb environments can be seen, the first of which is a Sb $3d_{5/2}$ peak at 530.2 eV corresponding to Sb in the 3+ oxidation state (166, 167). An additional Sb $3d_{5/2}$ peak at 527.3 eV is too low in energy to correspond to metallic Sb, which is often found at 528.0 eV; therefore, this peak at 527.3 eV is thought to correspond to Sb in the -3 oxidation state and in the form of GaSb, as shown in Figure 4.3(e). Previous XPS studies of GaSb have focused only on the Sb 4d transition and therefore comparison of this peak to literature values is not possible (168, 169).

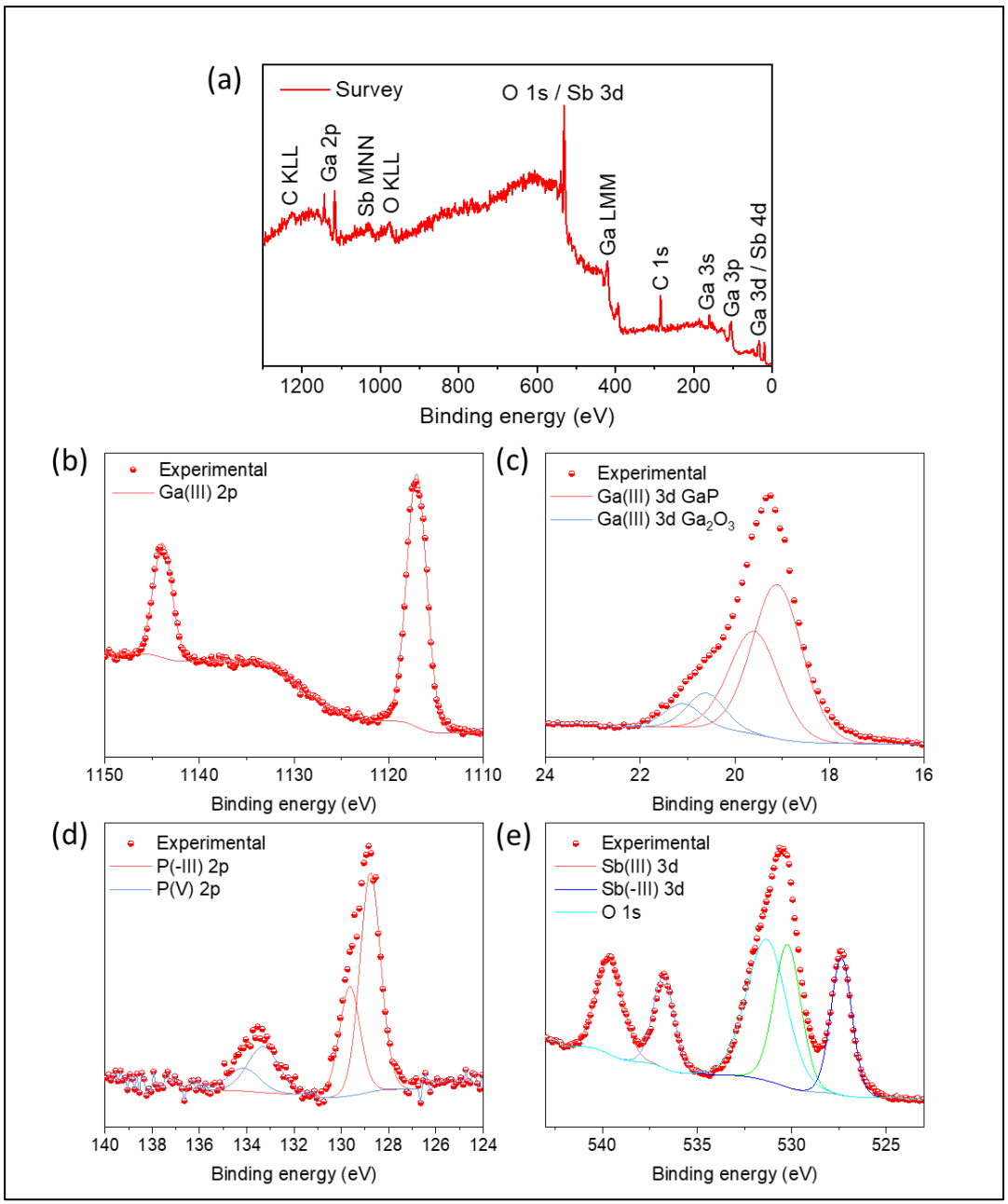

Figure 4.3. X-ray photoelectron spectroscopy (XPS) spectra of $GaP_{0.67}Sb_{0.33}$ grown on the silicon substrate photoanode. **(a)** Survey scan for $GaP_{0.67}Sb_{0.33}$ on Si shows the expected Ga, P, Sb, and O and C transitions and the high-resolution **(b)** Ga 2p, **(c)** Ga 3d, **(d)** P 2p, and **(e)** Sb 3d/O 1s transitions.

Figure 4.4(a) presents the results of X-ray diffraction (XRD) analysis on the $GaP_{0.67}Sb_{0.33}$ grown on Si substrate. A miscut of 6.1 ± 0.05° was observed towards the [110] direction, from the positions of the Si Bragg peaks, in agreement with the substrate specifications. The $\omega/2\theta$ scan exhibits a well-defined $GaP_{0.67}Sb_{0.33}$ Bragg peak. Reciprocal space maps carried out on either (224) or (004) reflections, as shown in Figure 4.4(b-c), show a full plastic relaxation of the $GaP_{0.67}Sb_{0.33}$ layer. Very similar values of the $GaP_{0.67}Sb_{0.33}$ lattice parameter have been extracted from both RSM and the $\omega/2\theta$ scan, confirming the full plastic relaxation rate and giving a mean lattice parameter of 0.5665 ± 0.0005 nm. An antimony content of 0.33 ± 0.01 in $GaP_{0.67}Sb_{0.33}$ is then inferred from these values (170). The observed position of the $GaP_{0.67}Sb_{0.33}$ peak overlaps the relaxation line (bold dashed line in Figure 4.4(b-c)). This corresponds to a supplementary tilt of the order of 0.4°. This is classically interpreted as the contribution of the miscut to the plastic relaxation process. The $\Delta\alpha$ Nagai angle of 0.25° is calculated by:

$$\tan(\Delta\alpha) = \left[\frac{(a_{op} - a_s)}{(a_s)}\right] \tan(\alpha)$$

Where α is the miscut value, a_{op} is the out of plane lattice parameter of the layer (here the measured value), and a_S is the substrate lattice parameter (171). A supplementary tilt of the order of 0.15° and a large broadening of the reflections are observed in agreement with the formation of a large density of 60° misfit dislocations. Finally, the XRD analysis does not give any evidence of a phase separation that could occur between GaP and GaSb in the metastable GaPSb alloy.

Figure 4.4(d) shows the Raman spectrum of $GaP_{0.67}Sb_{0.33}$ grown on a Si photoanode. This spectrum exhibits four clearly distinct peaks, in groups of two, at 190, 230, 335, and 370 cm^{-1}, respectively. These lines are significantly shifted as compared to conventional Raman scattering spectra of bulk GaSb (at 230 and 237 cm^{-1} for TO and LO phonons) and bulk GaP (367 and 403 cm^{-1} for TO and LO phonons) (172). The spectrum has the typical shape observed for a "two-mode" system, common for ternary III-V alloys, that displays two distinct sets of optical modes with frequencies characteristic of each end member (173). The observed Raman peaks are thus attributed respectively to GaSb-like TO and LO phonons, and GaP-like TO and LO phonons. The clear identification of the four peaks is an indication of the long-range coherency of the alloy, together with low composition fluctuations, despite the presence of crystal defects. In the "two-mode" systems, the relative intensities of Raman lines are usually roughly proportional to the respective concentrations. This is not the case here, where GaSb-like peaks are larger than GaP-like peaks. The very different sizes of P and Sb atoms strongly impact on the respective phonons' propagation, and thus may explain this observation. Overall, the 1 µm-thick $GaP_{0.67}Sb_{0.33}$ epilayer on the Si used as the photoanode is composed of X=0.33 of Sb and is fully plastically relaxed with a slight tilt induced during the plastic relaxation. Antiphase boundaries emerge at the sample surface, allowing the carrier's transport in the sample. Despite the observation of some crystal defects, significant composition fluctuations are not evidenced.

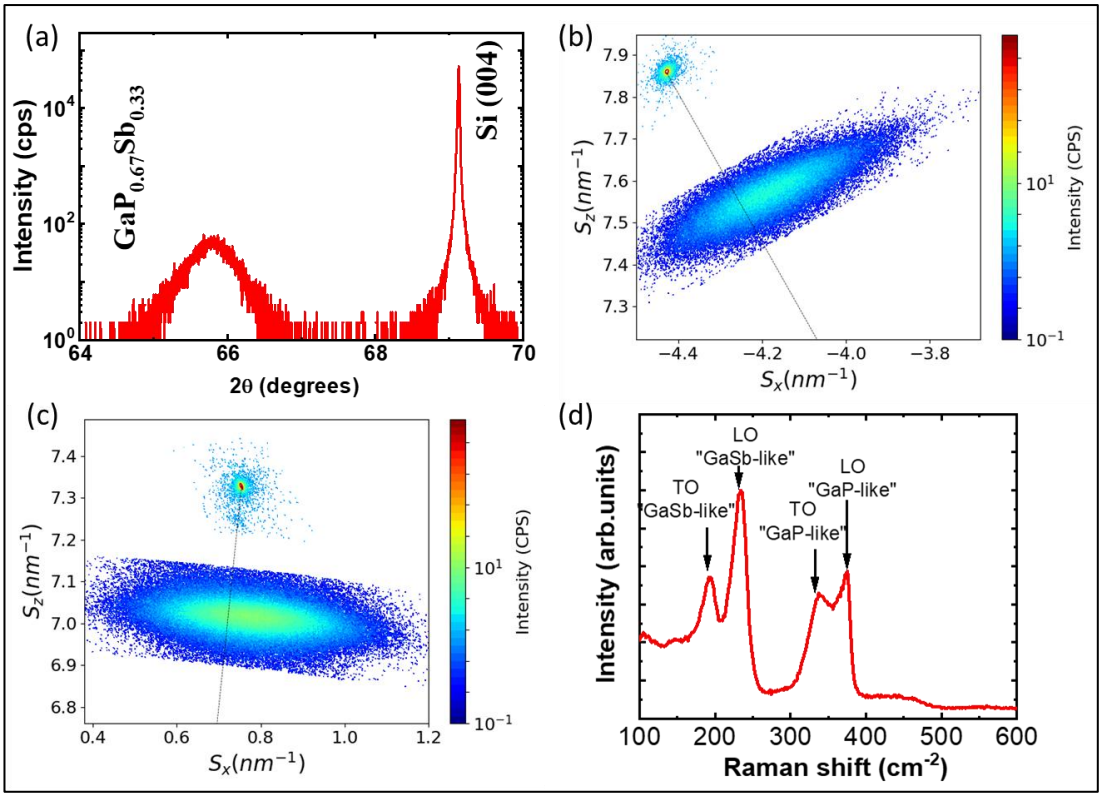

Figure 4.4. X-ray diffraction and Raman spectra of $GaP_{0.67}Sb_{0.33}$ photoanode. **(a)** X-ray diffraction $\omega/2\theta$ scan performed in the vicinity of the Si (004) Bragg reflection showing the distant $GaP_{0.67}Sb_{0.33}$ peak. **(b)** and **(c)** show the reciprocal space map around (224) illustrating the full relaxation state of $GaP_{0.67}Sb_{0.33}$ (S_x and S_z are the projected coordinates in the right-handed Cartesian, with the z axis parallel to the surface normal(170)). **(d)** Raman scattering spectrum of the $GaP_{0.67}Sb_{0.33}$ photoanode showing the two-mode (GaP-like and GaSb-like) structuration, composed of both LO and TO phonons.

4.3.2. Electronic and Optical Characterizations

4.3.2.1. Tight Binding Calculation

To further investigate the electronic properties of the $GaP_{0.67}Sb_{0.33}$ grown on the Si photoanode, the band structure of the unstrained $GaP_{0.67}Sb_{0.33}$ alloy was calculated using a tight-binding method, with an extended-basis $sp^3d^5s^*$ tight-binding Hamiltonian (154); this is shown in Figure 4.5(a). The band gaps obtained in the Γ, L, and X valleys are respectively 1.753, 1.784, and 2.071 eV at 0 K. The alloy therefore has a direct band-gap band structure. The values found in these calculations are in good agreement with those determined from the absorption spectrum deduced by ellipsometry measurements at 300 K in Figure 4.6 (1.65 eV), considering a conventional 50–70 meV temperature shift. It is also consistent with the IPCE curve presented in Figure 4.11(a) that shows significant photocurrent generation just below 750 nm. Finally, the band gap determined in this study is also in agreement with the pioneering works on $GaP_{1-x}Sb_x$ by Loualiche et al (174). Water redox potentials of H^+/H_2 and O_2/H_2O are relatively positioned with black dashed lines in Figure 4.5(a), with respect to the $GaP_{0.67}Sb_{0.33}$ alloy valence band. To do this, the absolute band lineup between GaP and GaSb (175) and the absolute band lineups between GaP and the water redox potentials was used (176). An energy shift of 0.41 eV is needed to align the valence band maximum and the O_2/H_2O energy level, as illustrated by the blue dashed lines in Figure 4.5(a). In the present study, the large band bending in the $GaP_{0.67}Sb_{0.33}$ grown on Si substrate cannot be predicted accurately, because of the surface pinning and the presence of APDs. Therefore, the advantages of $GaP_{0.67}Sb_{0.33}$ through accurate monitoring of Sb content, as compared to GaP, extends the absorption spectral range and direct band gap transition.

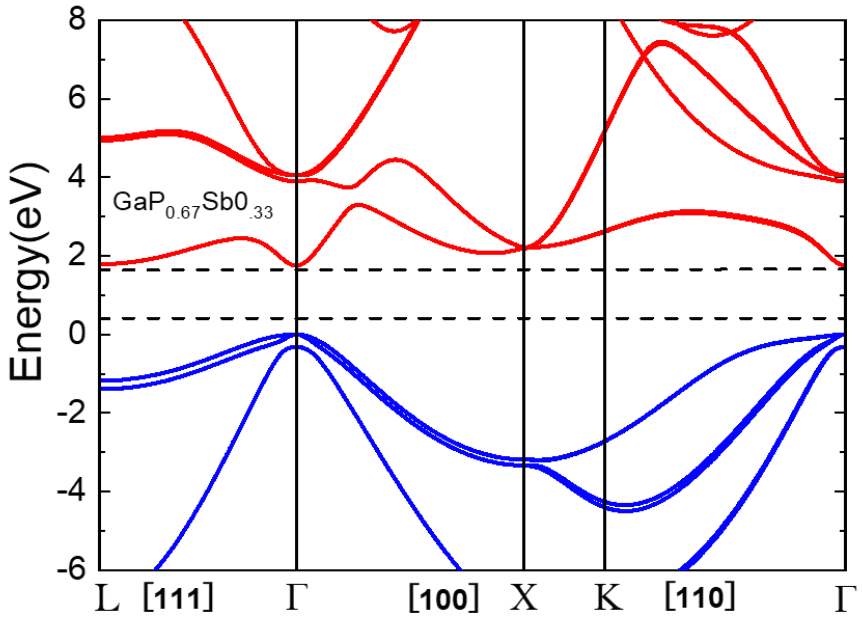

E_g(L)(eV)	E_g(Γ)(eV)	E_g(X)(eV)
1.784	1.753	2.071

Figure 4.5. Electronic and optical properties of $GaP_{0.67}Sb_{0.33}$ grown on the silicon substrate photoanode. **(a)** Band structure of the bulk unstrained $GaP_{0.67}Sb_{0.33}$ at 0 K. Band gaps of 1.753, 1.784, and 2.071 eV are computed for the Γ, L, and X valleys, respectively. Relative positions of the water redox potentials are superimposed.

4.3.3. Ellipsometry and Photoluminescence (PL) Measurement

The optical constants of the $GaP_{0.67}Sb_{0.33}$ alloy was measured by variable angle spectroscopic ellipsometry (VASE) at room temperature in the 0.85–5 eV photon energy region, as shown in Figure 4.6. The angles of incidence were set to 60˚ and 70˚. A Tauc-Lorentz model with two oscillators was used to fit the ellipsometry data and extract the absorption coefficient value. Figure 4.6(a) shows the fitting result. The red and blue lines correspond to experimental spectra where I_s and I_c parameters are represented. I_s and I_c are related to the well-known ellipsometry variables ψ (amplitude component) and Δ (phase difference) through the following relations: I_s =

$\sin(2\psi).\sin(\Delta)$, $I_c = \sin(2\psi).\cos(\Delta)$. The black lines correspond to the theoretical curves after adjusting the parameters of the Tauc-Lorentz model. From this model, the refractive index (n), extinction coefficient (k), and absorption spectrum of the sample were extracted, as shown in Figure 4.6(b). A Tauc plot ($(\alpha h\nu)^2$ versus $h\nu$) was used to evaluate the band gap of the $GaP_{0.67}Sb_{0.33}$ grown on a silicon photoanode in the absorption coefficient range 3000–1000 cm^{-1}, which were shown in Figure 4.6(c). The band gap range of the $GaP_{0.67}Sb_{0.33}$ grown on a silicon photoanode was obtained: E_g=1.643–1.762 eV for $GaP_{0.67}Sb_{0.33}$, which is consistent with the literature data (174).

The optical properties of the $GaP_{0.67}Sb_{0.33}$ photoanode were further studied using photoluminescence (PL) spectroscopy, as shown in Figure 4.6(d). Figure 4.6(d) provides the temperature-dependent PL analysis for this sample. A PL signal was detected up to 150 K. At first, two transitions are clearly distinguishable, at 1.22 eV (low-energy line –LEL) and 1.38 eV (high-energy line – HEL), respectively. From the experimental absorption curve presented in Figure 4.4(c), and calculations presented in Figure 4.2(a), the emission properties of the sample cannot be attributed to the band gap of the bulk $GaP_{0.67}Sb_{0.33}$ (which lies around 1.7 eV at low temperature). This strong Stokes-shift is necessarily a consequence of deep carrier localization in the $GaP_{0.67}Sb_{0.33}$ layer. The PL peaks were fitted by using a two-component Gaussian curve to deduce the Arrhenius evolutions for each PL peak, as shown in Figure 4.2(b) inset. The fitting of Arrhenius evolutions requires three activation energies, which are identical for the two lines: 8 meV, 30 meV, and 130 meV. The first one is attributed to a small alloy disorder, while the two others represent the detrapping of localized carriers to extended states. Interestingly, if the photoluminescence is not robust with increasing temperature, the 15 K PL intensity is significantly larger than that usually measured in GaP-based quantum dots or quantum wells, which are of the indirect type

(92, 177). Therefore, it concluded that this PL signal comes from localization of excitons in the sample, with a direct band gap. However, due to the various crystal defects shown in Figure 4.1, the non-radiative lifetime is short, and redistribution of carriers to the non-radiative centres hampers the observation of room-temperature PL. It is worth noting that localization of carriers around non-radiative or radiative centres does not prevent good operation of the photoanode. The presence of antiphase boundaries, acting as preferential transport channels (and thus preventing the carriers to visit non-radiative centres) may again explain this observation.

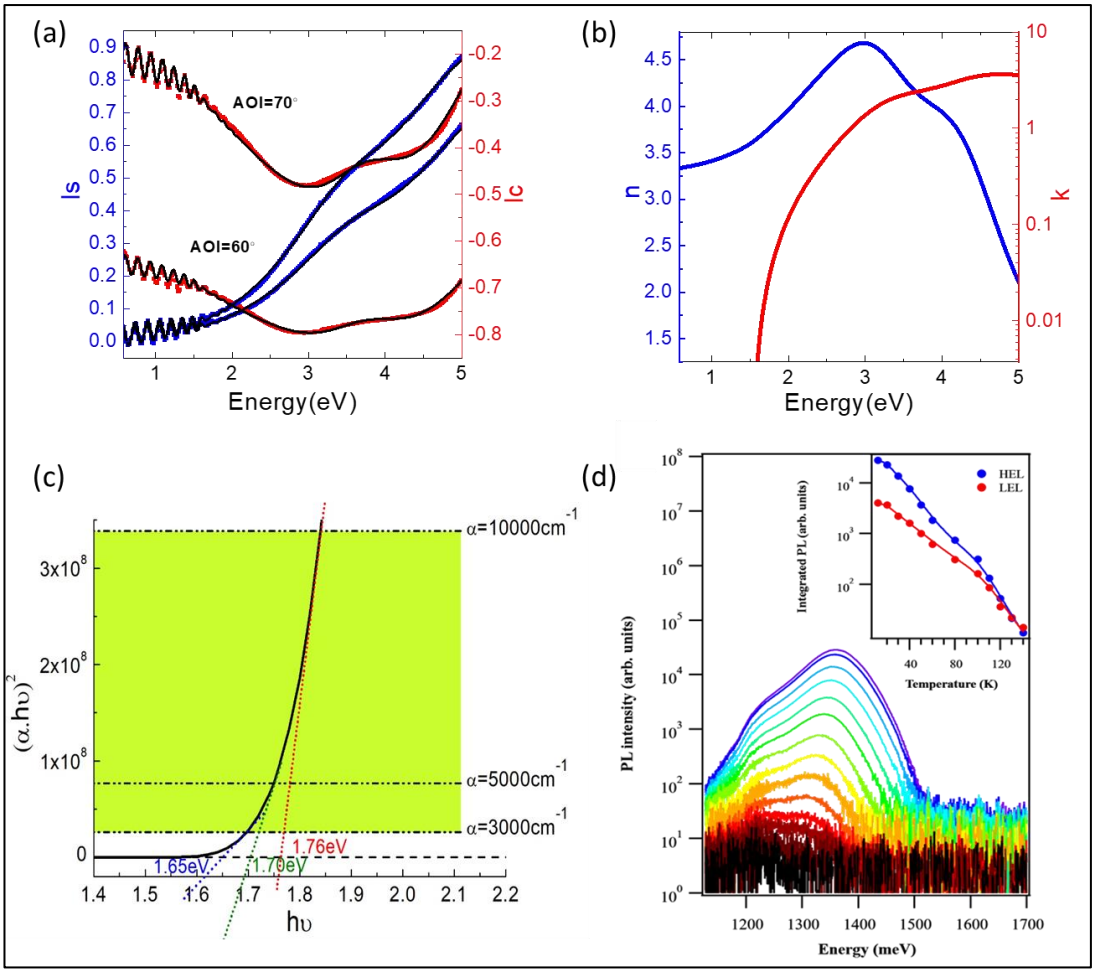

Figure 4.6. Optical properties of $GaP_{0.67}Sb_{0.33}$ grown on a silicon photoanode. **(a)** Experimental ellipsometry spectra of I_s and I_c for two incidence angles (red and blue lines) and comparison with theoretical curves by using a two-oscillator Tauc-Lorentz model (black lines). **(b)** n (optical index real part) and k (optical index imaginary part) optical constants of $GaP_{0.67}Sb_{0.33}$ grown on silicon extracted from the fitting of (a). **(c)** Tauc plot of $(\alpha hv)^2$ versus photon energy (hv) for $GaP_{0.67}Sb_{0.33}$ grown on a silicon photoanode. **(d)** Temperature-dependent photoluminescence spectra between 15 K and 150 K showing a large Stokes-shift, evidencing carrier localization. Inset is the corresponding Arrhenius plot for the two transitions, being low-energy line (LEL) and high-energy line (HEL).

4.3.4. Photoelectrochemical Performance of the $GaP_{0.67}Sb_{0.33}$ Photoanode

Figure 4.7(a-b) shows a schematic diagram of the structure of the $GaP_{0.67}Sb_{0.33}$ photoanode coating with a TiO_2 protection layer after being combined with the Ni co-catalyst. The experimental setup that was used for the PEC measurements consisted of a working electrode ($GaP_{0.67}Sb_{0.33}$), reference electrode (Ag/AgCl), and counter electrode (platinum coil). The PEC performance of the $GaP_{0.67}Sb_{0.33}$ photoanodes was investigated using a standard three-electrode configuration in 1.0 M KOH electrolyte (pH 14) under one-sun illumination.

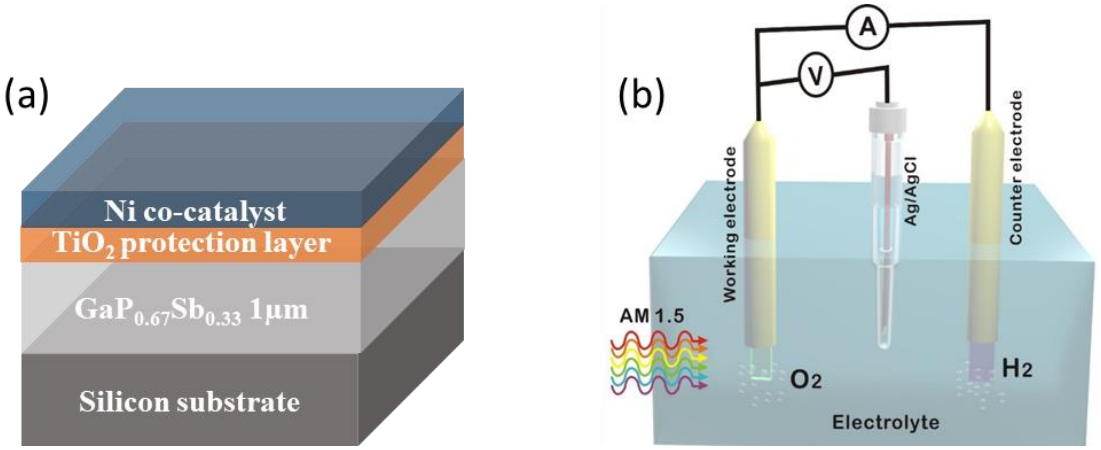

Figure 4.7. Illustration of structure and PEC setup for the $GaP_{0.67}Sb_{0.33}$ photoanode. **(a)** Schematic diagram of structure for the $GaP_{0.67}Sb_{0.33}$ photoanode coating with protection layer (TiO_2) and co-catalyst (Ni). **(b)** The experimental setup using a three-electrode system for the photoelectrochemical measurements.

The photocurrent density–voltage *(J–V)* curve for the $GaP_{0.67}Sb_{0.33}$ photoanode without coating is shown in Figure 4.8(a). Under AM 1.5G simulated one-sun illumination, it shows that the onset potential for the $GaP_{0.67}Sb_{0.33}$ photoanode without coating is 0.4 V versus the reversible hydrogen electrode (RHE), and this onset potential correlates with the flat-band potential of the photoanode, which is also determined by the Mott–Schottky measurement in Figure 4.8(b). The saturated photocurrent density was 13.26 mA/cm^2 at 1.23 V versus the reversible hydrogen electrode (RHE). The dark current usually has a measurement of 0 V but was observed to have a high voltage; that arises from self-corrosion, since the $GaP_{0.67}Sb_{0.33}$ oxidation potential is above the oxygen evolution potential (151). In addition, the oxidation photocorrosion of the $GaP_{0.67}Sb_{0.33}$ photoanode without coating could be from accumulation of holes on the surface of photoanode and oxidized itself instead of electrolyte (10, 13,151). To determine the flat-band potentials of the $GaP_{0.67}Sb_{0.33}$ photoanode without coating and donor concentration, the Mott−Schottky measurements in three electrode configurations in 1.0 M KOH (pH 14) were performed, as shown in Figure 4.8(b). The slope is positive, which indicates the electrode is an n-type material. The flat-band potential (V_{FB}) and the donor concentration were 0.5 V and 3.86 $\times 10^{15}$ cm^{-3} versus RHE, respectively.

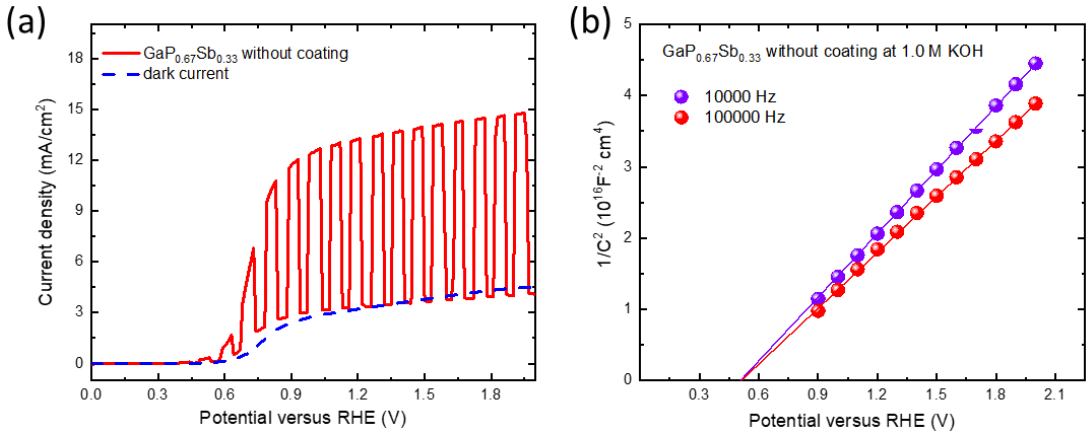

Figure 4.8. PEC measurements for the $GaP_{0.67}Sb_{0.33}$ photoanode. **(a)** Current density versus applied voltage (J–V) curve of the $GaP_{0.67}Sb_{0.33}$ photoanode without coating in 1.0 M KOH (pH 14) electrolyte under simulated AM1.5 illumination versus RHE. **(b)** Mott–Schottky (M–S) plot as a function of the applied potential (E) for the $GaP_{0.67}Sb_{0.33}$ photoanode without coating at 10 kHz and 100 kHz.

On the other hand, an ALD-TiO_2 of 20 nm thickness was deposited directly onto the surface of the $GaP_{0.67}Sb_{0.33}$ photoanode as a protection layer from photocorrosion water oxidation. 8 nm of metallic nickel (Ni) was deposited by a thermal evaporation tool onto the surface of the $GaP_{0.67}Sb_{0.33}$-TiO_2 photoanode as a co-catalyst. Figure 4.9(a) presents the current density versus potential (*J–V*) for the $GaP_{0.67}Sb_{0.33}$ photoanode coated with TiO_2 and Ni and the $GaP_{0.67}Sb_{0.33}$ photoanode coated with Ni in 1.0 M KOH (pH 14) electrolyte under one-sun illumination. As shown in Figure 4.9(a), the $GaP_{0.67}Sb_{0.33}$ coated with 8 nm of Ni showed an onset potential of 0.37 V and a saturated current density of 3.84 mA/cm^2 at 1.23 V versus RHE. In contrast, the $GaP_{0.67}Sb_{0.33}$ coated with TiO_2 (20 nm) and Ni (8 nm) showed significant improvement by increasing the photocurrent and a slight anodic shift to the onset potential relative to that of the $GaP_{0.67}Sb_{0.33}$ coated with Ni (8 nm).

The onset potential shifted slightly to 0.35 V and the current density was 4.82 mA/cm^2 at 1.23 V versus RHE. In the absence of the light, the dark current was zero compared to the $GaP_{0.67}Sb_{0.33}$ without coating and $GaP_{0.67}Sb_{0.33}$ photoanode coated with Ni (8 nm), which is attributed to the effectiveness of the protection layer formed by TiO_2 with the Ni co-catalyst. It clearly shows that the $GaP_{0.67}Sb_{0.33}$ photoanode coated with TiO_2 and Ni improved the PEC performance and photostability.

The current density versus potential (*J*–*V*) for three electrodes ($GaP_{0.67}Sb_{0.33}$ without coating, $GaP_{0.67}Sb_{0.33}$ coated with Ni (8 nm), and $GaP_{0.67}Sb_{0.33}$ photoanode coated with TiO_2 (20 nm) and Ni (8 nm)) after six potential sweeping scans are shown in Figure 4.9(b). As shown in Figure 4.9(b), the $GaP_{0.67}Sb_{0.33}$ without coating exhibited a sharp reduction in the photocurrent due to photocorrosion under a corrosive electrolyte, which is consistent with the stability of the electrode revealed in the next discussion. In contrast, the $GaP_{0.67}Sb_{0.33}$ coated with Ni and the $GaP_{0.67}Sb_{0.33}$ coated with TiO_2 and Ni showed no change in the current versus potential (*J*–*V*) behaviour under the same conditions, which suggests that there is good protection of the TiO_2 layer and that the Ni catalyst is highly active (10).

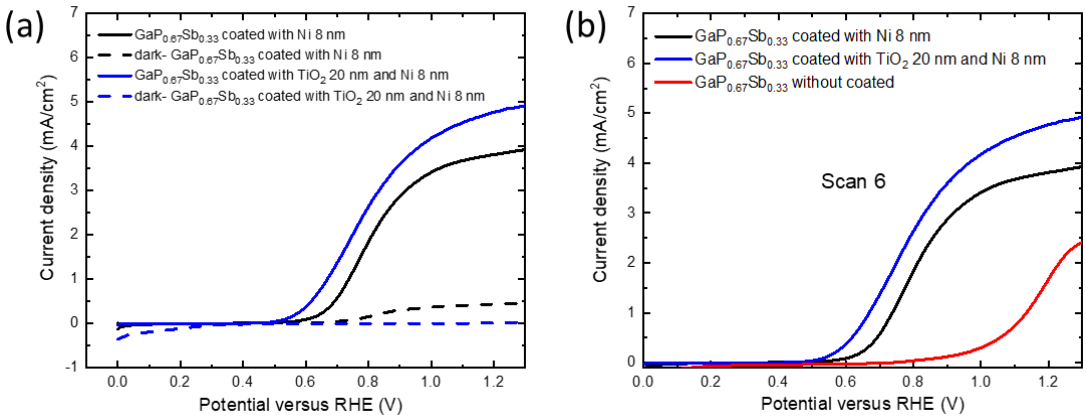

Figure 4.9. Photoelectrochemical performance of the $GaP_{0.67}Sb_{0.33}$ photoanode after using protection and co-catalyst layers. **(a)** Current density versus applied voltage (*J*–*V*) curve of the $GaP_{0.67}Sb_{0.33}$ photoanode coated with Ni (8 nm) and the $GaP_{0.67}Sb_{0.33}$ coated with TiO_2 (20 nm) and Ni (8 nm) in 1.0 M KOH electrolyte under simulated AM1.5 illumination versus RHE. **(b)** Current density versus applied voltage (*J*–*V*) curves (scan number 6) for the photoanodes from (a).

The incident photon-to-current conversion efficiency (IPCE) as a function of wavelength for the $GaP_{0.67}Sb_{0.33}$ photoanodes was further investigated at an applied bias of 1.23 V versus RHE in 1.0 M KOH electrolyte (pH 14). As shown in Figure 4.10(a), the narrow band gap of the $GaP_{0.67}Sb_{0.33}$ photoanode with composition shows an enhanced photoresponse over the visible light range from 400 nm to 700 nm, which leads to the high photocurrent density. This observation is consistent with the measured optical absorption coefficient of $GaP_{0.67}Sb_{0.33}$ and shows the interest of the bandgap extension due to the incorporation of Sb in Figure 4.10(a). For the $GaP_{0.67}Sb_{0.33}$ photoanode without coating, the maximum IPCE was 58.5% at 400 nm and decreased rapidly to 18.6% at 550 nm, which is attributed the oxidation/corrosion of the electrode. Compared with a reference GaP photoanode, the maximum IPCE value for the GaP photoanode was ∼ 53.2% at 400 nm and decreased towards longer wavelengths (> 550 nm), as shown in Figure 4.10(b). This is due to the large and

indirect band gap of GaP (2.26 eV) (15, 72). By depositing (8 nm) Ni as the co-catalyst, significant improvement was noticed. A maximum of 63% IPCE was achieved for the $GaP_{0.67}Sb_{0.33}$ coated with (8 nm) Ni at 400 nm and it gradually decreased to 53.4% at 550 nm. The IPCE of the $GaP_{0.67}Sb_{0.33}$ photoanode coated with Ni (8 nm) over the visible light region from 400 nm to 650 nm is as high as 51.16% due to a highly active oxygen evolution catalyst (10). In contrast, the $GaP_{0.67}Sb_{0.33}$ photoanode coated with TiO_2 (20 nm) and Ni (8 nm) reached a high IPCE of 76.4% at 400 nm and 67.1% between 400 nm to 650 nm, which indicates efficient and fast charge transfer to the semiconductor/electrolyte interface. Beyond 700 nm, the IPCE falls and tends to zero at around 750 nm in agreement with the energy bandgap (1.65 eV) deduced from the measured $GaP_{0.67}Sb_{0.33}$ absorption spectrum.

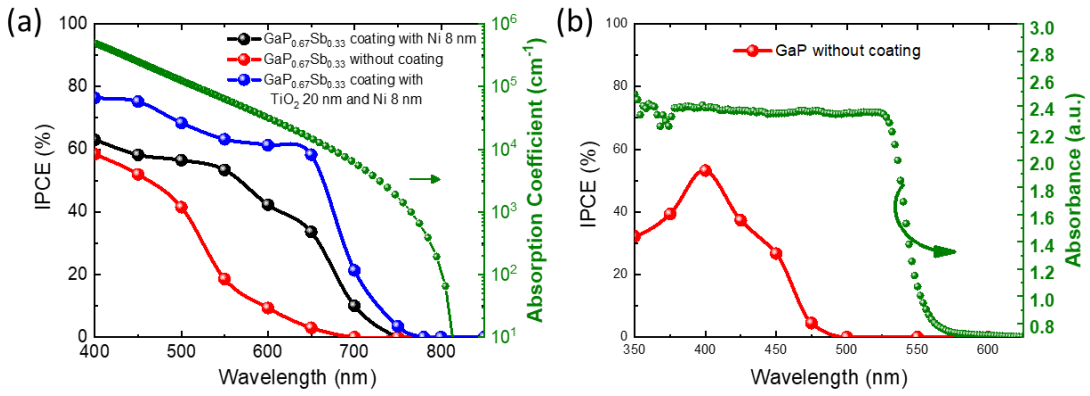

Figure 4.10. Incident photon-to-current conversion efficiency (IPCE) of the GaP and $GaP_{0.67}Sb_{0.33}$ photoanodes. **(a)** IPCE of the $GaP_{0.67}Sb_{0.33}$ photoelectrode without coating, $GaP_{0.67}Sb_{0.33}$ photoelectrode coated with Ni (8 nm), and $GaP_{0.67}Sb_{0.33}$ photoelectrode coated with TiO_2 (20 nm) and Ni (8 nm) in 1.0 M KOH electrolyte at 1 V versus RHE and the optical absorption spectrum (for $GaP_{0.67}Sb_{0.33}$) that shows a band-gap absorption edge at 1.65 eV. **(b)** Spectrum response for the GaP photoanode in 1.0 M KOH (pH 14) electrolyte at 1 V versus RHE under simulated sunlight using an AM1.5G filter.

4.3.5. Stability Evaluation of the $GaP_{0.67}Sb_{0.33}$ Photoanode

The stability of III-V semiconductors in aqueous solution is a critical challenge (41). To assess the stability of the $GaP_{0.67}Sb_{0.33}$ photoanodes, the photocurrent density versus time (*J–t*) characteristics of electrodes were investigated at a constant potential of 1 V versus RHE in a corrosive solution of 1.0 M KOH (pH 14), as shown in Figure 4.11(a-b). The photocurrent of the $GaP_{0.67}Sb_{0.33}$ without coating significantly decreased, which is attributed to photocorrosion. However, after the modification of the $GaP_{0.67}Sb_{0.33}$ surface by deposition (8 nm) of Ni as the co-catalyst, which is denoted as the $GaP_{0.67}Sb_{0.33}$ coated with Ni (8 nm), the photocurrent current stood for around 1.30 h with little decay in the current density and decreased sharply after that. Clearly, depositing Ni onto the surface of the $GaP_{0.67}Sb_{0.33}$ photoanode ($GaP_{0.67}Sb_{0.33}$ coated with Ni 8 nm) reduced the photocorrosion of the electrode. In contrast, using the corrosion resistance of TiO_2 (20 nm) and the Ni co-catalyst (8 nm) resulted in a drastic improvement in the stability of the electrode ($GaP_{0.67}Sb_{0.33}$ coated with TiO_2 (20 nm) and Ni (8 nm), as shown in Figure 4.11(b). The photocurrent of the $GaP_{0.67}Sb_{0.33}$ coated with TiO_2 (20 nm) and Ni (8 nm) remained stable for 5 hours without degradation whereas the $GaP_{0.67}Sb_{0.33}$ without the protective TiO_2 layer failed within 1.30 h. These results are attributed to the well-known corrosion resistance of TiO_2 in combination with the highly active Ni catalyst, which is consistent with previous reports (10).

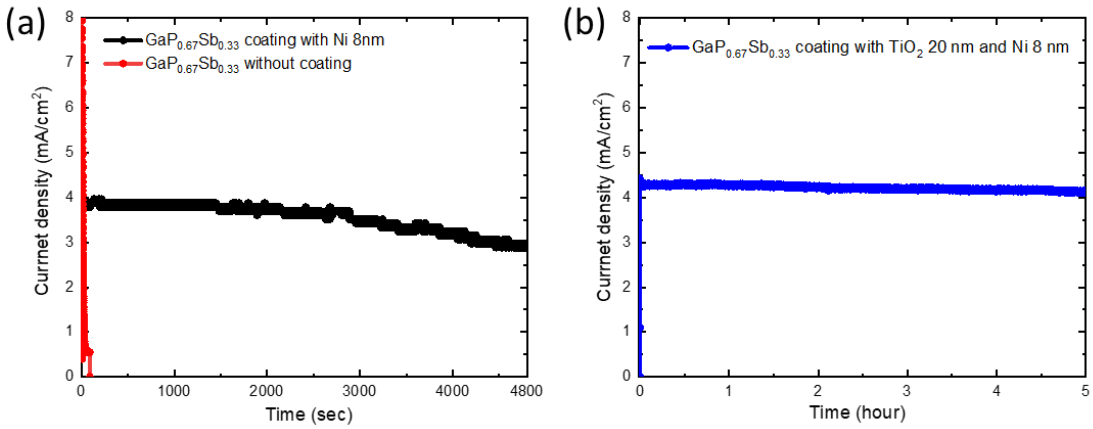

Figure 4.11. Stability assessment of $GaP_{0.67}Sb_{0.33}$ photoanodes. **(a)** Photocurrent density versus time (*J*–*t*) for the $GaP_{0.67}Sb_{0.33}$ photoanode without coating and the $GaP_{0.67}Sb_{0.33}$ photoanode coated with Ni (8 nm) in 1.0 KOH (pH 14) aqueous solution under one-sun illumination. **(b)** Chronoamperometric photocurrent density versus time (*J*–*t*) for the $GaP_{0.67}Sb_{0.33}$ photoanode coated with TiO_2 (20 nm) and Ni (8 nm) in 1.0 KOH (pH 14) aqueous solution under one-sun illumination.

To further investigate the morphology of the $GaP_{0.67}Sb_{0.33}$ photoanode coated with TiO_2 and Ni before and after a 5 h stability test in 1.0 M KOH (pH 14) electrolyte, we studied the surface of the electrode by atomic force microscopy (AFM), as shown in Figure 4.11. Growth of $GaP_{0.67}Sb_{0.33}$ directly on an Si substrate is challenging due to a large lattice mismatch between the two materials, which causes a strain to build up in the $GaP_{0.67}Sb_{0.33}$ layer. As the strain is released, dislocations form within the crystal, leading to the creation of defects and high surface roughness. An AFM image of the $GaP_{0.67}Sb_{0.33}$ surface without coating (as grown by MBE) is shown in Figure 4.11(a). The RMS (root-mean-square) roughness of this surface was calculated at 13.3 nm. After deposition of TiO_2 by ALD and the Ni catalyst by thermal evaporation, the surface morphology, as shown in Figure 4.11(b), remains comparable to the $GaP_{0.67}Sb_{0.33}$ without coating as grown by MBE with a slight increase in RMS surface roughness to 15.3 nm. In contrast, the morphology of the surface of the $GaP_{0.67}Sb_{0.33}$ photoanode coated with TiO_2 and Ni after the 5 h stability test was changed slightly as the sharp features smoothed out, as shown in Figure 4.11(c). However, the overall RMS roughness increased to 20.6 nm, which could be attributed to the etching of the photoanode surface due to the harsh condition of the corrosive high-pH solution. From these observations, it can be inferred that the quality of the $GaP_{0.67}Sb_{0.33}$ as-grown semiconductor has most impact on the surface roughness of the final sample ($GaP_{0.67}Sb_{0.33}$ coated with TiO_2 and Ni).

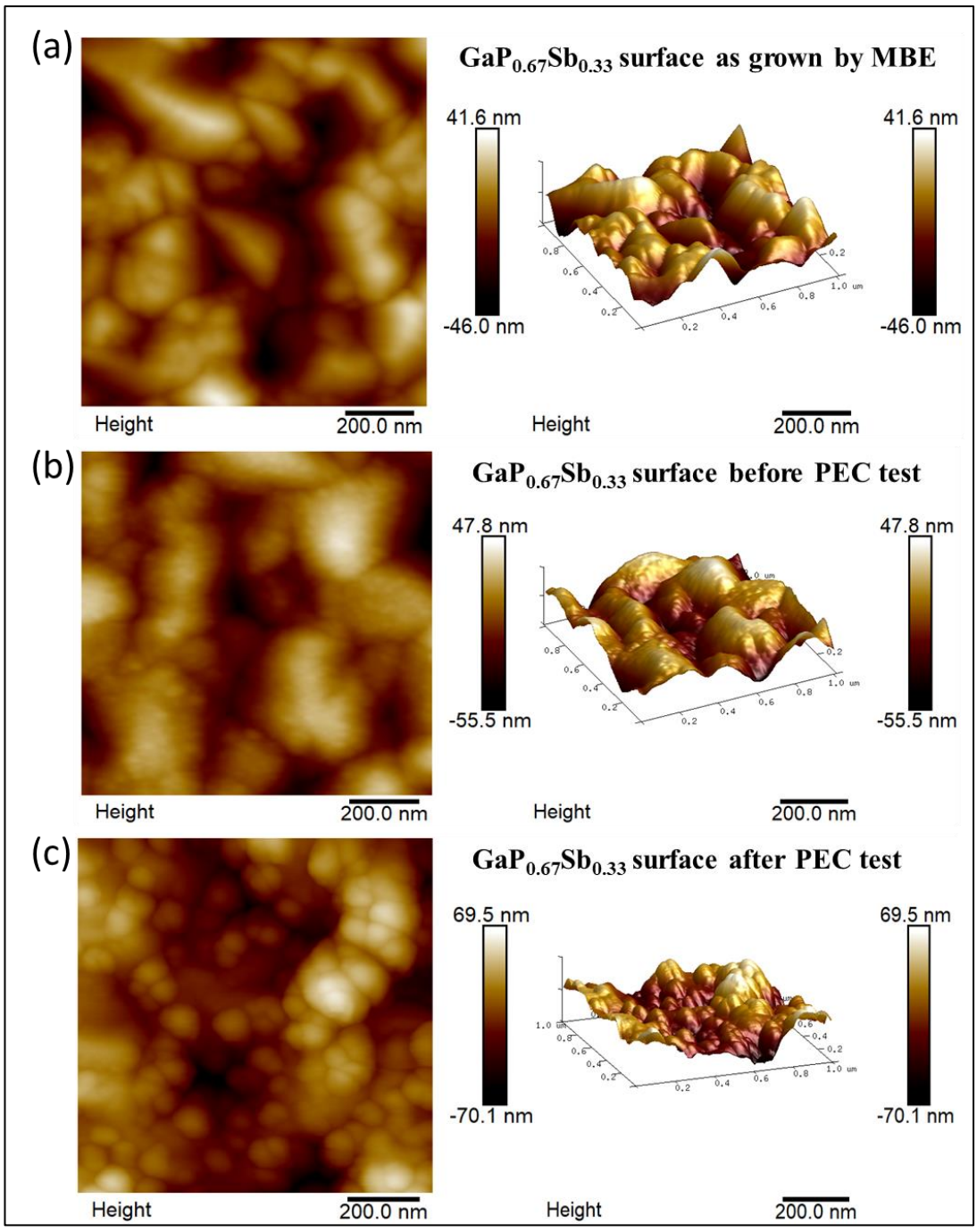

Figure 4.12. Atomic force microscopy (AFM) image morphology of the $GaP_{0.67}Sb_{0.33}$ photoanode before and after stability test. **(a-b)** AFM) image before the PEC test for the $GaP_{0.67}Sb_{0.33}$ photoanode surface coated with TiO_2 (20 nm) and Ni (8 nm). **(c)** AFM image morphology after a 5 h PEC test for the $GaP_{0.67}Sb_{0.33}$ photoanode surface coated with TiO_2 (20 nm) and Ni (8 nm).

4.4. Conclusion

In this chapter, a direct bandgap $GaP_{0.67}Sb_{0.33}$ photoanode has demonstrated, which offers a high absorption coefficient and substantial solar spectrum coverage. The $GaP_{0.67}Sb_{0.33}$ alloy was epitaxially grown on silicon substrates, which are potentially cost-effective for water oxidation compared to their III-V thin film counterparts. Additionally, the reduction of photoelectrode complexity and hence cost by a single semiconductor absorber provides an alternative to expensive technologies, e.g. multijunction PEC cells. The direct growth of 1.65 eV $GaP_{0.67}Sb_{0.33}$ on 1.1 eV Si offers new opportunities for the economic fabrication of the ideal tandem PEC device. More importantly, the alloy with high content of antimony (e.g. $GaP_{0.67}Sb_{0.33}$), reduces the band gap from 2.25 eV to 1.65 eV, however, it increases the absorption spectra and the efficiency for the photoelectrode. Under one-sun simulated solar light irradiation, the $GaP_{0.67}Sb_{0.33}$ photoanode showed a high photocurrent and onset potential in 1.0 M KOH (pH 14) aqueous solution. Furthermore, the photoanode was stable for 5 h without change in the photocurrent density at 1 V versus RHE and a high IPCE; up to 67.1% over the visible range from 400 nm to 650 nm was achieved.

In the following chapter, a nearly dislocation-free multiple quantum well (MQW) InGaN/GaN photoanode for water oxidation has developed. The CoO_x directly deposited onto InGaN/GaN MQW photoanodes exhibited excellent activity and stability in a strongly alkaline electrolyte, 1.0 M NaOH (pH 13.7), for water oxidation up to 28 h, while a reference sample without the catalyst degraded rapidly in the alkaline electrolyte.

Chapter 5: InGaN/GaN Multiple Quantum Well Photoanode Modified with Cobalt Oxide for Water Oxidation

Indium gallium nitride (InGaN) is an attractive semiconductor, with a tunable direct bandgap for photoelectrochemical (PEC) water splitting, but it corrodes in aqueous electrolytes. Cobalt oxide (CoO_x) is a promising co-catalyst to protect photoelectrodes and to accelerate the charge transfer. CoO_x is earth-abundant and stable in extremely alkaline conditions and shows high activity in the oxygen evolution reaction (OER). In this chapter, a high indium content InGaN/GaN multiple quantum wells (MQWs) has presented that can be used for PEC water oxidation. The addition of a CoO_x thin film as a co-catalyst using atomic layer deposition (ALD) has also led to an increase in the photocurrent, incident photon conversion efficiency (IPCE), and extended the life-time stability of the photoelectrode. The growth, optical analysis, and structural quality are evaluated in detail in this chapter. Moreover, the PEC performance for the enhanced photocurrent and extension of stability for an InGaN/GaN MQWs photoanode in 1.0 M NaOH, pH 13.7, is systematically investigated. Additionally, the photostability of the InGaN/GaN MQWs photoanode is studied before and after PEC measurements are taken by XPS and SEM.

5.1. Introduction

Since the burning of petroleum derivatives (coal, gaseous petrol, and oil) represents the majority of carbon emissions, renewable energy sources, for example, solar energy, are viewed as desperately required solutions for energy and the environment (121, 178). PEC water splitting is a promising method to harvest solar energy and can provide clean energy (e.g. hydrogen); it converts sunlight directly to hydrogen by cleaving water molecules (26-28, 116). After the discovery of titanium dioxide (TiO_2)

under ultraviolet radiation for PEC water splitting, research in this field has been led extensively, but critical challenges remain (1, 179). For instance, metal oxides (e.g. TiO_2) are resistant to corrosion but have a lower visible light absorption efficiency and slow charge transport kinetics, which are limitations to achieving high solar-to-hydrogen conversion efficiency (1, 147). On the other hand, PEC electrodes, based on III-V semiconductors used for water oxidation, exhibited high performance owing to their excellent optical properties in the visible region of the electromagnetic spectrum, but they are thermodynamically unstable and corrode rapidly in aqueous electrolytes (10, 11, 13, 22, 67, 68, 103).

Therefore, efficient and stable photoanodes are crucial to accomplishing long-term economic hydrogen production by PEC water splitting due to the shortage of stable oxygen evolution reaction (OER) catalysts (180). Group III-nitride semiconductors, for example, indium gallium nitride (InGaN), have recently become promising candidates for PEC water splitting because they have a tunable direct band gap from the ultraviolet to the near-infrared range covering the entire solar spectrum (91, 93, 181). Additionally, they are widely used in optoelectronic and electronic applications (97, 182). Moreover, their conduction and valence band edges straddle the hydrogen reduction (H^+/H_2) and water oxidation (H_2O/O_2) potentials (93). In recent years, extensive studies have investigated InGaN and GaN photoelectrodes but with limited success (78, 80, 94, 98-101, 183-197). For instance, a InGaN nanowires photoanode modified with a iridium oxide (IrO_2) co-catalyst exhibited a high photocurrent density under illumination but corroded rapidly in solution (95). Very recently, Co_3O_4 nano-islands were shown to reduce the onset potential and improve the stability of a GaN NW photoanode (102). However, the nano-islands led to an incomplete coverage of the catalyst over the GaN surface and hence limited stability in a strongly alkaline

electrolyte. The Co-Pi-modified GaN photoaonde has shown some improvement in the onset potential and photocurrent but poor resistance against photocorrosion (100). Additionally, it is commonly known that high-crystal-quality epilayer InGaN with large indium content is difficult to grow, due to the large lattice mismatch between InGaN and its template (97, 98, 182, 198). One solution to relax such a strain is to adopt one-dimensional materials, such as nanorods. Despite numerous advantages of one-dimensional materials in relaxing strain, enhancing photon absorption, and facilitating charge transport, the co-existence of different crystal phases and surface states of a large surface-to-volume ratio structure causes high non-radiative recombination rates. An alternative to tackle the strain is to implement InGaN/GaN MQWs, which can lead to an extended solar absorption spectrum and reduction in the non-radiative recombination (97, 198). Despite their decent performance in halogen splitting, the solar-to-hydrogen (STH) conversion efficiencies of conventional InGaN/GaN MQWs are quite trivial when engaged in water oxidation (99, 184, 185, 187, 190). That is, the relatively high defect densities severely limit the InGaN-based photoelectrode performance (179). The low crystalline quality of In-rich InGaN alloys is considered one of the primary confronting issues for metal-nitride devices in general (97, 182, 198). To overcome these limitations, InGaN/GaN MQWs with suitable surface modification may be adopted to achieve stable and efficient PEC water splitting.

In this chapter, a nearly dislocation-free and high-quality InGaN/GaN MQW photoanode modified with CoO_x is presented. The surface coating improved the photocurrent due to reduced overpotential, resulting in a stable photocurrent of the InGaN/GaN MQW photoanode in an alkaline electrolyte (1.0 M NaOH, pH 13.7) for up to 28 h. Moreover, the InGaN/GaN MQW photoanode modified with CoO_x

produced a low onset potential of -0.03 V and a high photocurrent density of 1.26 mA cm^{-2} versus RHE while the InGaN/GaN MQWs without any co-catalyst showed a reduced photocurrent of 0.94 mA cm^{-2} and onset potential of 0.01 V at potential 1.23 V versus RHE, respectively. Electrochemical impedance spectroscopy confirmed that the coupling of CoO_x onto InGaN/GaN MQWs reduced the electrochemical reaction resistance to some extent and thus enhanced the stability of InGaN/GaN MQWs for water oxidation.

5.2. Experimental Methods

Atomic layer deposition: ALD was performed in a home-made closed chamber-type ALD reactor at 250 ^oC, using ultrahigh purity N_2 (99.999%) carrier gas at a flow rate of 50 sccm and a pressure of 60 Pa. The CoO_x layer (12 ~ 13 nm) was deposited onto the surface of InGaN/GaN MQWs by sequential exposure of the cobaltocene ($CoCp_2$, 75 ^oC) and O_3 with 350 cycles.(149, 199) The pulse, exposure, and purge times were 5 s, 8 s, and 20 s for $CoCp_2$, and 0.1 s, 8 s, and 20 s for O_3, respectively.

Materials characterization: The high-resolution TEM (HRTEM) images and EELS spectra were obtained using a FEI Titan 80-300 KV microscope assembled with a spherical aberration corrector of the imaging lens, a monochromator, and a high-resolution spectrometer (Gatan Image Filter Tridiem 965). The microscope was operated at 80 kV, and the spectra were collected in STEM mode, which used the spectrum imaging technique with 0.1 eV per channel dispersion of the spectrometer. The TEM sample was prepared by a Zeiss NVision 40 dual beam, focused ion beam/scanning electron microscope (FIB/SEM), and then the sample was sealed in a vacuum transfer holder (Gatan Model 648) for further TEM characterization and electron energy loss spectroscopy (EELS) analysis. The XRD measurement was

performed by a Jordan Valley D1 X-ray diffraction instrument. Scanning electron microscope (SEM) analysis was carried out using a Hitachi S-4800 SEM at 3 kV accelerating voltage. X-ray photoelectron spectroscopy (XPS) measurements were performed with a Thermo monochromated aluminium k-alfa photoelectron spectrometer, using monochromic Al-Kα radiation (1486.7 eV). Survey scans were collected in the range of 0–1300 eV. The area underneath these bands is an indication of the concentration of element within the region of analysis (spot size 400 μm). Data was analysed with CasaXPS software. Raman measurements were carried out in a Renishaw inVia micro-Raman system by 1800 g mm^{-2} grating through a ×50 objective lens and using a 532 nm excitation laser. The laser power was controlled at about 10%.

Device fabrication: Before the PEC experiments, a window for contact was patterned by a typical lithography process and then was etched down to the GaN template by reactive ion etching. A metal of Ti/Au for ohmic contact was deposited on the GaN template with a thickness of 35 and 500 nm, respectively. Rapid thermal annealing (RTA) was performed at a temperature of 850 °C for 30 s. Then, the sample was attached by a copper wire using silver paste and covered by insulating epoxy.

Photoelectrochemical measurements: A 200 W Xe arc lamp (66477-200HXF-R1 Mercury-Xenon) was used as a light source with an AM 1.5 G filter to produce simulated sunlight. The illumination intensity was calibrated using a silicon reference cell with a power meter (Thorlabs, Model PM100A). Before the PEC experiments, the electrolyte was purged by Ar for 30 min. PEC measurements were performed in a three-electrode configuration using photoanodes as the working electrode, silver/silver chloride (Ag/AgCl) as the reference electrode, and platinum coil as the counter electrode in 1 M NaOH pH ~ 13.7 in a single-compartment PEC cell with a quartz

window. The measured potentials versus Ag/AgCl were converted into the reversible hydrogen electrode (RHE) scale using the following Nernst equation:

$$V_{RHE} = V_{Ag/AgCl} + 0.059 \times PH + V^{0}_{Ag/AgCl}$$

Where $V_{Ag/AgCl}$ the potential is experimentally measured versus the Ag/AgCl reference electrode, and $V^{0}_{Ag/AgCl}$ is the standard potential of Ag/AgCl at 25 °C (0.1976 V versus RHE). All linear sweep voltammetry measurements with a scan rate of 50 mV s^{-1} were performed under both dark and illumination conditions using a potentiostat (Ivium CompactStat).

The IPCE values for the InGaN/GaN photoanode were performed by measuring the current density under a 150 W xenon lamp (Newport) utilizing various band-pass filters. The IPCE measurement was also performed using a three-electrode configuration in 1 M NaOH. Throughout the measurements, the scan rate used was 50 mV s^{-1} scanning from negative to positive potential. The photocurrent was obtained by subtracting the dark current density from the measured current density under light at various wavelengths. The IPCE can then be computed by using the following equation:

$$\mathrm{IPCE} = \frac{1239.8\ (V\ nm)\times\left[\ J\ (mAcm^{-2})\ \right]}{P_{mono}\ (mW\ cm^{-2})\times\lambda\ (nm)}$$

Where J is the photocurrent density, P_{mono} is the monochromated illumination power intensity, and λ the wavelength. The photocurrent was obtained by subtracting the dark current from the light current.

5.3. Results and Discussion

5.3.1. Growth of InGaN/GaN MQWs by MOCVD

The widely common technique for growing III-Nitride semiconductors inclusive of AlN, GaN, InN, and their ternary and quaternary alloys is the metal-organic chemical vapor deposition (MOCVD). The common precursors are Trimethylgallium (TMGa), Triethylgallium, Trimethylindium (TMIn), and ammonia (NH_3) to introduce metal into the MOCVD reactor. The carrier gases such as H_2 and N_2 are used to transport the precursors into the chamber. In principle of MOCVD is to realize the contact between volatile compound material and the substrate heated under vacuum. The III-Nitride precursors are transported onto the chamber using the carrier gas and adsorbed on the substrate surface. The reactive species thus diffuse at the substrate surface to preferential sites and react in heterogeneous phase to give rise to the formation of the film. A high-quality InGaN/GaN MQWs photoanode for PEC water splitting was grown heteroepitaxially by atmospheric pressure metal organic chemical vapour deposition (MOCVD) on (0001) patterned sapphire substrates (PSS). Due to the lack of native substrates and the large polarization effect, conventional III-nitride planar heterostructures generally exhibit very high defect densities, which therefore severely limit the devices' performance and stability, particularly in aqueous solution. More importantly, the large lattice mismatch between InGaN and GaN makes the growth of thick InGaN with high Indium content very challenging. Using a thick GaN template above the substrate and implementing InGaN/GaN multiple MQWs in the active region are two techniques to surpass the two aforementioned obstacles. Nevertheless, growth temperature incompatibility between InGaN and GaN gives rise to a major difficulty.

The growth conditions of the samples in this study were optimized to surpass some of the abovementioned issues. The structure of the InGaN/GaN MQWs presented here were grown heteroepitaxially by atmospheric pressure metal organic chemical vapour deposition (MOCVD) on (0001) patterned sapphire substrates (PSS). Since there is a lattice mismatch of 13.9% between GaN and sapphire, an unintentionally doped (UID) GaN buffer template of 3.5 μm was grown at 1200 °C. Afterwards, the active region consisting of an undoped eight-period multiple-quantum well (MQW) was then grown. The thickness of the $In_xGa_{1-x}N$ wells was 2.6 nm with ~ 24% indium content. Each well was followed immediately by the growth of a low-temperature (LT) GaN barrier layer. The growth temperature of the InGaN/GaN QW/barrier was 805 °C. Finally, a high-temperature (HT) GaN cap was grown by ramping up the temperature 100 °C higher than the previous temperature. The thickness of the HT GaN cap was about 9 nm. The growth rates of the InGaN QW, LT GaN barrier and HT GaN cap layers were 1 Å/sec, 0.5 Å/sec, and 0.35 Å/sec, respectively. The detailed conditions of the growth in this study is presented in Table 5.1.

Table 5.1. Details of the MOCVD growth conditions.

Layer	TMI (sccm)	TEG (sccm)	NH3 (slm)	Carrier gas (slm)	Temperature (°C)
InGaN QW	90	35	5	2	805
LT GaN barrier	0	20	3.2	3.8	805
HT GaN barrier	0	12	3.2	3.8	905

5.3.2. InGaN/GaN MQWs Photoanode Modified by Cobalt Oxide Co-catalyst

A suitably highly active co-catalyst for the oxygen evolution reaction (OER) was required to stabilize the photoelectrode in high pH solution and promote charge transfer. Earth-abundant cobalt oxide (CoO_x) was chosen as the OER co-catalyst for the InGaN/GaN MQWs photoanode. The CoO_x catalyst has excellent hole conduction and electron blocking properties due to its high-conduction edge position, particularly under strongly alkaline conditions (8, 9, 21, 71, 149, 199-212). The CoO_x catalyst was directly deposited onto the surface of the InGaN/GaN MQWs using atomic layer deposition (ALD) and has been shown to enhance the stability of photoanodes (203, 207). A schematic illustration of the InGaN/GaN MQWs photoanode electrode modified by CoO_x is shown in Figure 5.1. When the light radiates on the InGaN/GaN MQWs, an electron–hole pair will be formed in both wells and barriers. The internal electrical field within the active region is illustrated by the band diagram in Figure 5.1(a). Eight stacks of InGaN/GaN MQWs epitaxially grown on (0001) sapphire substrates were employed for photoanodic water splitting. InGaN/GaN MQWs allow additional photon absorption in the visible region.

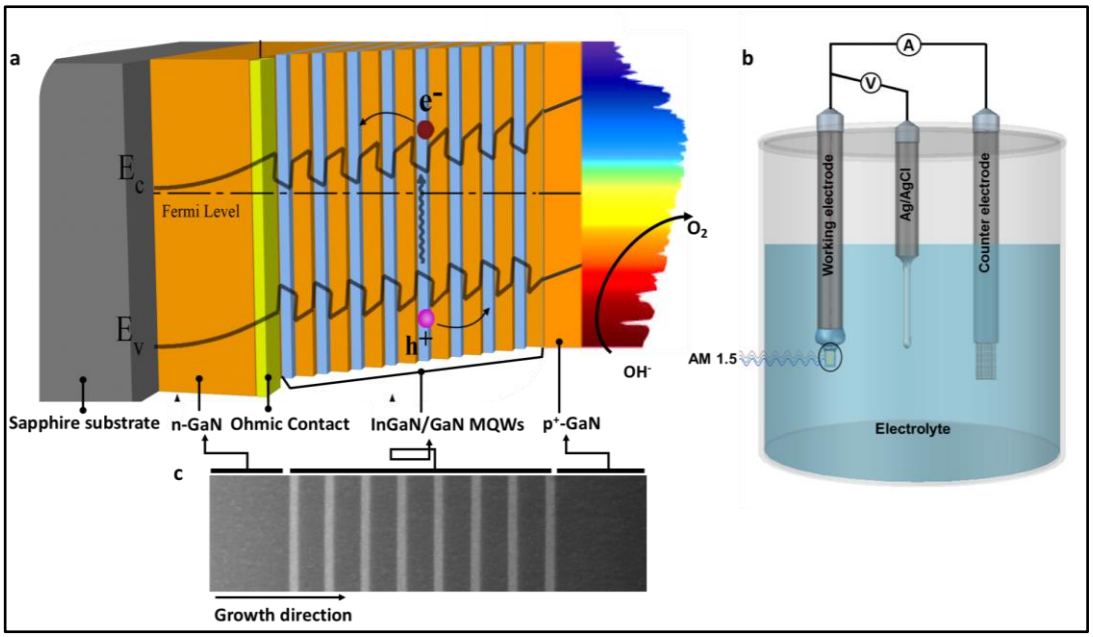

Figure 5.1. Schematic diagram of the main processes for illustrating the carrier transport mechanisms of the InGaN/GaN MQWs photoanode and PEC setup for water splitting. **(a)** Schematic diagram of the InGaN/GaN multiple quantum well (MQW) photoanode structure grown by MOCVD on (0001) patterned sapphire substrates (PSS) and then by a 3.5 μm GaN buffer followed by the active region consisting of undoped eight-period MQWs. The schematic illustration shows the general concept of a single photoelectrode under an AM 1.5G illumination; incoming photons (hv) generate electrons (e^-) and holes (h^+) pairs in the active region where they will be separated by internal electric field. The holes move towards the semiconductor/electrolyte interface to drive the OER and the electrons are moved towards the rear ohmic contact and through an electrical connection to the surface of the counter electrode to drive the HER. **(b)** Schematic diagram of the experimental setup used for the photoelectrochemical measurements, which consists of the working electrode (InGaN/GaN MQWs), reference electrode (Ag/AgCI), and counter electrode (platinum coil). **(c)** The TEM cross-section shows the InGaN/GaN MQWs photoanode and its growth direction.

5.3.3. Structural Characterization of the InGaN/GaN MQWs Photoanode

The structural properties of the InGaN/GaN MQWs were analysed by scanning transmission electron microscopy (STEM). The low-magnification STEM images in Figure 5.2 and 5.3 show that the active region is virtually free of any dislocations. Figure 5.3 shows high-resolution STEM images of the eight quantum wells (QWs), which unambiguously show defect-free single crystalline epilayers. A lattice constant of about 0.52 nm was measured for both InGaN wells (~3 nm) and GaN barriers (~10 nm), indicating coherent strained InGaN QWs on the GaN (0001) surface. Each QW shows a sharp contrast between wells and barriers, indicating high interface quality with marginal intermixing. No interfacial dislocations or misfits can be observed, although a high indium composition of about 20% was introduced in the wells. The crystal quality plays a critical role in the STH conversion efficiency of PEC cells because material imperfections are a major contribution to non-radiative recombination and are detrimental to photo-excited carriers for H_2 and O_2 evolution reactions. Although one-dimensional nanomaterials are capable of accommodating materials of large lattice mismatches, it has been shown that various types of dislocations, e.g. stacking faults, as well as a high density of surface states, largely undermine the performance of nanowire or nanorod devices (213-215). Therefore, defect-free MQWs may serve as a good alternative to one-dimensional nanostructures for high indium content InGaN and associated device applications.

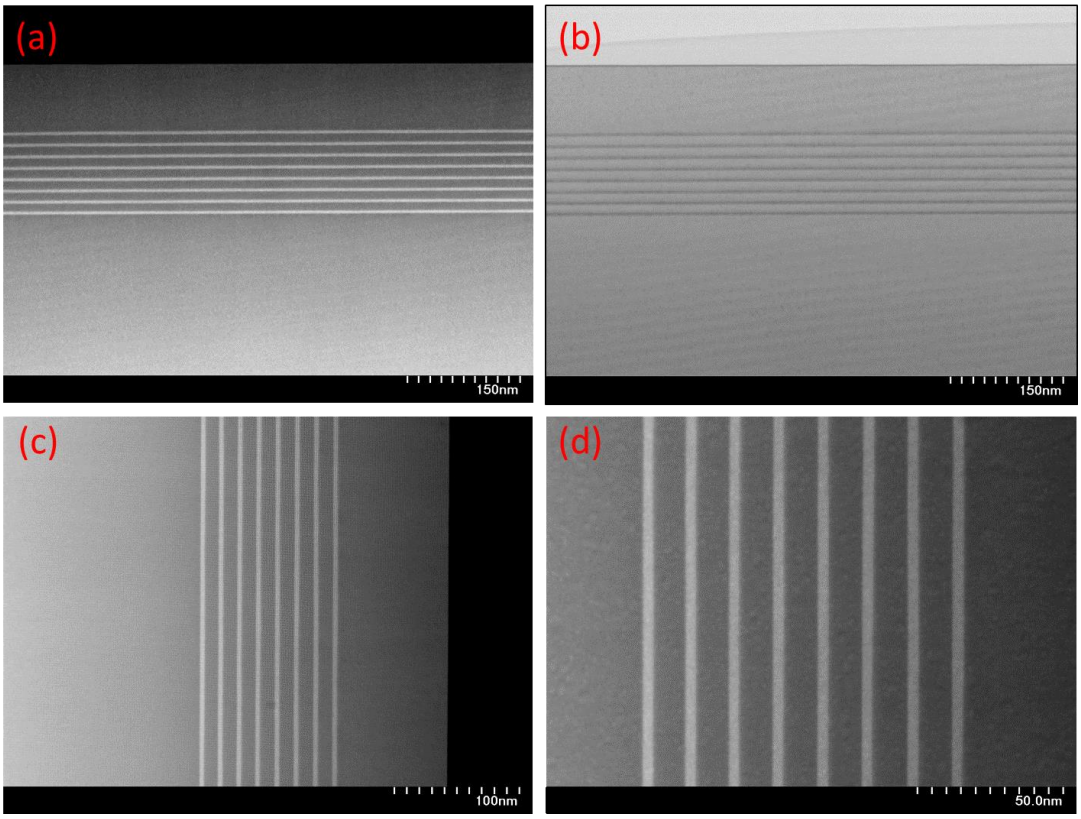

Figure 5.2. The high-angle annular dark-field scanning STEM (HAADF-STEM) and high-angle annular bright-field (ABF-STEM) images for the InGaN/GaN MQWs photoanode. **(a)** (HAADF-STEM) image of the InGaN/GaN MQWs photoanode. **(b)** (ABF-STEM) image of the InGaN/GaN MQWs photoanode. **(c-d)** (HAADF-STEM) image of the InGaN/GaN MQWs photoanode at a different scale.

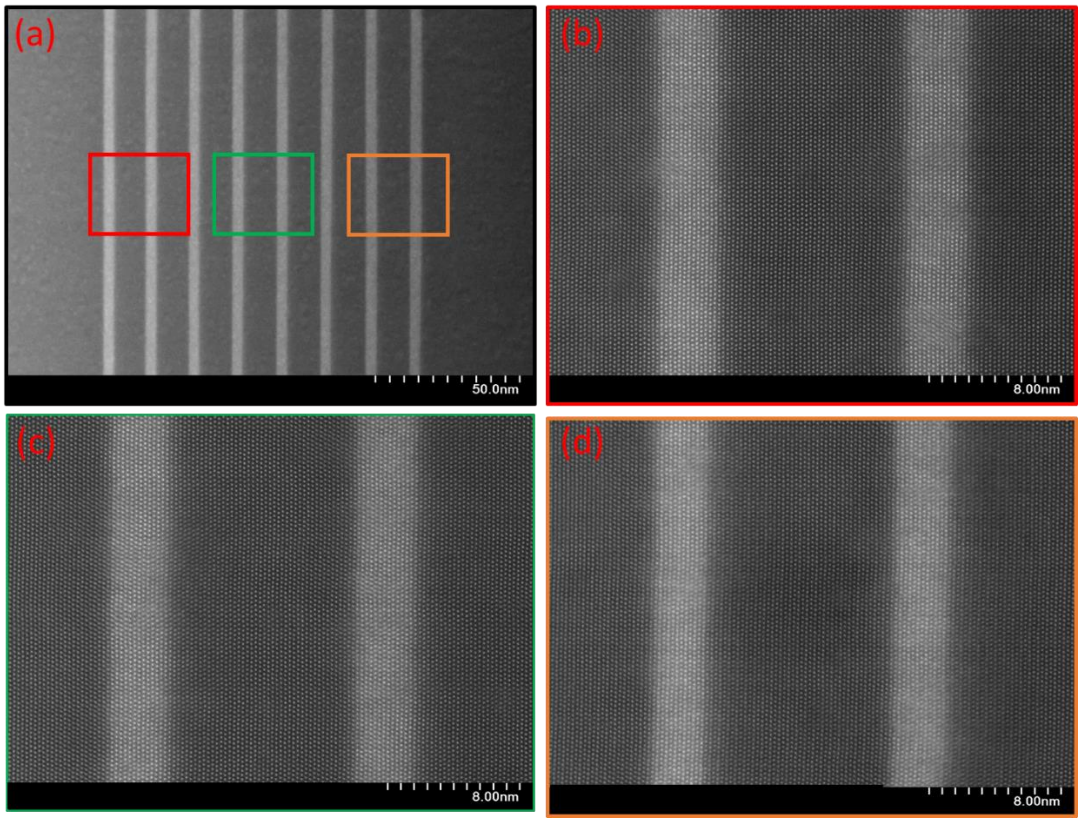

Figure 5.3. Structural characterization of the InGaN/GaN MQWs photoanode. **(a)** High-resolution STEM images of the InGaN/GaN MQWs photoanode which show that the structure is virtually free of any dislocations. **(b-d)** STEM images of eight quantum wells showing defect-free single crystalline epilayers.

STEM energy-dispersive X-ray spectroscopy (EDS) measurements were carried out to extract the indium content in the QWs. An EDS line scan across the QWs showed that they were highly uniform in indium composition, with all showing a uniform indium composition of around 20% or an atomic percentage of 10%, as shown in Figure 5.4. The EDS elemental mapping also provides evidence of the composition uniformity of InGaN QWs, as shown in Figure 5.5.

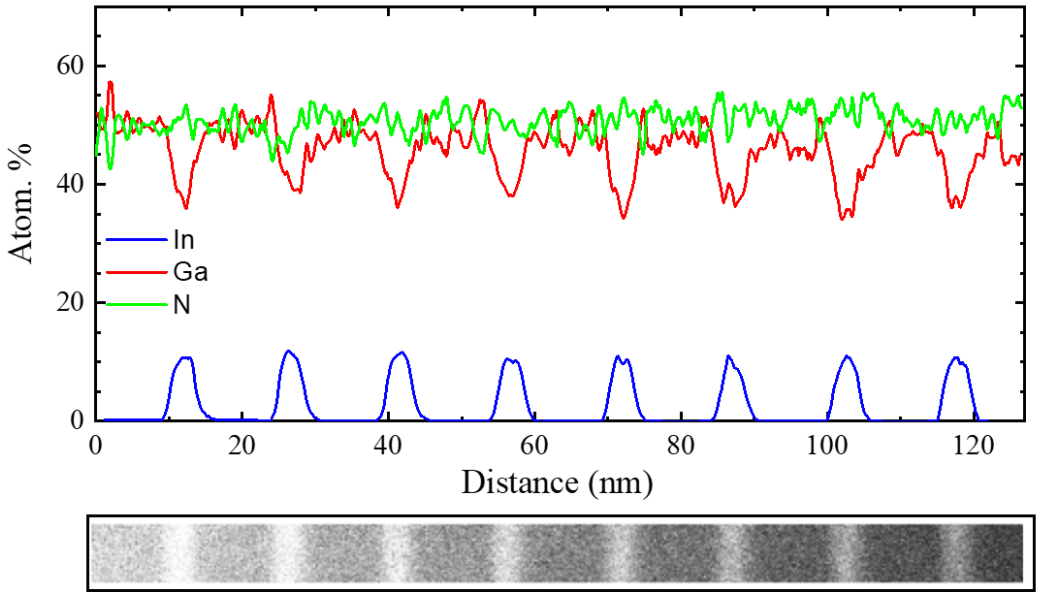

Figure 5.4. Characterization of the InGaN/GaN MQW_S photoanode. The In (blue line), N (green line), and Ga (red line) concentration depth profiles for the InGaN/GaN MQW photoanode using STEM energy-dispersive X-ray spectroscopy (EDS) measurements.

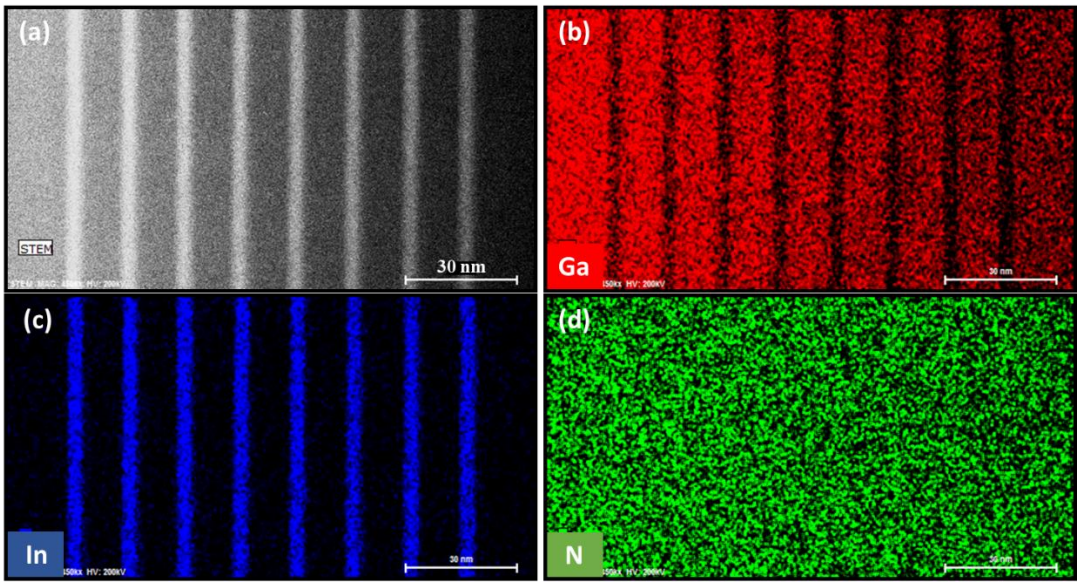

Figure 5.5. STEM energy-dispersive X-ray spectroscopy (EDS) measurements. **(a-d)** EDS elemental mapping for the InGaN/GaN MQWs photoanode showing a good composition uniformity of InGaN MQWs.

To further investigate the material properties of InGaN/GaN MQWs, X-ray diffraction (XRD) was performed; the XRD pattern of the MQWs is shown in Figure 5.6(a). The diffraction peak at zero arc-sec corresponds to the GaN (0002) plane. The XRD pattern from the ω-2θ scan exhibits distinct satellite peaks, indicating high interfacial quality between the InGaN QWs and GaN barriers. The period thickness of InGaN QWs and the GaN barrier is measured at 12.8 nm, which is consistent with the STEM measurements. The optical properties of the InGaN/GaN MQWs were further studied using photoluminescence (PL) spectroscopy, as shown in Figure 5.6(b). The PL emission peak takes place at ~ 519 nm, which corresponds to the emission from the InGaN QWs.

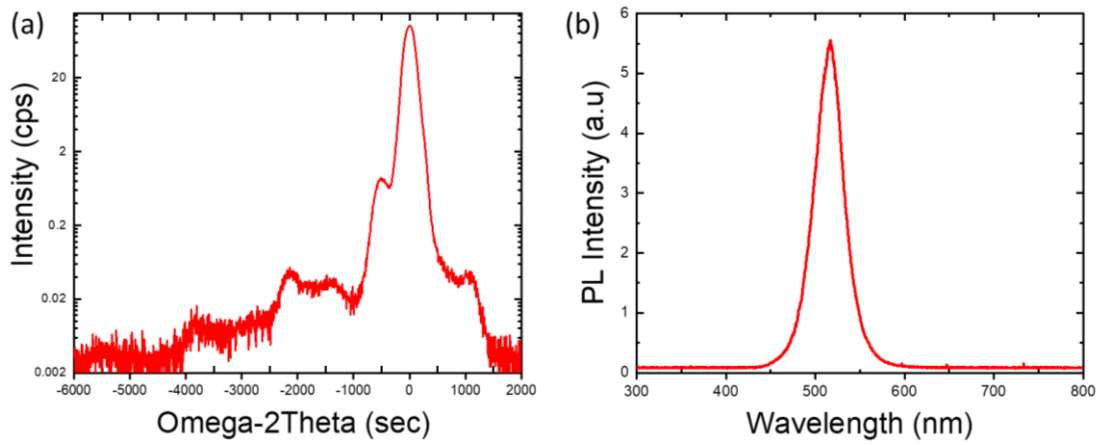

Figure 5.6. X-ray diffraction (XRD) and photoluminescence spectra for the InGaN/GaN MQWs photoanode. **(a)** X-ray diffraction (XRD) (0002) $\omega/2\theta$ scan measurements of the InGaN/GaN MQWs photoanode. **(b)** PL spectra of the InGaN/GaN MQWs photoanode at room temperature.

Furthermore, STEM energy-dispersive X-ray spectroscopy (EDS) measurements for the CoO_x layer (~ 13 nm) on the top of the p-type GaN layer are shown in Figure 5.7(a-b). It shows a highly dense layer composed of only Co and O, shown in orange and magenta colours, respectively. EDS elemental mapping for the CoO_x catalyst shows a good composition uniformity of the CoO_x film, as shown in Figure 5.7(b). This CoO_x layer covers the surface of the InGaN/GaN MQWs photoanode well and can prevent the photoanode from making direct contact with the electrolyte.

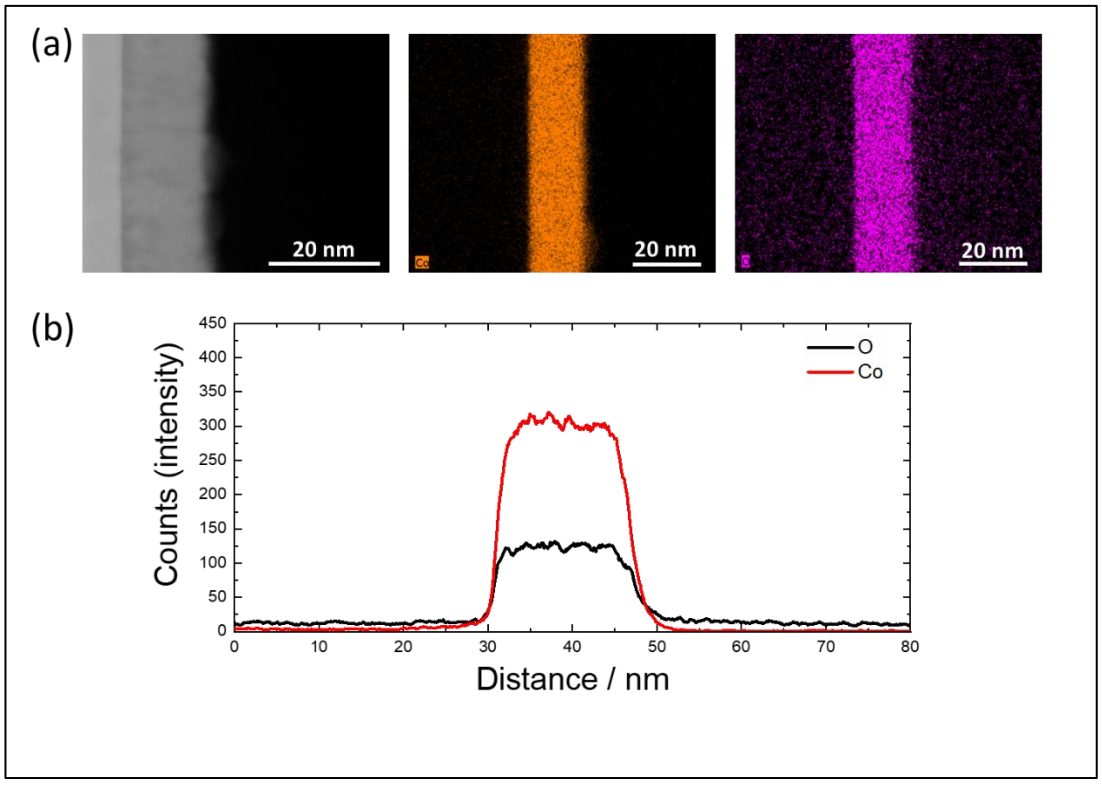

Figure 5.7. STEM energy-dispersive X-ray spectroscopy (EDS) measurements for cobalt oxide thin film co-catalyst. **(a-b)** STEM image of a thin-layer CoO_x co-catalyst on the surface of the InGaN/GaN MQWs photoanode and EDS elemental mapping showing the CoO_x thin layer to be composed of only Co (orange) and O (magenta).

To further confirm the surface structure, Raman measurements were carried out using a Renishaw inVia micro-Raman system, with a laser line of 532 nm, as shown in Figure 5.8. The Raman spectrum of InGaN/GaN MQWs, with an E2 phonon mode of GaN at ≈ 568 cm^{-1}, and the A1 longitudinal optical (LO) phonon mode at ≈ 734 cm^{-1}, was clearly observed, confirming the surface layer of GaN, as shown in Figure 5.8(a). These observed modes are in agreement with reported values (216). The Raman spectrum of InGaN/GaN MQWs-CoO_x shows both modes of GaN E2 and A1(LO) being observed, at 568 cm^{-1} and 733 cm^{-1}, respectively, and another peak at ≈ 688 cm^{-1}, which is attributed to the CoO_x phonons mode; this helps to confirm the presence of CoO_x in the top layer, as shown in Figure 5.8(b).

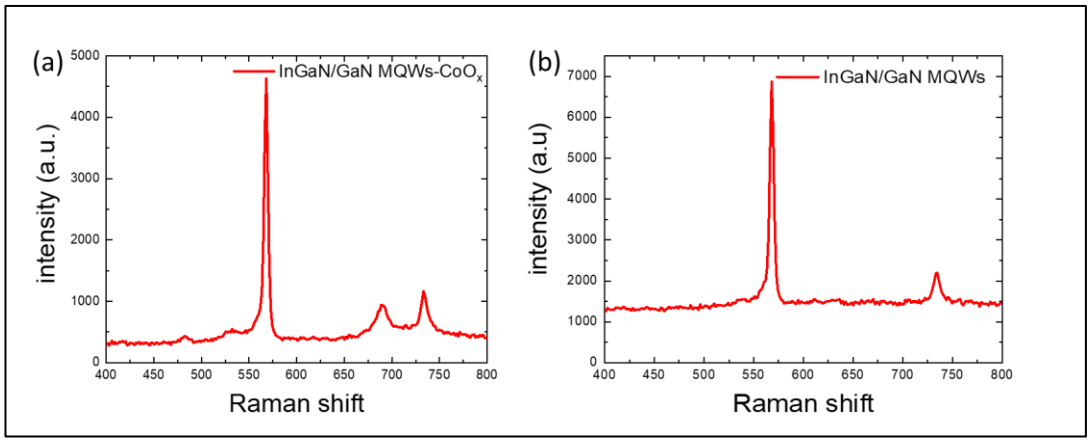

Figure 5.8. Raman measurements for InGaN/GaN MQWs photoanodes. (a) Raman spectra of InGaN/GaN MQW-CoO_x photoanode. **(b)** InGaN/GaN MQW photoanode. The Raman spectrum were carried out in a Renishaw inVia micro-Raman system with 1800 g mm^{-2} grating using a 532 nm excitation laser through a ×50 objective lens.

5.3.4. Photoelectrochemical Performance of the InGaN/GaN MQWs Photoanode

The PEC performance of the InGaN/GaN MQWs photoanodes was investigated using a standard three-electrode potentiostatic configuration, including a silver–silver chloride (Ag/AgCl) reference electrode, a Pt coil counter electrode, and a working electrode in 1 M NaOH electrolyte (pH ~13.7) under one-sun illumination. The photocurrent density–voltage (*J–V*) characteristics are shown in Figure 5.9(a) for the bare InGaN/GaN MQW and InGaN/GaN MQW modified with CoO_x. As shown in Figure 5.9(a), the saturated photocurrent of the InGaN/GaN MQW electrode reached ~ 0.95 mA cm^{-2} at a potential of 1.23 V versus the reversible hydrogen evolution (RHE). A significant improvement in photocurrent was obtained by using the CoO_x as co-catalyst; the saturated photocurrent increased to around 1.26 mA cm^{-2} at a potential of 1.23 V versus RHE. Moreover, the onset potentials for the InGaN/GaN MQW and InGaN/GaN MQW modified with CoO_x were 0.01 V and -0.03 V, respectively. The significant anodic shift can be attributed to improved carrier extraction/collection efficiency and enhanced charge carrier transport at the semiconductor/electrolyte interface when using the CoO_x catalyst (21, 102, 203, 207).

To further investigate the wavelength-dependent photoelectrochemical contribution of the GaN and InGaN layers to the photocurrent, the incident-photon-to-current conversion efficiency (IPCE) was measured at 1.23 V versus RHE. As shown in Figure 5.9(b), an IPCE of InGaN/GaN MQW-CoO_x at 380 nm is 16.8%, which is higher than the value of the bare InGaN/GaN MQW photoanode (~ 10.3% at 380 nm). The IPCE measurement is consistent with the (*J–V*) measurements. The improved IPCE value also indicates efficient carrier separation and collection, or fast charge transfer to the semiconductor/electrolyte interface while using CoO_x as co-catalyst. By

using the InGaN/GaN MQWs, the IPCE spectra extend to the visible region up to 500 nm, which is in good agreement with the absorption of the QWs. Due to the relatively low absorption from QWs, the IPCE can be further improved by using light trapping techniques. Fabrication of InGaN/GaN MQWs with a high indium content is also important in visible light-driven water splitting.

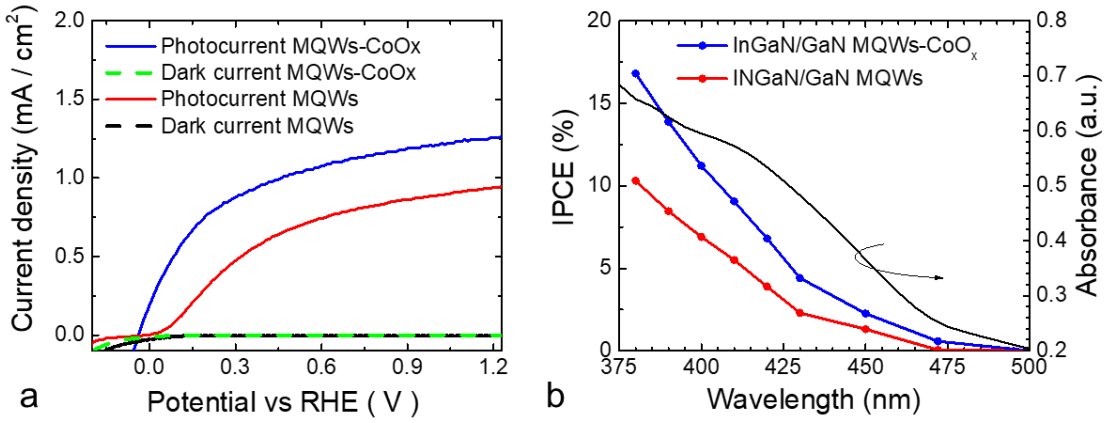

Figure 5.9. Photoelectrochemical performance of InGaN/GaN MQWs photoanodes. **(a)** Photocurrent density–potential (*J*–*V*) curves (scan rate is 50 mV s^{-1}) in 1 M NaOH electrolyte under one-sun illumination versus RHE (V). **(b)** Incident photon-to-current conversion efficiency (IPCE) of InGaN/GaN MQWs and InGaN/GaN MQWs-CoO_x photoanodes in 1 M NaOH electrolyte at 1.23 V versus RHE. The absorbance of the MQWs is plotted as a black curve in (b).

To obtain further insight into the charge transfer performance at the semiconductor/electrolyte interface, electrochemical impedance spectra (EIS) measurements were taken using a standard three-electrode configuration in 1 M NaOH electrolyte (pH ~13.7) under dark conditions. The EIS measurement was obtained in the range of $10\ \text{kHz} - 3\ \text{MHz}$ at an amplitude of $10\ \text{mV}$ and with the equivalent circuit model that was used to fit the EIS data, as shown in Figure 5.10(a-b). As shown in Figure 5.10, the InGaN/GaN MQWs-CoO_x photoanode shows a lower charge transfer resistance and higher conductivity compared to the bare InGaN/GaN MQW photoanode without catalyst, which confirms the improved charge transfer by using a high catalytic OER catalyst CoO_x.

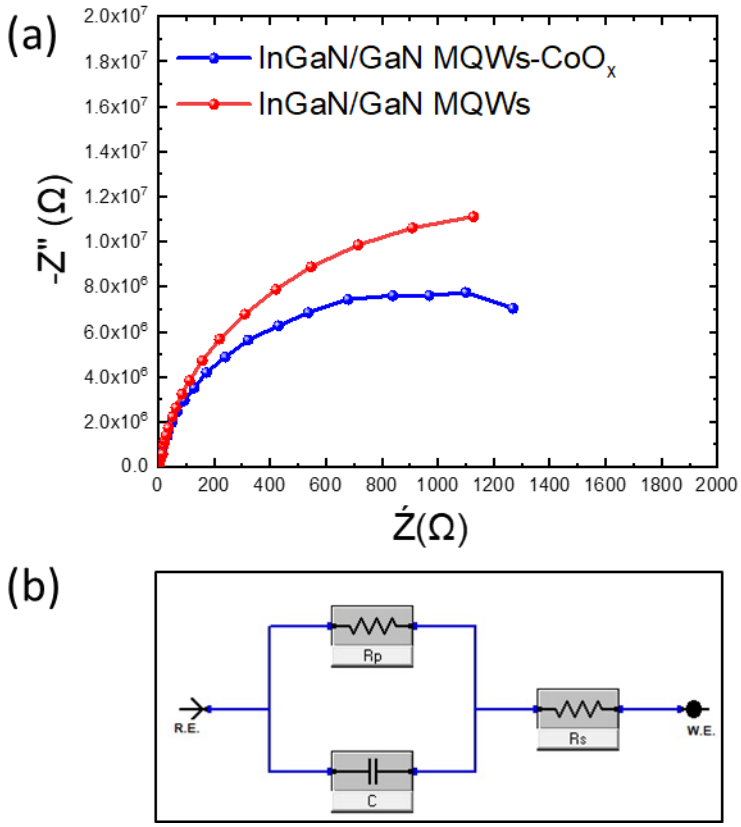

Figure 5.10. Electrochemical impedance spectra (EIS) measurements for both InGaN/GaN MQWs photoanodes. **(a)** Nyquist plots of InGaN/GaN MQWs and InGaN/GaN MQWs-CoO_x photoanodes under dark conditions in 1 M NaOH with a perturbation amplitude of 10 V and frequency range from 10 kHz to 3 MHz. **(b)** The equivalent circuit models.

5.3.5. Stability Evaluation of the InGaN/GaN MQWs Photoanode

Photoelectrode stability is an essential requirement and an outstanding challenge for PEC cells. The photocurrent density–time (*J*–*t*) characteristics of InGaN/GaN MQWs photoanodes were investigated for 28 h under zero bias vs. Pt counter electrode in a corrosive solution of 1M NaOH electrolyte (pH ~13.7), as shown in Figure 5.11(a-b). The photocurrent of the bare InGaN/GaN MQWs photoanode decreased rapidly at the beginning, which was attributed to significant photocorrosion. On the other hand, the InGaN/GaN MQWs photoanode modified by CoO_x shows that the photocurrent has been sustained over an extended reaction duration (> 21 h). While the photocurrent of the bare InGaN/GaN MQWs photoanode was degraded to around 0 mA cm^{-2} after only 40 min of experiment, the photocurrent of the InGaN/GaN MQWs modified with CoO_x was not degraded until extensive PEC reaction (~ 28 h). The initial increase in photocurrent density over the first couple of hours may be due to gradual activation of the CoO_x co-catalysts. Clearly, the catalyst can enhance the stability of the InGaN/GaN MQWs photoanode. As both photoanodes have the same structures, such an improvement is attributed to the high catalytic OER catalyst.

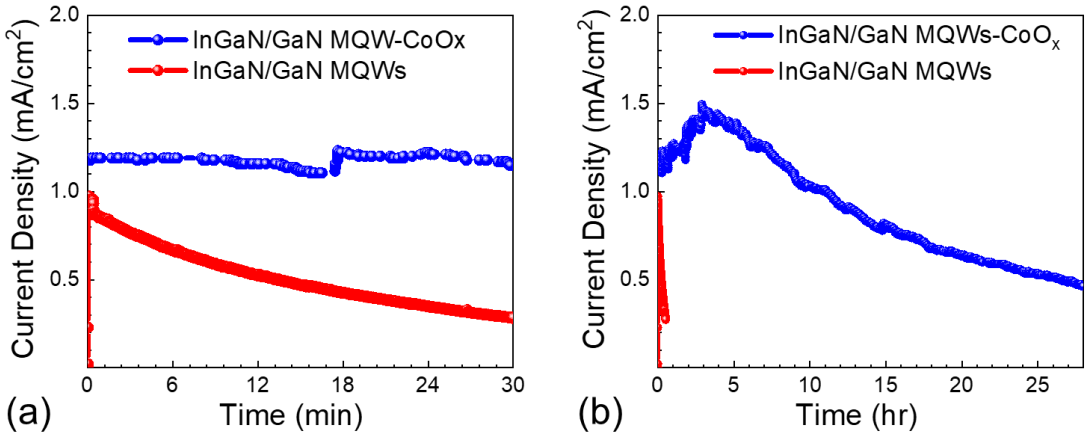

Figure 5.11. Stability evaluation for both InGaN/GaN MQWs photoanodes. **(a)** Current density versus time (*J*–*t*) of both InGaN/GaN MQW photoanodes at zero bias in 1M NaOH (pH 13.7) versus Pt counter electrode under simulated sunlight using AM1.5G filter over a short-term period (30 min). **(b)** Long-term performance of InGaN/GaN MQWs and InGaN/GaN MQWs-CoO_x photoanodes over 28 hours.

To compare the degree of photocorrosion of the two photoanodes, the bare InGaN/GaN MQW after 2 h of reaction and the modified-CoO_x InGaN/GaN MQWs after 28 h of reaction, the surface morphology of the photoanodes after reaction was studied by scanning electron microscopy (SEM) and X-ray photoelectron spectroscopy (XPS). Figure 5.12(a-d) shows the SEM images of the surfaces of the InGaN/GaN MQW-CoO_x and the bare InGaN/GaN MQW photoelectrodes after the stability test. Both photoanodes showed different degrees of photocorrosion. The InGaN/GaN MQW-CoO_x photoanode showed a smooth and pinhole-free surface before PEC, as shown in Figure 5.12(a), and after PEC this protective layer was still visible, with only small areas of the film showing the ordered surface textures caused by PEC corrosion of the nitride layers. By contrast, the entire surface of the bare InGaN/GaN MQW photoanode showed surface textures due to PEC etching, indicating that the photoelectrode was severely corroded, as shown in Figure 5.12(c-d).

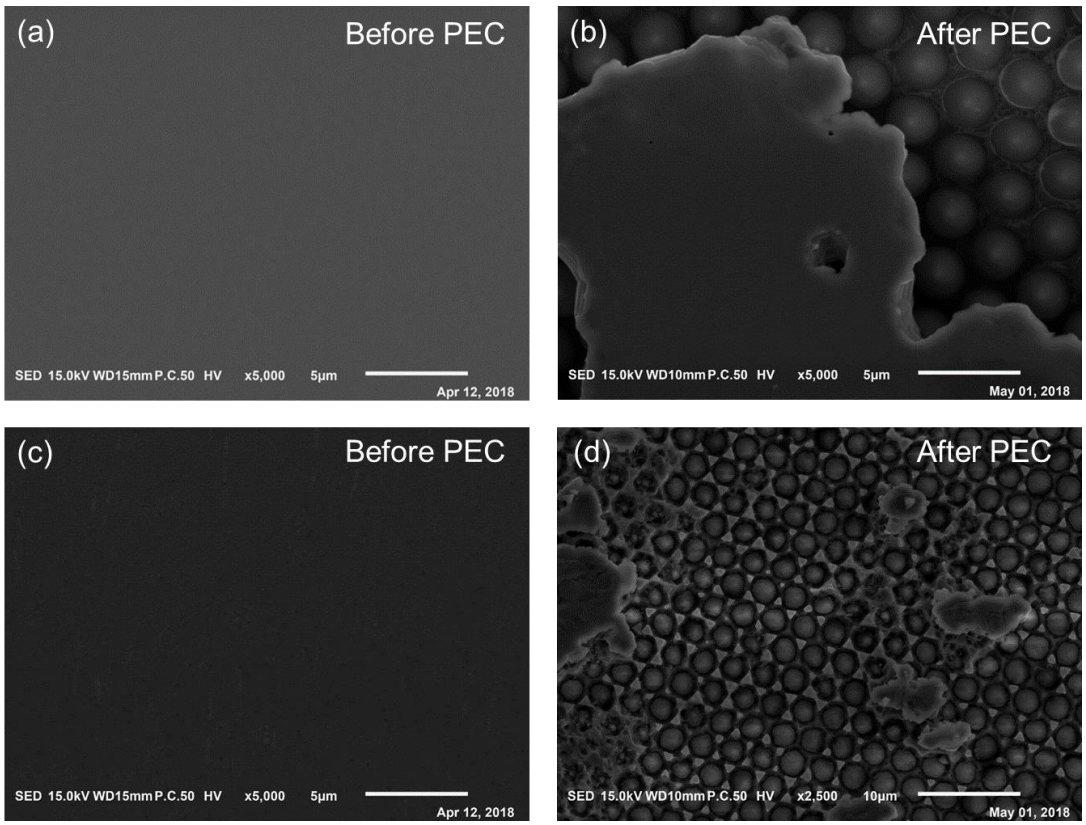

Figure 5.12. Scanning electron microscope (SEM) images for both InGaN/GaN MQWs photoanodes. (**a-b)** SEM images showing the morphology of the InGaN/GaN MQWs-CoO_x photoanode before and after the PEC test. **(c-d)** SEM images showing the morphology of the InGaN/GaN MQWs photoanode before and after the PEC test.

X-ray photoelectron spectroscopy (XPS) was carried out on the InGaN/GaN MQWs photoanodes before and after PEC analysis, as shown in Figure 5.13 and Figure 5.14. For the bare InGaN/GaN MQW before PEC, as shown in Figure 5.13, peaks were seen in the Ga 2p spectrum that were fitted with a simple doublet separated by 26.9 eV, with the Ga $2p_{3/2}$ transition centred at 1117.2 eV and corresponding to Ga-N (217). The N 1s spectrum showed an asymmetric broad peak with two distinct shoulders. A good fit was obtained by deconvoluting the experimental data using three peaks with a full-width half maximum of 1.6–1.9 eV, as suggested by Bertoti (217). Doing so yielded a primary peak centred at 397.1 eV, corresponding to N-Ga (217). The additional peaks at lower binding energies of 395.4 and 393.9 eV do not appear

to match any N species, but this may be due to oxygen contamination (which was detected on the surface and in the bulk [data not shown], which is known to cause N 1s peaks to shift in metal nitride films (217)). After PEC, XPS analysis of bare InGaN/GaN MQW showed the surface to have deteriorated, resulting in a much weaker signal for the Ga 2p transition than previously seen. The N 1s spectrum, when deconvoluted, showed a principle peak at 399.4 eV corresponding to surface organic nitrogen species. Additional peaks were seen at 396.4 and 394.4 eV, corresponding to N bound to Ga, and possibly N-In (respectively) as a weak signal for In 3d was also observed, as shown in Figure 5.13 (218).

For the InGaN/GaN MQWs-CoO_x photoanode before PEC analysis, as shown in Figure 5.14, XPS showed the immediate surface to be composed only of Co_3O_4, as expected due to the surface oxidation of CoO_x. The Co $2p_{3/2}$ transition was deconvoluted using five peaks according to the fitting parameters given by Biesinger et al (209). After PEC analysis, the protective CoO_x layer was still present (as also observed via SEM). However, XPS peaks for In 3d, Ga 2p, and N 1s were now also visible, suggesting that the CoO_x layer, though present, was partially deteriorated by the electrolyte solution during PEC, as shown in Figure 5.14. The In 3d spectrum was a simple doublet, with the In $3d_{5/2}$ peak centred at 444.3 eV corresponding to In-N. The Ga 2p3/2 transition was centred at 1116.6 eV, which is within the range for Ga-N (217). The nitrogen 1s spectrum showed four different environments, as explained before, with the most prominent peak at 396.5 eV and assigned to N bound to Ga (217).

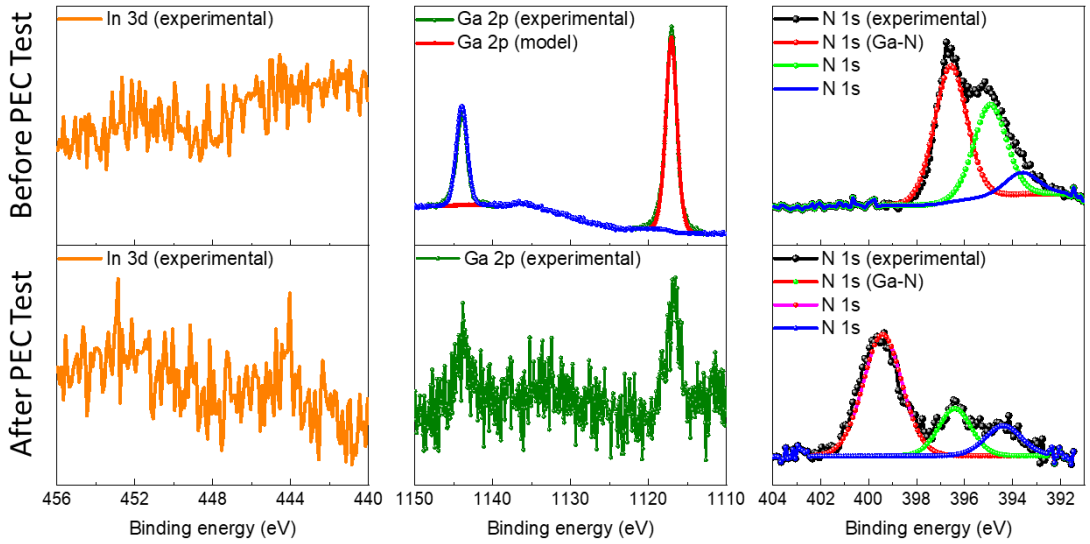

Figure 5.13. X-ray photoelectron spectroscopy (XPS) of both InGaN/GaN MQWs photoanodes before and after PEC testing. XPS spectra showing the surface composition of the InGaN/GaN MQWs photoanode detailing of Ga, N, and In transitions before and after a 2 h reliability test.

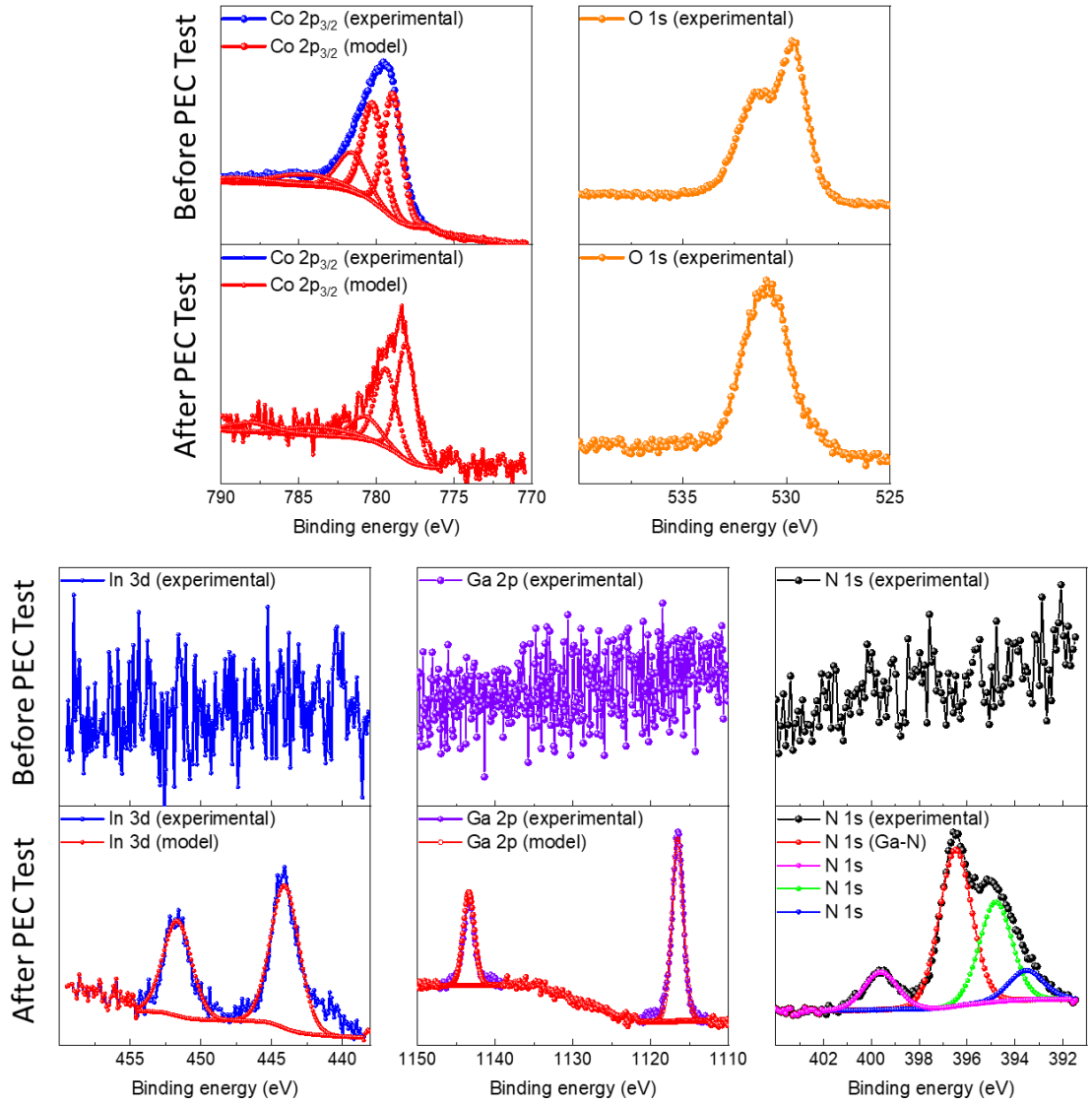

Figure 5.14. Chemical properties of both InGaN/GaN MQWs photoanodes before and after stability test. XPS spectra showing the surface composition of the InGaN/GaN MQWs modified with CoO_x photoanode detailing of Co, and O before and after a 28 h reliability test.

5.4. Conclusion

In this chapter, a nearly dislocation-free MQW InGaN/GaN photoanodes grown by MOCVD were developed. As the performance of photoanode depends strongly on the material quality and co-catalyst, high efficiency and long stability were successfully achieved by using such a CoO_x earth-abundant and highly active co-catalyst for oxidation evolution reaction. A CoO_x thin-film coating on the surface of the InGaN/GaN MQWs photoanode significantly enhanced the stability up to 20 hours, maintaining > 50% of the initial photocurrent density, while the InGaN/GaN MQWs without catalyst began to corrode in the first 30 min. In addition, electrochemical impedance spectroscopy and surface characterizations showed that InGaN/GaN MQWs modified with CoO_x reduced the reaction resistance to some extent, thus providing enhanced PEC efficiency and stability. The results presented in this chapter could have a strong impact on the future improvement of InGaN/GaN for PEC water splitting devices.

Chapter 6: Conclusions and Further Work

6.1. Conclusions

This thesis has presented the materials growth and photoelectrochemcial (PEC) analysis of III-V semiconductor photoelectrodes for PEC water splitting. The introductory chapters provided an introduction to solar energy and the principle of PEC water splitting as well as a summary of experimental methods for materials growth, materials analysis, and PEC measurement techniques. The experimental chapters explored various III-V semiconductor photoelectrodes for efficient solar fuel production.

The first experimental chapter reported a high-quality gallium phosphide photocathode directly grown on a silicon substrate by solid-source molecular beam epitaxy (MBE). The GaP photocathode can be stabilized under acidic electrolyte 1.0 M $HClO_4$ (pH=0) with an amorphous ALD-TiO_2 that functions as a protection layer and coated with a molybdenum sulphide MoS_2 hydrogen evolution catalyst. The PEC studies for the GaP photocathode grown on a silicon substrate show the potential for a widespread deployment of cost-effective photoelectrodes for hydrogen generation.

The second experimental chapter demonstrated a perfectly relaxed $GaP_{1-x}Sb_x$ (X = 0.33) monocrystalline alloy on a silicon substrate for PEC water oxidation. The alloy was monolithically grown on silicon, without any evidence of chemical disorders. The $GaP_{0.67}Sb_{0.33}$ photoanode shows an ideal direct band gap for full visible spectrum coverage and PEC water splitting. Under one-sun illumination, the $GaP_{0.67}Sb_{0.33}$ photoanode protected by amorphous TiO_2 and Ni exhibited a high photocurrent

density and stabilized for 5 h without degradation of the photocurrent in strongly alkaline conditions.

The final experimental chapter of this thesis presented the growth and fabrication of the InGaN/GaN MQWs photoanode for PEC solar water splitting. It has been found that the band edges of InGaN/GaN with a tuneable bandgap in the visible region can straddle water oxidation and hydrogen reduction potentials up to nearly the band gap of 1.23 eV, which is thermodynamically required to split water (93). The high quality InGaN/GaN MQWs structure and high activity of the cobalt oxide co-catalyst under simulated solar illumination provides a high photocurrent, onset potentials, and long stability. This study provides a critical insight into the potential role of metal-nitride InGaN/GaN in PEC applications. Thus, the realization of a highly efficient, stable, and scalable photoanode in a high-pH alkaline solution addresses the essential requirement for future PEC water splitting systems.

6.2. Future Work

The PEC pathway to hydrogen production has the potential to become economically viable, but the complexity of semiconductor photoelectrodes and the high cost associated with the fabrication process render their use impractical. Despite the promising results regarding the III-V semiconductor photoelectrodes presented in this thesis, the future work on the development of III-V photoelectrodes would involve improving and optimizing the growth quality of gallium phosphate (GaP) and gallium phosphate antimony ($GaP_{1-x}Sb_x$) grown on silicon wafer due to the lattice-mismatch, and thermal expansion coefficients between GaP and silicon (91). However, these obstacles result in defects such as threading Dislocations (TDs) that effect the active regions of the photoelectrode which is leading to poor PEC performance. Thus, the

reduction in the defects and improvement in the quality of the structure should improve the solar-to-hydrogen (STH) efficiency and PEC performance.

Another possible area of future work would be to rely on an optimized GaP photoelectrode that is connected electronically in series with Si, which could therefore in principle achieve a high solar-to-hydrogen efficiency of 12% under AM1.5 illumination. Moreover, reducing the bandgap of GaP to ~1.7 eV, by alloying with Sb content, may pave the way for the ideal tandem photoelectrochemical system with a theoretical solar-to-hydrogen efficiency of 27% (11).

The InGaN materials is a promising photoelectrode that can be used as the top light absorber in tandem structure and single absorber photoelectrodes for water splitting because of its tunable bandgap from 3.4 to 0.65 eV by incorporating the high indium content. Furthermore, the band edges alignment of InGaN straddle the water redox potentials for an indium composition up to ~50%. Therefore, the bandgap should be approximately 1.7 eV to split water without any external bias being required. Assuming a light-absorber with a bandgap of 1.7 eV which exhibits a unity external quantum efficiency, its maximum short circuit current density under AM1.5 G illumination can reach approximately 22.45 mA/cm^2, which corresponds to 27.6% solar-to-hydrogen (STH) efficiency (72, 95, 117).

Finally, the long-term stability of III-V semiconductor photoelectrodes operating under highly oxidizing or reducing potentials is the key for the realization of practical PEC cells. However, the development of both efficient and stable semiconductor photoanodes has been one of the greatest challenges for PEC water splitting systems. As a result, although the protection layers and catalyst would provide a good electrical property, e.g. high conductivity and efficient extraction of charges, the protection

layers and catalyst would also reduce corrosion and improve their chemical or photochemical stability when immersed in an electrolyte.

Chapter 7: References

1. Fujishima A, Honda K. Electrochemical Photolysis of Water at a Semiconductor Electrode. Nature. 1972;238(5358):37-8.

2. Lee DK, Choi K-S. Enhancing long-term photostability of $BiVO_4$ photoanodes for solar water splitting by tuning electrolyte composition. Nature Energy. 2017;3(1):53-60.

3. Iwashina K, Kudo A. Rh-doped $SrTiO_3$ photocatalyst electrode showing cathodic photocurrent for water splitting under visible-light irradiation. Journal of the American Chemical Society. 2011;133(34):13272-5.

4. Zhong DK, Sun J, Inumaru H, Gamelin DR. Solar water oxidation by composite catalyst/alpha-Fe_2O_3 photoanodes. Journal of the American Chemical Society. 2009;131(17):6086-7.

5. Kim JY, Magesh G, Youn DH, Jang JW, Kubota J, Domen K, et al. Single-crystalline, wormlike hematite photoanodes for efficient solar water splitting. Scientific Reports. 2013;3:2681.

6. Mayer MT, Lin Y, Yuan G, Wang D. Forming heterojunctions at the nanoscale for improved photoelectrochemical water splitting by semiconductor materials: case studies on hematite. Accounts of Chemical Research. 2013;46(7):1558-66.

7. Iandolo B, Zhang H, Wickman B, Zorić I, Conibeer G, Hellman A. Correlating flat band and onset potentials for solar water splitting on model hematite photoanodes. RSC Advances. 2015;5(75):61021-30.

8. Zhong M, Hisatomi T, Kuang Y, Zhao J, Liu M, Iwase A, et al. Surface Modification of CoO_x Loaded $BiVO_4$ Photoanodes with Ultrathin p-Type NiO Layers for Improved Solar Water Oxidation. Journal of the American Chemical Society. 2015;137(15):5053-60.

9. Ramakrishnan V, Kim H, Park J, Yang B. Cobalt oxide nanoparticles on TiO_2 nanorod/FTO as a photoanode with enhanced visible light sensitization. RSC Advances. 2016;6(12):9789-95.

10. Hu S, Shaner MR, Beardslee JA, Lichterman M, Brunschwig BS, Lewis NS. Amorphous TiO_2 coatings stabilize Si, GaAs, and GaP photoanodes for efficient water oxidation. Science. 2014;344(6187):1005-9.

11. Wu J, Li Y, Kubota J, Domen K, Aagesen M, Ward T, et al. Wafer-scale fabrication of self-catalyzed 1.7 eV GaAsP core-shell nanowire photocathode on silicon substrates. Nano Letter. 2014;14(4):2013-8.

12. Young JL, Steirer KX, Dzara MJ, Turner JA, Deutsch TG. Remarkable stability of unmodified GaAs photocathodes during hydrogen evolution in acidic electrolyte. Journal of Materials Chemistry A. 2016;4(8):2831-6.

13. Yang F, Nielander AC, Grimm RL, Lewis NS. Photoelectrochemical Behavior of n-Type GaAs(100) Electrodes Coated by a Single Layer of Graphene. The Journal of Physical Chemistry C. 2016;120(13):6989-95.

14. Malizia M, Seger B, Chorkendorff I, Vesborg PCK. Formation of a p–n heterojunction on GaP photocathodes for H_2 production providing an open-circuit voltage of 710 mV. Journal of Materials Chemistry A. 2014;2(19):6847-53.

15. Standing A, Assali S, Gao L, Verheijen MA, van Dam D, Cui Y, et al. Efficient water reduction with gallium phosphide nanowires. Nature Communication. 2015;6:7824.

16. Gu J, Aguiar JA, Ferrere S, Steirer KX, Yan Y, Xiao C, et al. A graded catalytic–protective layer for an efficient and stable water-splitting photocathode. Nature Energy. 2017;2(2):16192.

17. Lin Y, Kapadia R, Yang J, Zheng M, Chen K, Hettick M, et al. Role of TiO_2 Surface Passivation on Improving the Performance of p-InP Photocathodes. The Journal of Physical Chemistry C. 2015;119(5):2308-13.

18. Parameshwaran V, Xu X, Clemens B. Crystallinity, Surface Morphology, and Photoelectrochemical Effects in Conical InP and InN Nanowires Grown on Silicon. ACS Applied Materials & Interfaces. 2016;8(33):21454-64.

19. Walter MG, Warren EL, McKone JR, Boettcher SW, Mi Q, Santori EA, et al. Solar water splitting cells. Chemical Reviews. 2010;110(11):6446-73.

20. Scheuermann AG, McIntyre PC. Atomic Layer Deposited Corrosion Protection: A Path to Stable and Efficient Photoelectrochemical Cells. The Journal of Physical Chemistry Letters. 2016;7(14):2867-78.

21. Bae D, Seger B, Vesborg PC, Hansen O, Chorkendorff I. Strategies for stable water splitting via protected photoelectrodes. Chemical Society Reviews. 2017;46(7):1933-54.

22. Gu J, Yan Y, Young JL, Steirer KX, Neale NR, Turner JA. Water reduction by a p-$GaInP_2$ photoelectrode stabilized by an amorphous TiO_2 coating and a molecular cobalt catalyst. Nature Materials. 2016;15(4):456-60.

23. Sun K, Kuang Y, Verlage E, Brunschwig BS, Tu CW, Lewis NS. Sputtered NiO_x Films for Stabilization of p^+n-InP Photoanodes for Solar-Driven Water Oxidation. Advanced Energy Materials. 2015;5(11).

24. Li Q, Zheng M, Zhong M, Ma L, Wang F, Ma L, et al. Engineering MoS_x/Ti/InP Hybrid Photocathode for Improved Solar Hydrogen Production. Scientific Report. 2016;6:29738.

25. Yang J, Wang D, Han H, Li C. Roles of cocatalysts in photocatalysis and photoelectrocatalysis. Accounts of Chemical Research. 2013;46(8):1900-9.

26. Gratzel M. Photoelectrochemical cells. Nature. 2001;414(6861):338-44.

27. Turner JA. Sustainable hydrogen production. Science. 2004;305(5686):972-4.

28. Lewis NS. Research opportunities to advance solar energy utilization. Science. 2016;351(6271):aad1920.

29. Jiang C, Moniz SJA, Wang A, Zhang T, Tang J. Photoelectrochemical devices for solar water splitting - materials and challenges. Chemical Society Reviews. 2017;46(15):4645-60.

30. Lessio M, Carter EA. What Is the Role of Pyridinium in Pyridine-Catalyzed CO_2 Reduction on p-GaP Photocathodes? Journal of the American Chemical Society. 2015;137(41):13248-51.

31. Barber J. Photosynthetic energy conversion: natural and artificial. Chemical Society Reviews. 2009;38(1):185-96.

32. Li J, Wu N. Semiconductor-based photocatalysts and photoelectrochemical cells for solar fuel generation: a review. Catalysis Science & Technology. 2015;5(3):1360-84.

33. Lewis NS. Powering the Planet. MRS Bulletin. 2011;32(10):808-20.

34. Service RF. Solar energy. Is it time to shoot for the sun? Science. 2005;309(5734):548-51.

35. Lewis NSC, G.; Nozik, A. J.; Wasielewski, M. R.; Alivisatos, P.; Kung, H.; Tsao, J.; Chandler, E.; Walukiewicz, W.; Spitler, M.; Ellingson, R.; Overend, R.; Mazer, J.; Gress, M.; Horwitz, J.; Ashton, C.; Herndon, B.; Shapard, L.; Nault, R. M. Basic Research Needs for Solar Energy Utilization. Report of the Basic Energy Sciences Workshop on Solar Energy Utilization. 2005.

36. Tachibana Y, Vayssieres L, Durrant JR. Artificial photosynthesis for solar water-splitting. Nature Photonics. 2012;6(8):511-8.

37. Luo J, Steier L, Son MK, Schreier M, Mayer MT, Gratzel M. Cu2O Nanowire Photocathodes for Efficient and Durable Solar Water Splitting. Nano Letter. 2016;16(3):1848-57.

38. Murphy A, Barnes P, Randeniya L, Plumb I, Grey I, Horne M, et al. Efficiency of solar water splitting using semiconductor electrodes. International Journal of Hydrogen Energy. 2006;31(14):1999-2017.

39. Shi X, Jeong H, Oh SJ, Ma M, Zhang K, Kwon J, et al. Unassisted photoelectrochemical water splitting exceeding 7% solar-to-hydrogen conversion efficiency using photon recycling. Nature Communication. 2016;7:11943.

40. Fountaine KT, Lewerenz HJ, Atwater HA. Efficiency limits for photoelectrochemical water-splitting. Nature Communication. 2016;7:13706.

41. McKone JR, Lewis NS, Gray HB. Will Solar-Driven Water-Splitting Devices See the Light of Day? Chemistry of Materials. 2013;26(1):407-14.

42. Gray EM. Hydrogen storage – status and prospects. Advances in Applied Ceramics. 2013;106(1-2):25-8.

43. Bossel U. Does a Hydrogen Economy Make Sense? Proceedings of the IEEE. 2006;94(10):1826-37.

44. van de Krol R, Grätzel M. Photoelectrochemical Hydrogen Production2012.

45. Bak T, Nowotny J, Rekas M, Sorrell CC. Photo-electrochemical hydrogen generation from water using solar energy. Materials-related aspects. International Journal of Hydrogen Energy. 2002;27(10):991-1022.

46. Ager JW, Shaner MR, Walczak KA, Sharp ID, Ardo S. Experimental demonstrations of spontaneous, solar-driven photoelectrochemical water splitting. Energy & Environmental Science. 2015;8(10):2811-24.

47. Nozik AJ, Memming R. Physical Chemistry of Semiconductor−Liquid Interfaces. The Journal of Physical Chemistry. 1996;100(31):13061-78.

48. Pierret RF. Advanced Semiconductor Fundamentals: Prentice Hall; 2003.

49. Zhang XG. Electrochemistry of Silicon and Its Oxide: Springer; 2014.

50. Seraphin BO. Solar Energy Conversion1979.

51. Krishnan R. Fundamentals of Semiconductor Electrochemistry and Photoelectrochemistry. Encyclopedia of Electrochemistry 2007.

52. Lewerenz HJ, Sharp ID. Chapter 1. Concepts of Photoelectrochemical Energy Conversion and Fuel Generation. Integrated Solar Fuel Generators. Energy and Environment Series: The Royal Society of Chemistry; 2018. p. 1-42.

53. Turner JA. Energetics of the semiconductor-electrolyte interface. Journal of Chemical Education. 1983;60(4).

54. Giménez S, Bisquert J. Photoelectrochemical Solar Fuel Production 2016.

55. Guldi D. Nanostructured and Photoelectrochemical Systems for Solar Photon Conversion.Edited by Mary D. Archer, Arthur J. Nozik. ChemSusChem. 2009;2(2):185-6.

56. Chen Z, Dinh HN, Miller E. Photoelectrochemical Water Splitting. Energy Si, editor 2013.

57. Bard AJ. Photoelectrochemistry and heterogeneous photo-catalysis at semiconductors. Journal of Photochemistry. 1979;10(1):59-75.

58. Chen S, Wang L-W. Thermodynamic Oxidation and Reduction Potentials of Photocatalytic Semiconductors in Aqueous Solution. Chemistry of Materials. 2012;24(18):3659-66.

59. Liu R, Zheng Z, Spurgeon J, Yang X. Enhanced photoelectrochemical water-splitting performance of semiconductors by surface passivation layers. Energy & Environmental Science 2014;7(8):2504-17.

60. Pendlebury SR, Wang X, Le Formal F, Cornuz M, Kafizas A, Tilley SD, et al. Ultrafast charge carrier recombination and trapping in hematite photoanodes under applied bias. Journal of the American Chemical Society. 2014;136(28):9854-7.

61. Rai S, Ikram A, Sahai S, Dass S, Shrivastav R, Satsangi VR. Morphological, optical and photoelectrochemical properties of Fe_2O_3–GNP composite thin films. RSC Advances. 2014;4(34):17671.

62. Corby S, Francas L, Selim S, Sachs M, Blackman C, Kafizas A, et al. Water Oxidation and Electron Extraction Kinetics in Nanostructured Tungsten

Trioxide Photoanodes. Journal of the American Chemical Society. 2018;140(47):16168-77.

63. Sotelo-Vazquez C, Quesada-Cabrera R, Ling M, Scanlon DO, Kafizas A, Thakur PK, et al. Evidence and Effect of Photogenerated Charge Transfer for Enhanced Photocatalysis in WO_3/TiO_2 Heterojunction Films: A Computational and Experimental Study. Advanced Functional Materials. 2017;27(18).

64. Ma Y, Pendlebury SR, Reynal A, Le Formal F, Durrant JR. Dynamics of photogenerated holes in undoped $BiVO_4$ photoanodes for solar water oxidation. Chemical Science. 2014;5(8):2964-73.

65. Licht S, Wang B, Mukerji S, Soga T, Umeno M, Tributsch H. Efficient Solar Water Splitting, Exemplified by RuO_2-Catalyzed AlGaAs/Si Photoelectrolysis. The Journal of Physical Chemistry B. 2000;104(38):8920-4.

66. Benck JD, Chen Z, Kuritzky LY, Forman AJ, Jaramillo TF. Amorphous Molybdenum Sulfide Catalysts for Electrochemical Hydrogen Production: Insights into the Origin of their Catalytic Activity. ACS Catalysis. 2012;2(9):1916-23.

67. Lee MH, Takei K, Zhang J, Kapadia R, Zheng M, Chen YZ, et al. p-Type InP nanopillar photocathodes for efficient solar-driven hydrogen production. Angewandte Chemie Int Ed Engl. 2012;51(43):10760-4.

68. Hettick M, Zheng M, Lin Y, Sutter-Fella CM, Ager JW, Javey A. Nonepitaxial Thin-Film InP for Scalable and Efficient Photocathodes. The Journal of Physical Chemistry Letters. 2015;6(12):2177-82.

69. Sun J, Liu C, Yang P. Surfactant-free, large-scale, solution-liquid-solid growth of gallium phosphide nanowires and their use for visible-light-driven hydrogen production from water reduction. Journal of the American Chemical Society. 2011;133(48):19306-9.

70. Krawicz A, Cedeno D, Moore GF. Energetics and efficiency analysis of a cobaloxime-modified semiconductor under simulated air mass 1.5 illumination. Physical Chemistry Chemical Physics. 2014;16(30):15818-24.

71. Alqahtani M, Ben-Jabar S, Ebaid M, Sathasivam S, Jurczak P, Xia X, et al. Gallium Phosphide photoanode coated with TiO_2 and CoO_x for stable photoelectrochemical water oxidation. Optics Express. 2019;27(8):A364-A71.

72. Strandwitz NC, Turner-Evans DB, Tamboli AC, Chen CT, Atwater HA, Lewis NS. Photoelectrochemical Behavior of Planar and Microwire-Array Si|GaP Electrodes. Advance Energy Materails. 2012;2(9):1109-16.

73. Alqahtani M, Sathasivam S, Cui F, Steier L, Xia X, Blackman C, et al. Heteroepitaxy of GaP on silicon for efficient and cost-effective photoelectrochemical water splitting. Journal of Materials Chemistry A. 2019;7(14):8550-8.

74. Lee YH, Kim J, Oh J. Wafer-Scale Ultrathin, Single-Crystal Si and GaAs Photocathodes for Photoelectrochemical Hydrogen Production. ACS Applied Materails Interfaces. 2018;10(39):33230-7.

75. Tee SY, Win KY, Teo WS, Koh LD, Liu S, Teng CP, et al. Recent Progress in Energy-Driven Water Splitting. Advanced Science. 2017;4(5):1600337.

76. Kim JH, Hansora D, Sharma P, Jang JW, Lee JS. Toward practical solar hydrogen production - an artificial photosynthetic leaf-to-farm challenge. Chemical Society Reviews. 2019;48(7):1908-71.

77. Liu P, Zheng M, Li Q, Ma L, Wang F, Jiang D, et al. A one-step method to fabricate novel three-dimensional GaP nanopore arrays for enhanced photoelectrochemical hydrogen production. Chemical Communications. 2017;53(91):12333-6.

78. Neuderth P, Hille P, Schörmann J, Frank A, Reitz C, Martí-Sánchez S, et al. Passivation layers for nanostructured photoanodes: ultra-thin oxides on InGaN nanowires. Journal of Materials Chemistry A. 2018;6(2):565-73.

79. Kargar A, Sukrittanon S, Zhou C, Ro YG, Pan X, Dayeh SA, et al. GaP/GaNP Heterojunctions for Efficient Solar-Driven Water Oxidation. Small. 2017;13(21).

80. Caccamo L, Cocco G, Martin G, Zhou H, Fundling S, Gad A, et al. Insights into Interfacial Changes and Photoelectrochemical Stability of $In_xGa_{1-x}N$ (0001) Photoanode Surfaces in Liquid Environments. ACS Applied Materails Interfaces. 2016;8(12):8232-8.

81. Zeng J, Xu X, Parameshwaran V, Baker J, Bent S, Wong HSP, et al. Photoelectrochemical Water Oxidation by GaAs Nanowire Arrays Protected with Atomic Layer Deposited NiO_x Electrocatalysts. Journal of Electronic Materials. 2017;47(2):932-7.

82. Wang T, Gong J. Single-Crystal Semiconductors with Narrow Band Gaps for Solar Water Splitting. Angew Chem Int Ed Engl. 2015;54(37):10718-32.

83. Heller A, Lewerenz HJ, Miller B. Combined Ruthenium Lead Surface Treatment of Gallium Arsenide Photoanodes. Chemie. 1980;84(6):592-5.

84. Allongue P. Charge Transfer Process at Illuminated Semiconductor/Electrolyte Junctions Modified by Electrodeposition of Microscopic Metal Grain. Journal of The Electrochemical Society. 1989;136(4).

85. Frese KW, Madou MJ, Morrison SR. Investigation of photoelectrochemical corrosion of semiconductors. The Journal of Physical Chemistry. 1980;84(24):3172-8.

86. Sun ZW, Campet G. n-GaAs photoelectrodes coated with $SrTiO_3$-based films: Charge transfer mechanisms and stability. Materials Science and Engineering: B. 1990;5(4):455-64.

87. Kainthla RC. Significant Efficiency Increase in Self-Driven Photoelectrochemical Cell for Water Photoelectrolysis. Journal of The Electrochemical Society. 1987;134(4).

88. Rajeshwar K. Regenerative Photoelectrochemical Cells Using Polymer-Coated n-GaAs Photoanodes in Contact with Aqueous Electrolytes. Journal of The Electrochemical Society. 1983;130(1).

89. Lucci I, Charbonnier S, Pedesseau L, Vallet M, Cerutti L, Rodriguez JB, et al. Universal description of III-V/Si epitaxial growth processes. Physical Review Materials 2018;2(6).

90. Georges Siddiqi ZP, Shu Hu,. III–V Semiconductor Photoelectrodes Semiconduct. Semimet. Elsevier: Elsevier BV; 2017.

91. Ning C-Z, Dou L, Yang P. Bandgap engineering in semiconductor alloy nanomaterials with widely tunable compositions. Nature Reviews Materials. 2017;2(12).

92. Robert C, Bondi A, Thanh TN, Even J, Cornet C, Durand O, et al. Room temperature operation of GaAsP(N)/GaP(N) quantum well based light-emitting diodes: Effect of the incorporation of nitrogen. Applied Physics Letters. 2011;98(25):251110.

93. Moses PG, Van de Walle CG. Band bowing and band alignment in InGaN alloys. Applied Physics Letters. 2010;96(2):021908.

94. Benton J, Bai J, Wang T. Utilisation of GaN and InGaN/GaN with nanoporous structures for water splitting. Applied Physics Letters. 2014;105(22):223902.

95. Chu S, Vanka S, Wang Y, Gim J, Wang Y, Ra Y-H, et al. Solar Water Oxidation by an InGaN Nanowire Photoanode with a Bandgap of 1.7 eV. ACS Energy Letters. 2018;3(2):307-14.

96. Benton J, Bai J, Wang T. Significantly enhanced performance of an InGaN/GaN nanostructure based photo-electrode for solar power hydrogen generation. Applied Physics Letters. 2013;103(13).

97. Nakamura S. The roles of structural imperfections in InGaN-based blue light-emitting diodes and laser diodes. Science. 1998;281(5379):955-61.

98. Yeh TW, Lin YT, Stewart LS, Dapkus PD, Sarkissian R, O'Brien JD, et al. InGaN/GaN multiple quantum wells grown on nonpolar facets of vertical GaN nanorod arrays. Nano Letter. 2012;12(6):3257-62.

99. AlOtaibi B, Nguyen HP, Zhao S, Kibria MG, Fan S, Mi Z. Highly stable photoelectrochemical water splitting and hydrogen generation using a double-band InGaN/GaN core/shell nanowire photoanode. Nano Letter. 2013;13(9):4356-61.

100. Kamimura J, Bogdanoff P, Abdi FF, Lähnemann J, van de Krol R, Riechert H, et al. Photoelectrochemical Properties of GaN Photoanodes with Cobalt Phosphate Catalyst for Solar Water Splitting in Neutral Electrolyte. The Journal of Physical Chemistry C. 2017;121(23):12540-5.

101. Ebaid M, Priante D, Liu G, Zhao C, Sharizal Alias M, Buttner U, et al. Unbiased photocatalytic hydrogen generation from pure water on stable Ir-treated In 0.33 Ga 0.67 N nanorods. Nano Energy. 2017;37:158-67.

102. Liu G, Karuturi SK, Simonov AN, Fekete M, Chen H, Nasiri N, et al. Robust Sub-Monolayers of Co_3O_4 Nano-Islands: A Highly Transparent Morphology for Efficient Water Oxidation Catalysis. Advanced Energy Materials. 2016;6(15).

103. Britto RJ, Benck JD, Young JL, Hahn C, Deutsch TG, Jaramillo TF. Molybdenum Disulfide as a Protection Layer and Catalyst for Gallium Indium Phosphide Solar Water Splitting Photocathodes. The Journal of Physical Chemistry Letters 2016;7(11):2044-9.

104. May MM, Lewerenz HJ, Lackner D, Dimroth F, Hannappel T. Efficient direct solar-to-hydrogen conversion by in situ interface transformation of a tandem structure. Nature Communication. 2015;6:8286.

105. Khaselev O, Turner JA. A monolithic photovoltaic-photoelectrochemical device for hydrogen production via water splitting. Science. 1998;280(5362):425-7.

106. Verlage E, Hu S, Liu R, Jones RJR, Sun K, Xiang C, et al. A monolithically integrated, intrinsically safe, 10% efficient, solar-driven water-splitting system based on active, stable earth-abundant electrocatalysts in conjunction with tandem III–V light absorbers protected by amorphous TiO_2 films. Energy & Environmental Science. 2015;8(11):3166-72.

107. Cheng W-H, Richter MH, May MM, Ohlmann J, Lackner D, Dimroth F, et al. Monolithic Photoelectrochemical Device for Direct Water Splitting with 19% Efficiency. ACS Energy Letters. 2018;3(8):1795-800.

108. Cheng W-H, Richter MH, May MM, Ohlmann J, Lackner D, Dimroth F, et al. Monolithic Photoelectrochemical Device for Direct Water Splitting with 19% Efficiency. ACS Energy Letters. 2018;3(8):1795-800.

109. Coridan RH, Nielander AC, Francis SA, McDowell MT, Dix V, Chatman SM, et al. Methods for comparing the performance of energy-conversion systems for use in solar fuels and solar electricity generation. Energy & Environmental Science. 2015;8(10):2886-901.

110. Dotan H, Mathews N, Hisatomi T, Gratzel M, Rothschild A. On the Solar to Hydrogen Conversion Efficiency of Photoelectrodes for Water Splitting. The Journal of Physical Chemistry Letters. 2014;5(19):3330-4.

111. Brozel M. Gallium Arsenide. In: Kasap S, Capper P, editors. Springer Handbook of Electronic and Photonic Materials. Boston, MA: Springer US; 2006. p. 499-536.

112. Ansari AA, Alhoshan M, Alsalhi MS, Aldwayyan AS. Prospects of nanotechnology in clinical immunodiagnostics. Sensors (Basel). 2010;10(7):6535-81.

113. George SM. Atomic layer deposition: an overview. Chemical Reviews. 2010;110(1):111-31.

114. Johnson RW, Hultqvist A, Bent SF. A brief review of atomic layer deposition: from fundamentals to applications. Materials Today. 2014;17(5):236-46.

115. Razeghi M. Semiconductor Characterization Techniques. Fundamentals of Solid State Engineering. Boston, MA: Springer US; 2006. p. 521-49.

116. Bard AJ. Photoelectrochemistry. Science. 1980;207(4427):139-44.

117. Seger B, Castelli IE, Vesborg PCK, Jacobsen KW, Hansen O, Chorkendorff I. 2-Photon tandem device for water splitting: comparing photocathode first versus photoanode first designs. Energy & Environmental Science. 2014;7(8):2397-413.

118. Nandjou F, Haussener S. Degradation in photoelectrochemical devices: review with an illustrative case study. Journal of Physics D: Applied Physics. 2017;50(12).

119. Shaner MR, Atwater HA, Lewis NS, McFarland EW. A comparative technoeconomic analysis of renewable hydrogen production using solar energy. Energy & Environmental Science. 2016;9(7):2354-71.

120. Armstrong RC, Wolfram C, de Jong KP, Gross R, Lewis NS, Boardman B, et al. The frontiers of energy. Nature Energy. 2016;1(1):15020.

121. Lewis NS, Nocera DG. Powering the planet: chemical challenges in solar energy utilization. Proceedings of the National Academy of Sciences of the United States of America. 2006;103(43):15729-35.

122. Jiang C, Moniz SJ, Khraisheh M, Tang J. Earth-abundant oxygen evolution catalysts coupled onto ZnO nanowire arrays for efficient photoelectrochemical water cleavage. Chemistry. 2014;20(40):12954-61.

123. Kim TW, Choi KS. Nanoporous $BiVO_4$ photoanodes with dual-layer oxygen evolution catalysts for solar water splitting. Science. 2014;343(6174):990-4.

124. Guilleme P, Vallet M, Stodolna J, Ponchet A, Cornet C, Letoublon A, et al. Antiphase domain tailoring for combination of modal and 4 -quasi-phase matching in gallium phosphide microdisks. Optics Express. 2016;24(13):14608-17.

125. Beiler AM, Khusnutdinova D, Jacob SI, Moore GF. Chemistry at the Interface: Polymer-Functionalized GaP Semiconductors for Solar Hydrogen Production. Industrial & Engineering Chemistry Research. 2016;55(18):5306-14.

126. Ziegler J, Fertig D, Kaiser B, Jaegermann W, Blug M, Hoch S, et al. Preparation and Characterization of GaP Semiconductor Electrodes for Photoelectrochemical Water Splitting. Energy Procedia. 2012;22:108-13.

127. Beiler AM, Khusnutdinova D, Jacob SI, Moore GF. Solar Hydrogen Production Using Molecular Catalysts Immobilized on Gallium Phosphide (111)A and (111)B Polymer-Modified Photocathodes. ACS Applied Materails Interfaces. 2016;8(15):10038-47.

128. Khusnutdinova D, Beiler AM, Wadsworth BL, Jacob SI, Moore GF. Metalloporphyrin-modified semiconductors for solar fuel production. Chemical Science. 2017;8(1):253-9.

129. Kornienko N, Gibson NA, Zhang H, Eaton SW, Yu Y, Aloni S, et al. Growth and Photoelectrochemical Energy Conversion of Wurtzite Indium Phosphide Nanowire Arrays. ACS Nano. 2016;10(5):5525-35.

130. Lucci I, Charbonnier S, Vallet M, Turban P, Léger Y, Rohel T, et al. A Stress-Free and Textured GaP Template on Silicon for Solar Water Splitting. Advanced Functional Materials. 2018;28(30):1801585.

131. Williams OM, Shi JW, Rose MJ. Photoelectrochemical study of p-GaP(100)|ZnO|AuNP devices: strategies for enhanced electron transfer and aqueous catalysis. Chemical Communications. 2016;52(58):9145-8.

132. Wilson RL, Simion CE, Blackman CS, Carmalt CJ, Stanoiu A, Di Maggio F, et al. The Effect of Film Thickness on the Gas Sensing Properties of Ultra-Thin TiO_2 Films Deposited by Atomic Layer Deposition. Sensors (Basel). 2018;18(3).

133. Emmer H, Chen CT, Saive R, Friedrich D, Horie Y, Arbabi A, et al. Fabrication of Single Crystal Gallium Phosphide Thin Films on Glass. Scientific Reports. 2017;7(1):4643.

134. Lu Q, Yu Y, Ma Q, Chen B, Zhang H. 2D Transition-Metal-Dichalcogenide-Nanosheet-Based Composites for Photocatalytic and Electrocatalytic Hydrogen Evolution Reactions. Advanced Materials. 2016;28(10):1917-33.

135. Moore GF, Sharp ID. A Noble-Metal-Free Hydrogen Evolution Catalyst Grafted to Visible Light-Absorbing Semiconductors. The Journal of Physical Chemistry Letters. 2013;4(4):568-72.

136. Paracchino A, Laporte V, Sivula K, Gratzel M, Thimsen E. Highly active oxide photocathode for photoelectrochemical water reduction. Nature Materails. 2011;10(6):456-61.

137. Chen YW, Prange JD, Duhnen S, Park Y, Gunji M, Chidsey CE, et al. Atomic layer-deposited tunnel oxide stabilizes silicon photoanodes for water oxidation. Nature Materails. 2011;10(7):539-44.

138. Seger B, Pedersen T, Laursen AB, Vesborg PC, Hansen O, Chorkendorff I. Using TiO_2 as a conductive protective layer for photocathodic H2 evolution. Journal of the American Chemical Society, 2013;135(3):1057-64.

139. Merki D, Hu X. Recent developments of molybdenum and tungsten sulfides as hydrogen evolution catalysts. Energy & Environmental Science. 2011;4(10):3878.

140. Morales-Guio CG, Tilley SD, Vrubel H, Gratzel M, Hu X. Hydrogen evolution from a copper(I) oxide photocathode coated with an amorphous molybdenum sulphide catalyst. Nature Communication. 2014;5:3059.

141. Seger B, Laursen AB, Vesborg PC, Pedersen T, Hansen O, Dahl S, et al. Hydrogen production using a molybdenum sulfide catalyst on a titanium-protected n^+p-silicon photocathode. Angewandte Chemie International Edition Engl. 2012;51(36):9128-31.

142. Lee S, Bielinski AR, Fahrenkrug E, Dasgupta NP, Maldonado S. Macroporous p-GaP Photocathodes Prepared by Anodic Etching and Atomic Layer Deposition Doping. ACS Applied Materails Interfaces. 2016;8(25):16178-85.

143. Lewis NS. A prospective on energy and environmental science. Energy & Environmental Science. 2019;12(1):16-8.

144. Quinci T, Kuyyalil J, Thanh TN, Wang YP, Almosni S, Létoublon A, et al. Defects limitation in epitaxial GaP on bistepped Si surface using UHVCVD–MBE growth cluster. Journal of Crystal Growth. 2013;380:157-62.

145. Verlage E, Hu S, Liu R, Jones RJR, Sun K, Xiang C, et al. A monolithically integrated, intrinsically safe, 10% efficient, solar-driven water-splitting system based on active, stable earth-abundant electrocatalysts in conjunction with tandem III–V light absorbers protected by amorphous TiO_2 films. Energy & Environmental Science. 2015;8(11):3166-72.

146. Kim JH, Jo YH, Kim JH, Lee JS. Ultrafast fabrication of highly active $BiVO_4$ photoanodes by hybrid microwave annealing for unbiased solar water splitting. Nanoscale. 2016;8(40):17623-31.

147. Zhen C, Wang L, Liu L, Liu G, Lu GQ, Cheng HM. Nonstoichiometric rutile TiO_2 photoelectrodes for improved photoelectrochemical water splitting. Chemical Communication. 2013;49(55):6191-3.

148. Eichhorn J, Kastl C, Cooper JK, Ziegler D, Schwartzberg AM, Sharp ID, et al. Nanoscale imaging of charge carrier transport in water splitting photoanodes. Nature Communication. 2018;9(1):2597.

149. Zhang J, Yu Z, Gao Z, Ge H, Zhao S, Chen C, et al. Porous TiO_2 Nanotubes with Spatially Separated Platinum and CoO_x Cocatalysts Produced by Atomic Layer Deposition for Photocatalytic Hydrogen Production. Angewandte Chemie International Edition Engl. 2017;56(3):816-20.

150. Russell HB, Andriotis AN, Menon M, Jasinski JB, Martinez-Garcia A, Sunkara MK. Direct Band Gap Gallium Antimony Phosphide ($GaSb_xP_{(1-x)}$) Alloys. Scientific Reports. 2016;6:20822.

151. Martinez-Garcia A, Russell HB, Paxton W, Ravipati S, Calero-Barney S, Menon M, et al. Unassisted Water Splitting Using a $GaSb_xP_{(1-x)}$ Photoanode. Advanced Energy Materials, 2018;8(16):1703247.

152. Sun K, Saadi FH, Lichterman MF, Hale WG, Wang HP, Zhou X, et al. Stable solar-driven oxidation of water by semiconducting photoanodes protected by transparent catalytic nickel oxide films. Proceedings of the National Academy of Sciences of the United States of America. 2015;112(12):3612-7.

153. Lichterman MF, Carim AI, McDowell MT, Hu S, Gray HB, Brunschwig BS, et al. Stabilization of n-cadmium telluride photoanodes for water oxidation to O_2(g) in aqueous alkaline electrolytes using amorphous TiO_2 films formed by atomic-layer deposition. Energy & Environmental Science. 2014;7(10):3334-7.

154. Jancu J-M, Scholz R, Beltram F, Bassani F. Empiricalspds*tight-binding calculation for cubic semiconductors: General method and material parameters. Physical Review B. 1998;57(11):6493-507.

155. Boyer-Richard S, Robert C, Gerard L, Richters JP, Andre R, Bleuse J, et al. Atomistic simulations of the optical absorption of type-II CdSe/ZnTe superlattices. Nanoscale Research Letters. 2012;7(1):543.

156. Scholz R, Jancu JM, Beltram F, Bassani F. Calculation of Electronic States in Semiconductor Heterostructures with an Empirical spds* Tight-Binding Model. physica status solidi (b). 2000;217(1):449-60.

157. Sacconi F, Di Carlo A, Lugli P, Stadele M, Jancu JM. Full band approach to tunneling in MOS structures. IEEE Transactions on Electron Devices. 2004;51(5):741-8.

158. Raouafi F, Samti R, Benchamekh R, Heyd R, Boyer-Richard S, Voisin P, et al. Optical properties of potential-inserted quantum wells in the near infrared and Terahertz ranges. Solid State Communications. 2016;236:7-11.

159. Ping Wang Y, Stodolna J, Bahri M, Kuyyalil J, Nguyen Thanh T, Almosni S, et al. Abrupt GaP/Si hetero-interface using bistepped Si buffer. Applied Physics Letters. 2015;107(19):191603.

160. Feifel M, Ohlmann J, Benick J, Rachow T, Janz S, Hermle M, et al. MOVPE Grown Gallium Phosphide–Silicon Heterojunction Solar Cells. IEEE Journal of Photovoltaics. 2017;7(2):502-7.

161. Tea E, Vidal J, Pedesseau L, Cornet C, Jancu JM, Even J, et al. Theoretical study of optical properties of anti phase domains in GaP. Journal of Applied Physics. 2014;115(6):063502.

162. Cornet C, Da Silva M, Levallois C, Durand O. GaP/Si-Based Photovoltaic Devices Grown by Molecular Beam Epitaxy. In: Henini M, editor. Molecular Beam Epitaxy. Elsevier; 2018. p. 637-48.

163. Contour JP, Massies J, Saletes A. X-ray photoelectron spectroscopy study of GaAs (001) and InP (001) cleaning procedures prior to molecular beam epitaxy. Japanese journal of applied physics. 1985;24(7A):L563.

164. Kher SS, Wells RL. A straightforward, new method for the synthesis of nanocrystalline GaAs and GaP. Chemistry of materials. 1994;6(11):2056-62.

165. Nishitani R, Iwasaki H, Mizokawa Y, Nakamura S. An XPS analysis of thermally grown oxide film on GaP. Japanese Journal of Applied Physics. 1978;17(2):321.

166. Garbassi F. XPS and AES study of antimony oxides. Surface and Interface Analysis. 1980;2(5):165-9.

167. Bhachu DS, Egdell RG, Sankar G, Carmalt CJ, Parkin IP. Electronic properties of antimony-doped anatase TiO_2 thin films prepared by aerosol assisted chemical vapour deposition. Journal of Materials Chemistry C. 2017;5(37):9694-701.

168. Kitamura N, Kikuchi T, Kakehi M, Wada T. Chemical Depth Profile of Thermal Oxide on GaSb Using XPS Method. Japanese Journal of Applied Physics. 1984;23(Part 1, No. 11):1534-5.

169. Yu W, Sullivan JL, Saied SO. XPS and LEISS studies of ion bombarded GaSb, InSb and CdSe surfaces. Surface Science. 1996;352-354:781-7.

170. Nguyen Thanh T, Robert C, Guo W, Létoublon A, Cornet C, Elias G, et al. Structural and optical analyses of GaP/Si and (GaAsPN/GaPN)/GaP/Si nanolayers for integrated photonics on silicon. Journal of Applied Physics. 2012;112(5):053521.

171. Qiu Y, Li M, Liu G, Zhang B, Wang Y, Zhao L. Investigation of crystallographic tilting in GaSb/GaAs heteroepitaxial structure by high-resolution X-ray diffraction. Journal of Crystal Growth. 2007;308(2):325-9.

172. Cherng YT, Jou MJ, Jen HR, Stringfellow GB. Raman scattering in $GaP_{1-x}Sb_x$. Journal of Applied Physics. 1988;63(11):5444-6.

173. Cherng YT, Jaw DH, Jou MJ, Stringfellow GB. Lattice vibration spectra of $GaP_{1-x}Sb_x$ and $InP_{1-x}Sb_x$. Journal of Applied Physics. 1989;65(8):3285-8.

174. Loualiche S, Le Corre A, Salaun S, Caulet J, Lambert B, Gauneau M, et al. GaPSb: A new ternary material for Schottky diode fabrication on InP. Applied Physics Letters. 1991;59(4):423-4.

175. Van de Walle CG, Neugebauer J. Universal alignment of hydrogen levels in semiconductors, insulators and solutions. Nature. 2003;423(6940):626-8.

176. Serpone N, and Ezio Pelizzetti. Photocatalysis: Fundamentals and Applications. Wiley. 1989:650

177. Robert C, Cornet C, Turban P, Nguyen Thanh T, Nestoklon MO, Even J, et al. Electronic, optical, and structural properties of (In,Ga)As/GaP quantum dots. Physical Review B. 2012;86(20).

178. Pinaud BA, Benck JD, Seitz LC, Forman AJ, Chen Z, Deutsch TG, et al. Technical and economic feasibility of centralized facilities for solar hydrogen production via photocatalysis and photoelectrochemistry. Energy & Environmental Science. 2013;6(7):1983-2002.

179. Kibria MG, Mi Z. Artificial photosynthesis using metal/nonmetal-nitride semiconductors: current status, prospects, and challenges. Journal of Materials Chemistry A. 2016;4(8):2801-20.

180. McCrory CC, Jung S, Peters JC, Jaramillo TF. Benchmarking heterogeneous electrocatalysts for the oxygen evolution reaction. Journal of the American Chemical Society. 2013;135(45):16977-87.

181. Stampfl C, Van de Walle CG. Energetics and electronic structure of stacking faults in AlN, GaN, and InN. Physical Review B. 1998;57(24):R15052-R5.

182. Alhassan AI, Farrell RM, Saifaddin B, Mughal A, Wu F, DenBaars SP, et al. High luminous efficacy green light-emitting diodes with AlGaN cap layer. Optics Express. 2016;24(16):17868-73.

183. Ebaid M, Kang J-H, Lim S-H, Cho Y-H, Ryu S-W. Towards highly efficient photoanodes: the role of carrier dynamics on the photoelectrochemical performance of InGaN/GaN multiple quantum well coaxial nanowires. RSC Advances. 2015;5(30):23303-10.

184. Tao T, Zhi T, Liu B, Li M, Zhuang Z, Dai J, et al. Significant improvements in InGaN/GaN nano-photoelectrodes for hydrogen generation by structure and polarization optimization. Scientific Reports. 2016;6:20218.

185. Fan S, Shih I, Mi Z. A Monolithically Integrated InGaN Nanowire/Si Tandem Photoanode Approaching the Ideal Bandgap Configuration of 1.75/1.13 eV. Advanced Energy Materails. 2017;7(2):1600952.

186. Gopalakrishnan M, Gopalakrishnan S, Bhalerao GM, Jeganathan K. Multiband InGaN nanowires with enhanced visible photon absorption for efficient photoelectrochemical water splitting. Journal of Power Sources. 2017;337:130-6.

187. AlOtaibi B, Fan S, Vanka S, Kibria MG, Mi Z. A Metal-Nitride Nanowire Dual-Photoelectrode Device for Unassisted Solar-to-Hydrogen Conversion under Parallel Illumination. Nano Letter. 2015;15(10):6821-8.

188. Alvi NuH, Soto Rodriguez PED, Aseev P, Gómez VJ, Alvi AuH, Hassan Wu, et al. InN/InGaN quantum dot photoelectrode: Efficient hydrogen generation by water splitting at zero voltage. Nano Energy. 2015;13:291-7.

189. Park JH, Mandal A, Kang S, Chatterjee U, Kim JS, Park BG, et al. Hydrogen Generation using non-polar coaxial InGaN/GaN Multiple Quantum Well Structure Formed on Hollow n-GaN Nanowires. Scientific Reports. 2016;6:31996.

190. Fan S, AlOtaibi B, Woo SY, Wang Y, Botton GA, Mi Z. High efficiency solar-to-hydrogen conversion on a monolithically integrated InGaN/GaN/Si adaptive tunnel junction photocathode. Nano Letter. 2015;15(4):2721-6.

191. Caccamo L, Hartmann J, Fabrega C, Estrade S, Lilienkamp G, Prades JD, et al. Band engineered epitaxial 3D GaN-InGaN core-shell rod arrays as an advanced photoanode for visible-light-driven water splitting. ACS Applied Materails Interfaces. 2014;6(4):2235-40.

192. Ganesh V, Alizadeh M, Shuhaimi A, Adreen A, Pandikumar A, Jayakumar M, et al. Correlation between indium content in monolithic InGaN/GaN multi quantum well structures on photoelectrochemical activity for water splitting. Journal of Alloys and Compounds. 2017;706:629-36.

193. Bae H, Park J-B, Fujii K, Lee H-J, Lee S-H, Ryu S-W, et al. The Effect of the number of InGaN/GaN pairs on the photoelectrochemical properties of InGaN/GaN multi quantum wells. Applied Surface Science. 2017;401:348-52.

194. Zhi T, Tao T, Liu B, Li M, Zhuang Z, Dai J, et al. Enhanced InGaN/GaN photoelectrodes for visible-light-driven hydrogen generation by surface roughening. physica status solidi (a). 2016;213(10):2704-8.

195. Alqahtani M, Sathasivam S, Alhassan A, Cui F, BenJaber S, Blackman C, et al. InGaN/GaN Multiple Quantum Well Photoanode Modified with Cobalt Oxide for Water Oxidation. ACS Applied Energy Materials. 2018;1(11):6417-24.

196. Fujii K, Nakamura S, Yokojima S, Goto T, Yao T, Sugiyama M, et al. Photoelectrochemical Properties of InxGa1–xN/GaN Multiquantum Well Structures in Depletion Layers. The Journal of Physical Chemistry C. 2011;115(50):25165-9.

197. Varadhan P, Fu HC, Priante D, Retamal JR, Zhao C, Ebaid M, et al. Surface Passivation of GaN Nanowires for Enhanced Photoelectrochemical Water-Splitting. Nano Letter. 2017;17(3):1520-8.

198. Zhao Y, Yan Q, Huang C-Y, Huang S-C, Shan Hsu P, Tanaka S, et al. Indium incorporation and emission properties of nonpolar and semipolar InGaN quantum wells. Applied Physics Letters. 2012;100(20):201108.

199. Li Y, Zhao S, Hu Q, Gao Z, Liu Y, Zhang J, et al. Highly efficient CoO_x/SBA-15 catalysts prepared by atomic layer deposition for the epoxidation reaction of styrene. Catalysis Science & Technology. 2017;7(10):2032-8.

200. Zhou X, Liu R, Sun K, Papadantonakis KM, Brunschwig BS, Lewis NS. 570 mV photovoltage, stabilized n-Si/CoO_x heterojunction photoanodes fabricated using atomic layer deposition. Energy & Environmental Science. 2016;9(3):892-7.

201. Fester J, Garcia-Melchor M, Walton AS, Bajdich M, Li Z, Lammich L, et al. Edge reactivity and water-assisted dissociation on cobalt oxide nanoislands. Nature Communication. 2017;8:14169.

202. Chen Z, Duan Z, Wang Z, Liu X, Gu L, Zhang F, et al. Amorphous Cobalt Oxide Nanoparticles as Active Water-Oxidation Catalysts. ChemCatChem. 2017;9(19):3641-5.

203. Yang J, Walczak K, Anzenberg E, Toma FM, Yuan G, Beeman J, et al. Efficient and sustained photoelectrochemical water oxidation by cobalt oxide/silicon photoanodes with nanotextured interfaces. Journal of the American Chemical Society. 2014;136(17):6191-4.

204. Kwapien K, Piccinin S, Fabris S. Energetics of Water Oxidation Catalyzed by Cobalt Oxide Nanoparticles: Assessing the Accuracy of DFT and DFT+U Approaches against Coupled Cluster Methods. The Journal of Physical Chemistry Letters. 2013;4(24):4223-30.

205. Gujral SS, Simonov AN, Higashi M, Fang X-Y, Abe R, Spiccia L. Highly Dispersed Cobalt Oxide on TaON as Efficient Photoanodes for Long-Term Solar Water Splitting. ACS Catalysis. 2016;6(5):3404-17.

206. García-Mota M, Bajdich M, Viswanathan V, Vojvodic A, Bell AT, Nørskov JK. Importance of Correlation in Determining Electrocatalytic Oxygen Evolution Activity on Cobalt Oxides. The Journal of Physical Chemistry C. 2012;116(39):21077-82.

207. Lichterman MF, Shaner MR, Handler SG, Brunschwig BS, Gray HB, Lewis NS, et al. Enhanced Stability and Activity for Water Oxidation in Alkaline Media with Bismuth Vanadate Photoelectrodes Modified with a Cobalt Oxide Catalytic Layer Produced by Atomic Layer Deposition. The Journal of Physical Chemistry Letters. 2013;4(23):4188-91.

208. Zhang M, de Respinis M, Frei H. Time-resolved observations of water oxidation intermediates on a cobalt oxide nanoparticle catalyst. Nature Chemistry. 2014;6(4):362-7.

209. Biesinger MC, Payne BP, Grosvenor AP, Lau LWM, Gerson AR, Smart RSC. Resolving surface chemical states in XPS analysis of first row transition metals, oxides and hydroxides: Cr, Mn, Fe, Co and Ni. Applied Surface Science. 2011;257(7):2717-30.

210. Bajdich M, Garcia-Mota M, Vojvodic A, Norskov JK, Bell AT. Theoretical investigation of the activity of cobalt oxides for the electrochemical oxidation of water. Journal of the American Chemical Society. 2013;135(36):13521-30.

211. Kim J, Iivonen T, Hämäläinen J, Kemell M, Meinander K, Mizohata K, et al. Low-Temperature Atomic Layer Deposition of Cobalt Oxide as an Effective Catalyst for Photoelectrochemical Water-Splitting Devices. Chemistry of Materials. 2017;29(14):5796-805.

212. Seabold JA, Choi K-S. Effect of a Cobalt-Based Oxygen Evolution Catalyst on the Stability and the Selectivity of Photo-Oxidation Reactions of a WO_3 Photoanode. Chemistry of Materials. 2011;23(5):1105-12.

213. Zhou X, Chesin J, Crawford S, Gradecak S. Using seed particle composition to control structural and optical properties of GaN nanowires. Nanotechnology. 2012;23(28):285603.

214. Walle CSaCGVd. Energetics and electronic structure of stacking faults in AlN, GaN, and InN. physical review B. 1998;57.

215. Yeh C-Y, Lu ZW, Froyen S, Zunger A. Zinc-blende–wurtzite polytypism in semiconductors. Physical Review B. 1992;46(16):10086-97.

216. Mishra P, Janjua B, Ng TK, Anjum DH, Elafandy RT, Prabaswara A, et al. On the optical and microstrain analysis of graded InGaN/GaN MQWs based on plasma assisted molecular beam epitaxy. Optical Materials Express. 2016;6(6):2052-62.

217. Bertóti I. Characterization of nitride coatings by XPS. Surface and Coatings Technology. 2002;151-152:194-203.

218. Guo QX, Nishio M, Ogawa H, Wakahara A, Yoshida A. Electronic structure of indium nitride studied by photoelectron spectroscopy. Physical Review B. 1998;58(23):15304-6.